Master Thesis

Seismic analysis of Mars using gravitational potential stresses - InSight

Lisa De Backer
Student number: 4233530
Supervisor: Bart Root

Delft University of Technology

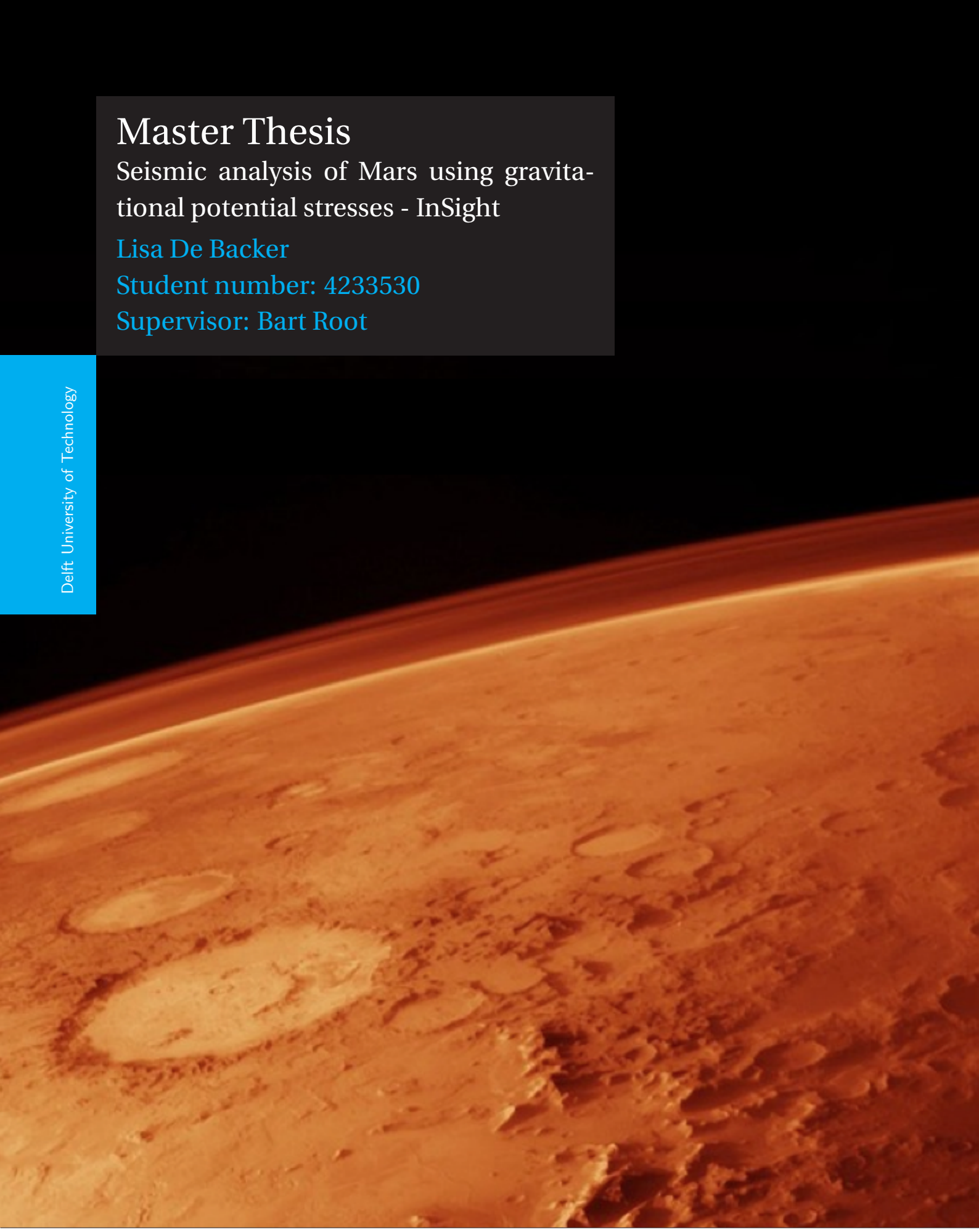

TU Delft Delft University of Technology

Challenge the future

PREFACE

"I would like to die on Mars, just not on impact"

— Elon Musk

This report contains my master thesis research which is the final part of my studies. It is a part of the Space Flight master program of the faculty Aerospace Engineering at Delft University of Technology. The topic is the determination of the stress field on Mars in order to identify likely sources of marsquakes which will be measured by the upcoming InSight mission from NASA. This subject was chosen as I am very enthusiastic about space exploration and as the rumbling of a planet has always fascinated me. The master thesis research started in April 2018 and ends in December 2018. This amount to seven months of full time work.

I would like to thank Bart Root, for having weekly meetings with me, always giving useful suggestions and being happy to answer all my questions. I consider myself very lucky to have worked together with Bart. He gave me the opportunity to learn a lot from him in a friendly atmosphere and I value this a lot. Apart from Bart, I would like to thank Wouter van der Wal and Pavel Ditmar for being in my assessment committee. I would also like to thank my family and friends for supporting me with my final thesis project.

Front page picture from NASA

LIST OF FIGURES

LIST OF TABLES

NOMENCLATURE

Greek Symbols

Symbol	Description	Units
γ	Correlation	–
λ	Fluid pressure factor	–
λ	Longitude	rad
λ	Wavelength	m
μ	Gravitational parameter	km^3/s^2
Ω	Position on a sphere	(rad, rad)
ρ_{avg}	Average density	kg/m^3
σ	Scaling factor	–
σ	Stress	Pa
σ_n	Normal stress	Pa
σ_1	Minimum principal stress	Pa
σ_3	Maximum principal stress	Pa
σ_{diff}	Differential stress	Pa
σ_H	Horizontal stress	Pa
σ_V	Vertical stress	Pa
σ_{xx}	Horizontal stress	Pa
σ_{zz}	Vertical stress	Pa
τ	Shear stress	Pa
θ	Co-latitude	rad

Roman Symbols

Symbol	Description	Units
$\bar{P}_{nm}$	Normalized associated Legendre functions	
δg_T	Terrain correction	m/s^2
ϕ	Latitude	$^\circ$
ρ_c	Crustal density	kg/m^3
ρ_m	Mantle density	kg/m^3
c_t	Crustal thickness	m
C_{nm}	Spherical harmonics coefficients	–

D_c	Compensation depth	km
d_c	Crustal depth	m
d_{m-e}	Distance Mars - Earth	km
d_{m-s}	Semi-major axis mars, distance Mars - Sun	km
DV	Degree variance	–
G	Gravitational constant	$m^3/(kg\ s^2)$
g	Gravitation acceleration	m/s^2
g_0	Average gravitational acceleration	m/s^2
g_B	Bouguer gravity	m/s^2
g_F	Free-air gravity	m/s^2
g_{obs}	Observed gravity	m/s^2
h	Altitude	m
l	Distance between two points	m
M	Mass	kg
m	Spherical harmonic order	–
n	Spherical harmonic degree	–
P_{nm}	Normalized Legendre functions	–
R	Average radius	km
r	Variable part crustal thickness, Airy model	m
R_{eq}	Equatorial radius	km
R_{polar}	Polar radius	km
S_{ff}	Power spectrum spherical harmonics	–
S_{fg}	Cross-power spectrum spherical harmonics	–
T_{bb}	Black body temperature	K
t_{sol}	Time in a sol	h
U	Gravitational potential energy	J
V	Gravitational potential	J/kg
Z	Admittance	–
z_{bl}	Baseline lithospheric depth	m
z_i	Intersection depth of the GPSt and yield stress	km

ABBREVIATIONS

BDT ..... Brittle-ductile transition

CMB ..... Core-mantle boundary

ESA ..... European Space Agency

FR ..... Failure ratio

GPE ..... Gravitational potential energy

GPSt ..... Gravitational potential stresses

GSHA ..... Global spherical harmonics analysis

GSHS ..... Global spherical harmonics synthesis

HiRISE ..... High Resolution Imaging Science Experiment

HP3 ..... Heat Flow and Physical Properties Probe

InSight ..... Interior Exploration using Seismic Investigations, Geodesy and Heat Transport

MGS ..... Mars Global Surveyor

MOLA ..... Mars Orbiter Laser Altimeter

MRO ..... Mars Reconnaissance Orbiter

NASA ..... National Aeronautics and Space Administration

RISE ..... Rotation and Interior Structure Experiment

RMS ..... Root mean square

SEIS ..... Seismic Experiment for Interior Structure

SH ..... Spherical harmonics

SNC ..... Shergottites, Nakhlites and Chassignites

YSE ..... Yield stress evenlope

SUMMARY

November 26th 2018, the InSight mission from NASA will land on Mars. InSight's main mission objective is to learn more about the interior of Mars, link this to other terrestrial planets and to determine the meteorite impact rate and seismicity level of Mars. This will be investigated by use of a seismometer, SEIS, an internal heat probe, HP3, and an exact location tracker, RISE. In order to process the incoming data of SEIS as fast and efficient as possible, a-priori models of seismicity on Mars are advantageous. This thesis work comprises the creation of such models by using gravitational potential theory. The focus is on deriving several configurations for the interior density structure of Mars (crust and upper mantle) and creating gravitational potential stress maps using the approximated density models. The stress maps are linked to the yield stress and hence allow to identify the most likely sources of seismicity on Mars. Important findings are the interior stress field of Mars and a method to quickly make a first analysis of incoming SEIS data. This research is renewing in three ways: (1) more possibilities of density profiles of the crust and upper mantle are analyzed, (2) the gravitational potential theory has never been applied on Mars before and (3) a seismic analysis by use of yield stress envelopes has never been performed on Mars. This project will contribute to the determination of the interior structure of Mars and to knowledge on the formation of terrestrial planets in the solar system.

Several methods are used to create interior density models of Mars. First of all, isostatic assumptions are used which result in several Airy and Pratt-like models. Next, the Bouguer gravity is used to create a third type of interior density models. The fourth and fifth type of models are the models created by Wieczorek (2015) and Goossens et al. (2017). Wieczorek (2015) uses the Bouguer gravity to create five different models with a varying crustal density. Goossens et al. (2017) uses the admittance between gravity and topography data to estimate the average crustal density and crustal thickness. All models are fitted to the gravitational potential using the software from Root et al. (2016) which calculates the gravitational potential from density layers inside a planet using spherical harmonics. The resulting density models are used to calculate gravitational potential stresses. Conclusions about likely epicenters can be made by comparing the yield stress envelope of Mars with the calculated gravitational potential stresses for each model. The yield stress envelope can be calculated using Byerlee's law, which states that for large stresses the yield stress does not depend on the type of material but on the amount of pressure in the lithosphere. Finally, the failure ratio can be determined by comparing the gravitational potential stresses with the yield stress envelopes, calculated using Byerlee's law. The failure ratio is the ratio between the depth at which the yield stress is reached and the brittle-ductile transition depth. The brittle-ductile transition depth is the depth up to which marsquakes are expected to happen, below this depth only ductile failure will occur which does not lead to seismic activity. The higher the failure ratio, the more likely failure is to occur at that specific spot. The sensitivity of several parameters on the failure ratio is tested during this research in order to be able to make efficient conclusions about incoming InSight data.

The outcome of the thesis shows that the higher the level of isostatic compensation on the planet, the lower the gravitational potential stresses and failure ratios are. Varying the average crustal and mantle density and the average crustal thickness or compensation depth leads to different interior density models. Before starting the project, it was expected that varying the average crustal density would have a large effect on the failure ratios, however, this proved to be untrue. The crustal density is canceled out when combining the equations for gravitational potential stresses and the yield stress envelope. An average crustal thickness which is close to the brittle-ductile transition depth leads to lower stresses due to an increased amount of isostatic compensation. The Airy and Pratt models lead to lower stresses compared to the Bouguer, Wieczorek (2015) and Goossens et al. (2017) models they both assume isostatic compensation whereas the latter models do not. A more shallow brittle-ductile transition depth leads to higher stresses as the amount of compensation up to that level is still low compared to at a deeper brittle-ductile transition depth. Also, the yield stress at shallow depths is lower than at greater depths. These two factors lead to higher failure ratios when the brittle-ductile transition depth is more shallow. As last, the yield stress is significantly lower when the lithosphere is in a wet state in comparison to a dry state. Therefore, higher failure ratios are found when the lithosphere is wet or in a hydrostatic state. The actual amount of liquid in the Martian lithosphere is still unclear up to this moment.

Several interesting locations are Utopia Planitia, Isidis Planitia and Elysium Mons. If seismicity at these locations is high, the interior density of Mars is expected to be non compensated in these regions and more related to the Bouguer gravity. If more seismicity is coming from the south compared to the north, the planet is presumed to have Pratt-like isostasy, meaning that the crustal density in the north is higher than the crustal density in the south. In the north of Utopia Planitia, northeast of Alba Patera, around Arcadia Planitia, around the Tharsis volcanoes and below Elysium Mons, active faults of Mars neatly align with the calculated failure ratios, indicating that seismic activity is likely at these locations. A higher than expected seismic moment per year on Mars points to one or more of the several factors: (1) a shallow brittle-ductile transition depth (+/- 30-40 km), (2) a wetter lithosphere, (3) a small crustal thickness range and (4) a low level of isostatic compensation.

This proved to be a renewing and interesting research since gravitational potential stresses have never been combined with yield stress envelopes before, certainly not on Mars. This method proved to work and it is therefore suggested to also use this method on other planets. This research will help the analysis of incoming InSight data which will improve the overall knowledge about the interior and origin of Mars. Some recommendations for future research are to focus more on lateral density variations, the brittle-ductile transition depth and whether the lithosphere is in a wet or dry state or something in between. Likewise, the combination of flexural stresses and gravitational potential stresses is another interesting upcoming research topic. Also, when even a slight amount of seismic data on Mars comes in, it will be easier to determine which models are actually most realistic. Therefore it is recommended to continue similar analyses once more data becomes available. At last, a relation between the failure ratio and the magnitude of seismic events would be beneficial for quake analyses on Mars, on the Earth or other terrestrial planets.

CONTENTS

1. INTRODUCTION

The interior of Mars is essential to human knowledge regarding the formation of terrestrial planets. The best method to determine the inside of a planet is to have a seismometer on its surface. For a long time, people have been trying to develop a lander to go to Mars with a seismometer on board. The Viking landers in 1975 both had a seismometer placed on top of their structure, however due to a lack of direct ground contact there was too much noise to derive significant information of seismicity on Mars (Lorenz et al., 2017). Now, in November 2018, NASA's InSight mission (Interior Exploration using Seismic Investigations, Geodesy and Heat Transport) will land on the surface of Mars with on board three instruments. These instruments are SEIS (the Seismic Experiment for Interior Structure), HP3 (The Heat Flow and Physical Properties Probe) and RISE (Rotation and Interior Structure Experiment) and will be employed at the InSight landing site in Elysium Planitia. The main common goal of the instruments is to learn more about the crust, mantle and core of Mars. Before the actual landing of InSight, preliminary research regarding marsquakes needs to be performed. In this chapter, a literature recap of past research towards the interior and seismicity of Mars is given. The literature review concludes with a clear set of research questions.

1.1. MARS; THE RED PLANET

Currently, Mars is the most popular planet regarding space exploration. It is known as the small, red planet close to the Earth. Mars is the fourth terrestrial planet in our solar system. Mars has a gravitational acceleration on its surface of 3.711 kg/m^2 and an average radius of 3389.5 km (about half of the Earth's radius).[1] A list of more general properties of the planet can be found in Table 1.1. Mars has two moons: Phobos and Deimos with a radius of 13.0 and 7.8 km respectively. Both moons are not heavy enough to have achieved a circular form.[1] Also, both moons are tidally locked to Mars. A topographic map of Mars is shown in Figure 1.1. Its two most prominent features are the Tharsis rise and the hemispheric dichotomy. Tharsis is a large volcanic plateau with three huge aligned volcanoes on it; Arsia Mons, Pavonis Mons, and Ascraeus Mons reaching an altitude of 18, 14 and 18 km respectively. Northwest from the Tharsis rise is the largest volcano of the solar system: Olympus Mons, which reaches a stunning altitude of 21 km (Melosh, 2011). The crustal dichotomy of Mars is the contrast between the northern lowland and the southern highlands. The average altitude difference between the north and south is about six kilometers. The south is heavily cratered while the north has a relatively smooth surface. The origins of both the Tharsis rise and the crustal dichotomy are still being debated. There are several suggestions that the creation of Tharsis and the hemispheric dichotomy are related. One of the suggestions is that Tharsis was underlain by a convective cell, and that this cell had first created the dichotomy and afterwards Tharsis (H. Barosio et al., 2001). Another suggestion is that Tharsis originated out of the build-up of lava flows which are supported by the lithosphere (Wieczorek, 2007). Proposed causes that lead to the formation of the crustal dichomoty are (1) a large meteorite impact (Marinova et al., 2008; Watters and McGovern, 2006), (2) thinning of the lowland crust by mantle convection or plate tectonics (Watters and McGovern, 2006), (3) a high heat flow in the north during the Martian history (Zuber et al., 2000) and (4) an ancient ocean which covered the north of the planet (Perron et al., 2007).

It is highly suggested that Mars has no plate tectonics and has a liquid core (Denton, 2017; Zharkov and Gudkova, 1993, 1997). Both will only be confirmed once InSight lands on the surface. The liquid core of Mars has been proven by Zharkov and Gudkova (1993, 1997). Most other authors also assume this is the case. However, it is important to keep into mind that the actual confirmation will only arise once seismic measurements of Mars are available.

The suggestion that Mars has no plate tectonics but one large plate can be derived by the conditions needed for plate tectonics: (1) the environment needs to be cold enough such that a magma ocean cannot exist, (2) the planet needs to be warm enough such that there is convection in the upper layers of the planet, (3) the lithosphere needs to be in a certain state for the plates to be able to subduct: thin, cool, strong and dense enough and (4) it is suggested that liquid water is needed on the surface, as on Earth most plate boundaries

[1] URL `https://nssdc.gsfc.nasa.gov/planetary/factsheet/marsfact.html` [31-03-2018]

Property	Symbol	Value	Unit
Equatorial radius	R_{eq}	3396.2	km
Polar radius	R_{polar}	3376.2	km
Average radius	R	3389.5	km
Mass	M	$6.4171 \cdot 10^{23}$	kg
Average density	ρ_{avg}	3933	kg/m^3
Gravitational constant	G	$6.67259 \cdot 10^{-11}$	$m^3/(kgs^2)$
Gravitational parameter	$GM = \mu$	$4.2828 \cdot 10^4$	km^3/s^2
Gravity	g	3.711	m/s^2
Black body temperature	T_{bb}	209.8	K
Astronomical unit	AU	149597870.700	km
Semi-major axis	d_{m-s}	1.52366231	AU
Distance Mars - Earth	d_{m-e}	55.7-401.3 $\cdot 10^6$	km
One day (sol)	t_{sol}	24.6597	h

Table 1.1: General properties Mars. All values are from the NASA Mars factsheet.[1]

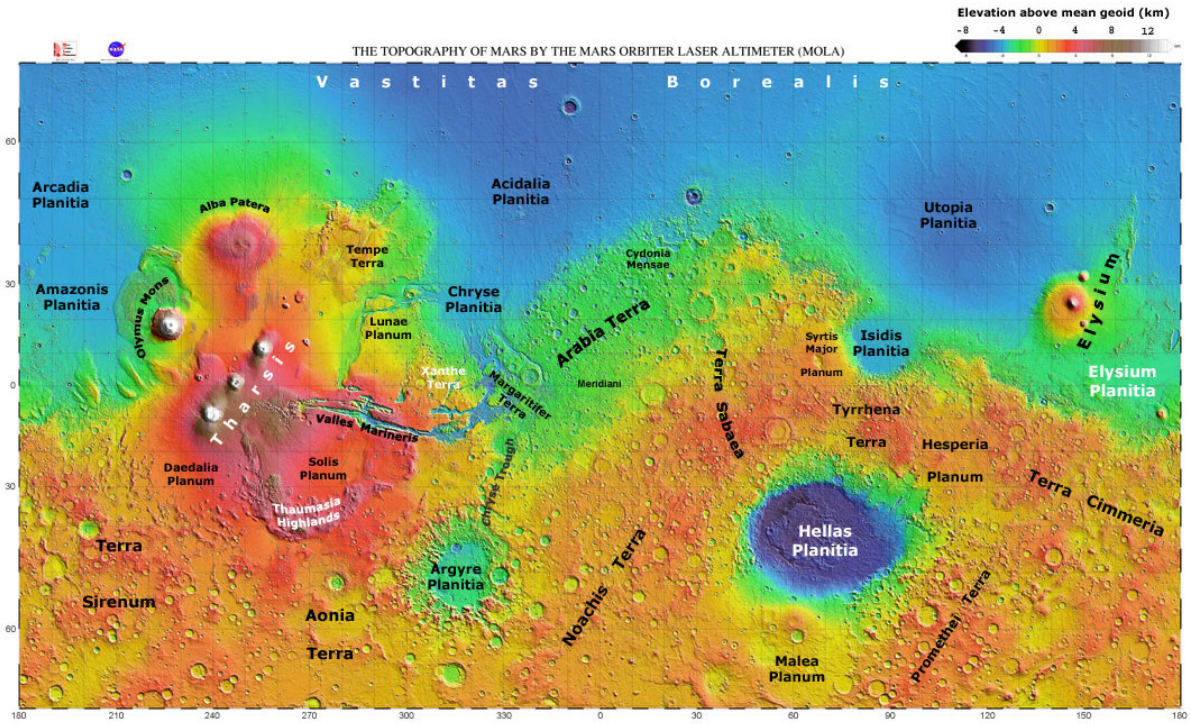

Figure 1.1: Topographic map of Mars created by the Mars Orbiter Laser Altimeter (MOLA), an instrument on the Mars Global Surveyor (MGS). Location names on Mars are shown on the map.[2]

are at an ocean/continent boundary where the weight of the water decreases the crust size of the oceanic plates which makes subduction possible (Denton, 2017). As Mars is too cold and there is no water on the surface, the most plausible theory is that there is no plate tectonics on the planet (Denton, 2017; McLennan, 2001). Therefore, in the remainder of this project it is assumed that there is no plate tectonics on Mars while keeping into account that this will only be confirmed once InSight lands on the Martian surface.

While on Earth the main source of seismic activity is the motion of the plate boundaries, seismic motion on Mars might have other origins. There are currently four presumed sources of marsquakes: (1) meteorite impacts: when looking at the surface of Mars numerous impact craters can be seen, (2) Phobos moon tidal effects: Phobos is Mars its biggest moon, its tidal interaction with Mars can cause marsquakes, (3) Faulting:

[1] URL `https://nssdc.gsfc.nasa.gov/planetary/factsheet/marsfact.html` [31-03-2018]
[2] URL `http://web.csulb.edu/~rodrigue/mars/indexS16.html` [08-11-2018]

this is what is known on Earth as intraplate earthquakes, the cooling and shrinking of the interior of Mars or magmamotions underground provide the energy for these kinds of quakes and (4) atmospheric excitation: this implies big storms which can shake up Mars (Denton, 2017). In this project all attention is put into marsquakes due to the cooling down and shrinking of the planet.

1.2. NASA'S INSIGHT MISSION

The Interior Exploration using Seismic Investigations, Geodesy and Heat Transport mission, in short, InSight, is the mission from NASA to which this research is linked to. Its launch took place the 5th of May using the Atlas V and its arrival at Mars will be November 26th 2018 (which might already have happened once the reader finds this report). Its mission is to study the inside of Mars: its core, mantle and crust. Most information in this section is deducted from the NASA website on the InSight mission.[1]

As mentioned shortly before, the main goal of the InSight mission is to study the interior of Mars. To be more explicit, the InSight team has set up two science goals for the missions:

1. *"Understand the formation and evolution of terrestrial planets through investigation of the interior structure and processes of Mars."*
2. *"Determine the present level of tectonic activity and meteorite impact rate on Mars."*

These goals will be reached with the help of three instruments: SEIS (Seismic Experiment for Interior Structure), HP3 (Heat Flow and Physical Properties Probe) and RISE (Rotation and Interior Structure Experiment). In Figure 1.2 instruments and functionalities are indicated on an image of InSight. SEIS is a seismometer and will measure seismic activity on the planet. HP3 is a heat probe that will burrow down up to 5 meters in the surface of Mars. Its main research question is how much heat is still coming from Mars its interior and leaving the planet. RISE will track the exact location of InSight up to a few centimeters. By doing so, more can be learned about Mars its movements in space: Mars its wobble (Earth-like Chandler wobble), precession and nutation.

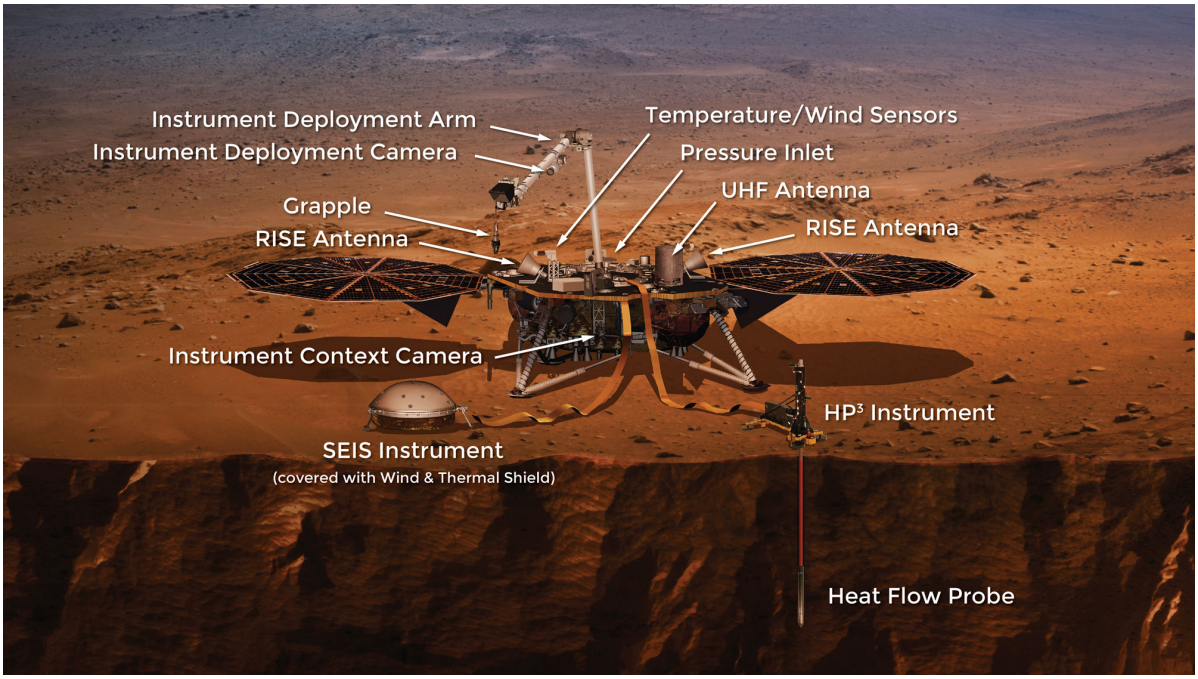

Figure 1.2: The InSight lander and its instruments. The three main instruments are SEIS (seismometer), HP3 (heat probe) and RISE (two radio tracking antennas). Other components of the lander are two cameras, a deployment arm, a UHF antenna, environmental sensors and solar arrays.[2]

From the launch onwards, it takes InSight six months to arrive on Mars on November 26th in 2018. In Figure 1.3, the landing site, located in Elysium Planitia, can be seen on a photographic map of Mars. Previous

[1] URL `https://mars.nasa.gov/insight/` [02-01-2018]

landing sites of Martian missions from NASA can also be seen. The landing site in Elysium Planitia is located close to the Elysium Mons volcano, which has an altitude of about 16 km (Melosh, 2011). The landing site is chosen to be Elysium Planitia for several reasons. First of all, important to keep into account while choosing a landing site is that it has to be low enough for the lander to slow down during approach. Secondly, the lander needs to be located close to the equator for its solar arrays to be able to catch enough sunlight during all seasons. Also important is that the slope of the landing site is not too high, if so the lander could tip over after touch down or the slope could prevent the solar arrays from receiving enough light. HiRISE images were very useful in selecting an appropriate landing site. HiRISE (High Resolution Imaging Science Experiment) is an instrument on the Mars Reconnaissance Orbiter (MRO) which provides images with great detail of Mars its surface. Once InSight has landed and all its instruments are deployed (which takes about ten weeks), the prime mission will take on for about two Earth years, which is equal to one Martian year, 708 sols or 728 days. So far, several landers and orbiters of Mars have functioned way past their initial mission duration since no functional problems were encountered. This is also a possibility for InSight.

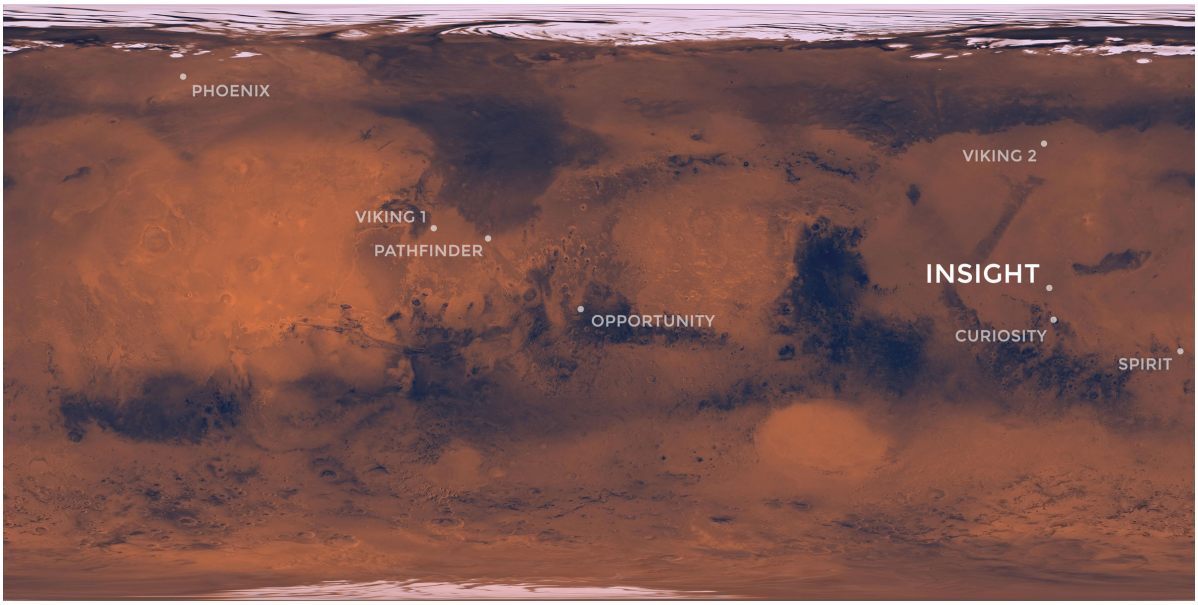

Figure 1.3: Photographic map of Mars, indicating the InSight landing site in Elysium Planitia. The landing sites of past NASA landers and rovers are also shown on the map.[3]

Planned outcomes of InSight consist among others of constraints on the interior of Mars, the core-mantle boundary and crustal thickness determination. The material transitions in the Martian mantle can also be analyzed. A seismic catalogue of Mars will be created, indicating more about the current seismicity and meteorite impact rate on Mars. The tidal Love numbers, h_2 and k_2, will be determined by analyzing seismic waves due to interaction with Phobos. Whether or not Mars has plate tectonics and a liquid core will be confirmed by InSight. All these measurements will also indicate more information about the origin of the weak Martian magnetic field. Conclusions about habitability on Mars and the possibility of a human Martian habitat will be made.

1.3. State of the art seismic predictions

One method to study seismicity on a planet is to look at the yield stress envelope (YSE). When creating the YSE, two laws are used: Byerlee's law for the brittle regime and the flow law for the ductile regime (Burov, 2011). The brittle yield stress increases with depth, while the ductile yield stress decreases with depth. At their intersection, called the brittle-ductile transition depth or BDT depth, the highest yield stress of the lithosphere can be found. Marsquakes will only occur due to brittle failure, as this leads to a sudden short-time motion. Ductile failure leads to slow moving motion over a long timescale which does not create a quake.

[2] URL `https://mars.nasa.gov/insight/mission/instruments/` [02-04-2018]
[3] URL `https://mars.nasa.gov/insight/mission/timeline/prelaunch/landing-site-selection/` [02-04-2018]

Therefore, the BDT depth is an important parameter as it points towards the maximum depth at which a marsquake can be found. The BDT depth is also called the seismogenic depth.

So far, two studies have analyzed what the BDT depth could be. Plesa et al. (2018) found an average seismogenic depth of 50 km when using a 573 Kelvin isotherm and a depth of 180 km when using a 1073 Kelvin isotherm. They use the depth at which these temperature are reached as the depth up to which seismicity is expected. Above 753 K, quartz shows plastic behaviour and 1073 K is the maximum temperature where intraplate seismic activity on an oceanic plate occurs on Earth. They assume 1073 K to be the upper limit on Mars as well. The BDT depth estimations they make are significantly deeper compared to the Earth, where most quakes (except at subduction zones and oceanic plates) are above 40 km depth (Burov, 2011). Azuma and Katayama (2017) analyze several compressional YSEs for Mars while performing research towards the rheological structure of the planet. They look at two different locations: (1) at the North Pole (low topography and temperature) and (2) at Solis Planum (high topography and temperature, below Valles Marineris, see Figure 1.1). They consider a dry and hydrostatic state of the lithosphere. In the dry state, there is no liquid present in the lithosphere. In the hydrostatic state, the liquid pore pressure is equal to the pressure of the lithosphere. This means that there is no acceleration acting on the fluids. For both locations and both states, they create the YSE for Mars in the present and 1, 2, 3 and 4 Ga ago (1 Ga = 10^9 years). Their results on the BDT depth in compression are as follows:

- North Pole hydrostatic: BDT depth at 63 km
- North Pole dry: BDT depth > 75 km
- Solis Planum hydrostatic: BDT depth at 37 km
- Solis Planum dry: BDT depth > 75 km

Except for Solis Planum in a wet regime, the BDT depth is significantly deeper compared to the Earth. For tensional stresses the BTD is expected to be deeper, but with a lower governing maximum strength (Burov, 2011). When knowing the BDT depth, all what is left is to calculate Byerlee's law. Byerlee's law states that for large stresses (of the magnitude found in the crust of a planet), failure does not depend on the type of rock but on the pressure applied (Byerlee, 1978). He provides a set of two equations for the brittle strength which can be applied to Mars and which can be used in this research.

In order to derive conclusions from the yield stress envelopes, the actual stress in the lithosphere of Mars has to be calculated. A method which has been used before on Earth in intraplate zones, but never on Mars, is the gravitational potential theory (Pascal, 2006; Raulin, 2007). Gravitational potential stresses (GPSt) can be calculated from the density profile of Mars. The gravitational potential theory provides a clear method to calculate lateral stresses due to mass imbalances in the lithosphere. As Mars is presumed to have no plate tectonics, gravitational potential theory can be used on the whole planet. Compared to the theory of flexural stresses, the calculation of GPSt results in a more local stress field, which is what is desired in order to make seismic predictions. The lithosphere is assumed to be an elastic plate upon which loads are applied when calculating flexural stresses. The theory of flexural stresses thus provides another valid method to calculate subsurface stresses, therefore the flexural stresses calculated by Tenzer et al. (2015) are used for comparison purposes in this research. Tenzer et al. (2015) use a combination of the Navier-Stokes problem and the Vening Meinesz-Moritz inverse problem of isostasy while incorporating the thin plate lithospheric flexure model.

Before being able to calculate the GPSt, an interior density model of the planet is needed. The most important variable in knowing the density profile of the crust and upper mantle of a planet is the crustal thickness. The largest density contrast of the lithosphere can be found at the boundary between the crust and mantle, which is also called Moho, derived from Mohorovičić discontinuity. The crustal thickness of Mars has been calculated before by, among others, Wieczorek (2015) and Goossens et al. (2017). Both have diverse results: Wieczorek (2015) creates five models, each with a different crustal density between 2700 kg/m^3 and 3200 kg/m^3, whereas Goossens et al. (2017) calculates an average crustal density of 2582 kg/m^3. Wieczorek (2015) uses the Bouguer gravity anomaly to model the crustal thickness while taking into account the amplification of short-wavelength noise from the measured gravitational field. Using this method, an average crustal thickness and density needs to be assumed for each model. Goossens et al. (2017) use the admittance between the topography and gravity data, from which the average crustal density of Mars is derived. They find it to be a

lot lower than what has previously been suggested; the most often used value in literature is a crustal density of 2900 kg/m^3 (Neumann et al., 2004; Wieczorek, 2007; Zuber et al., 2000). Goossens et al. (2017) also state that large density variations are expected in the Martian crust. Apart from the models from Wieczorek (2015) and Goossens et al. (2017), isostatic assumptions and the Bouguer gravity can be used to create end-member interior density models (Watts, 2001). These models can be used to test the sensitivity of certain parameters. The last step in the interior density model creation is to calculate the gravitational field from an interior density model of a planet in order to see how well all models fit with reality. Root et al. (2016) provide software which calculates the gravitational forces from density layers inside a planet using the spherical harmonics representation. This software can be used to see which models are closest to reality. So far, there is still no consensus about what the interior structure of Mars is. The correct answers will only become clear after InSight has landed on Mars and the SEIS outcomes have extensively been analyzed.

Several results found so far on seismicity on Mars are from Knapmeyer et al. (2006) and Plesa et al. (2018). According to Knapmeyer et al. (2006) the major source of seismicity on Mars is the contraction of the entire planet. A fault catalogue of Mars is used to simulate a spacial distribution of seismicity. Three relations are used for this analysis: (1) the seismic moment budget, (2) the relation between seismic moment and frequency and (3) a rupture lengths versus released moment relation. Creating five different models, the total seismic moment release per year is found to be between $3.42 \cdot 10^{16}$ Nm and $4.78 \cdot 10^{18}$ Nm. The amount of faults which are still active today is a varying parameter in their research. First, the age of the fault is determined by looking at the age of the by the fault disturbed surface, this is assumed to be the age of the last activity of the respective fault. Two end members are analysed: one where all faults are assumed to be active and one where only faults younger than 500 million years are active. Their end member case used as upper limit (all faults active) identified 576 quakes per year with a magnitude greater than 4. They found that the largest amount of seismic events is expected to be in the Tharsis region. South of Hellas Basin and north of Utopia Planitia are also identified as high seismicity locations. It is concluded that with current knowledge the creation of a unique model on Martian seismicity is not possible, as a significant amount of assumptions on input parameters was used. This would make it interesting for future research to use varying values for these unknown parameters in order to see their effect on seismic predictions.

Plesa et al. (2018) use thermal evolution models of Mars based on convective stresses and stresses due to cooling and the contraction of Mars to make seismic budget estimations. When using only stresses due to the cooling and contraction of Mars, the conclusion is that the highest seismic budget values are found in areas where the crustal thickness is small: ie. in the north and in impact basins. Contrary, when only using convective stresses, high seismicity zones are found in regions with a thick crust. Taking both into account, a homogeneous distributions can be found while showing relative highs. They do not find high seismic activity in the Tharsis region, they say that this is because seismic activity there would mainly be due to flexural stresses which are not taken into account in this research. They use several models: the main variable parameters are the amount of active faults on Mars and the temperature of the isotherm. Active faults are assumed to be (1) faults which are no older than 600 million years, (2) faults which are no older than 3700 million years and (3) all faults. The fault catalogue from Knapmeyer et al. (2006) is used. The depth at which the isotherm is reached is used as the seismogenic depth. Two isotherms are used, (1) a low isotherm of 573 K which results in a lower seismogenic depth (average around 50 km depth) and (2) a high isotherm of 1073 K which results in a higher seismogenic depth (average around 180 km depth). When all faults are assumed as active, mostly homogeneous distributions of seismicity can be found. When only the youngest faults are active and the low isotherm is used, high seismicity zones are found around Alba Patera and between Isidis Planatia and Hellas Basin. When a high isotherm is used, the predictions are mainly dependable on the convective stresses, indicating high seismicity zones at topographic lows.

1.4. RESEARCH QUESTION

It is desired for the entire InSight mission that when the data of its instruments starts coming in, this data can be processed in the most efficient way. This can be done by performing a-priori research on the science goals of InSight. Whenever data comes in, the models which already exist can immediately be used and compared with the measured data. Needles to say, there will be lots of unexpected scenarios related to the InSight mission and it is impossible to completely anticipate all the incoming data, nevertheless creating a-priori models is the best possible way to prepare. Creating a model related to incoming data from SEIS is the main

purpose of the upcoming master thesis research. The goal is to model gravitational potential stresses and relate these to the yield stress. Doing so, the most likely sources of seismic vibrations to be measured by SEIS can be identified. Novelty compared to previous research is present in three ways: (1) more possibilities on density profiles of the crust and upper mantle of Mars are analyzed (2) the gravitational potential theory has never been applied on Mars before and (3) a seismic analysis by use of yield stress envelopes has never been performed on Mars. The research question is formulated as follows:

What are the most likely seismic epicenters of marsquakes derived from gravitational potential theory to be measured by the InSight mission?

Subquestions to solve this research question are given below:

- What is the density profile of the crust and upper mantle of Mars?
  - What is the crustal thickness?
- What is the gravitational potential stress field of Mars?
  - What is the gravitational potential energy field of Mars?
  - How do the gravitational potential stresses correlate with topographic structures on Mars?
- What are the most likely epicenters of marsquakes to be measured by InSight?
  - From what locations are the seismic waves most likely to originate?
  - What factors have an effect on the locations of seismic epicenters?
    - ◇ What is the effect of varying the average crustal and mantle density?
    - ◇ What is the effect of varying the average crustal thickness?
    - ◇ What is the effect of density anomalies resulting from gravitational fitting put in the crust or mantle?
    - ◇ What is the effect of fitting the original models with the gravitational gradient, vector of potential?
    - ◇ What is the effect of changing the brittle-ductile transition depth?
    - ◇ What is the effect of a dry or wet lithosphere?

The research plan consists out of three main phases, in parallel with the research questions. In Figure 1.4 a clear overview of the method used can be seen. The three steps are (1) the interior density analysis, (2) the gravitational potential stresses calculation and (3) the seismic analysis by use of yield stress envelopes.

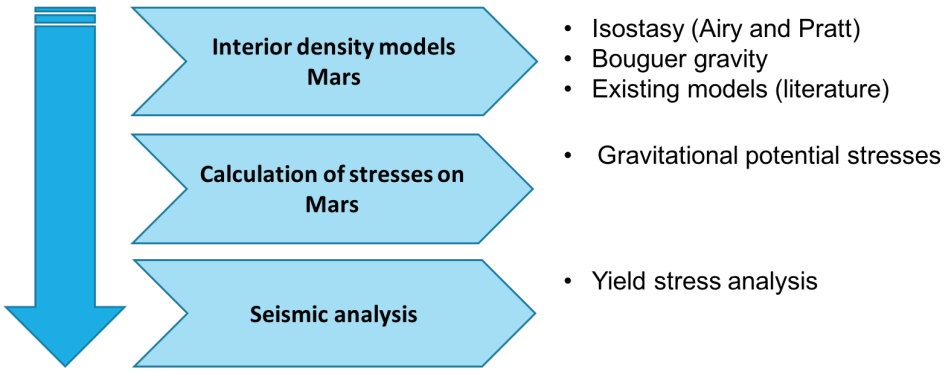

Figure 1.4: Overview of the three main steps out of which the thesis project consists. First, an interior density model analysis has to be performed, followed by the calculation of gravitational potential stresses on Mars. Finally, a seismic analysis is made by use of yield stress envelopes.

In this report the structure of these three phases can clearly be seen. First of all, in Chapter 2, the input data used in this research is discussed. The input data consists out of topographic and gravitational data. Also, the

method to represent this data is discussed, for the gravitational data this also implies the relation between interior density and gravity. Next, in Chapter 3, the entire method is discussed in more detail. This chapter consists out of three sections analogue to the research questions: (1) the creation of interior density models, governing isostatic principles, the Bouguer gravity and existing models by literature, (2) the gravitational potential theory and (3) the method to perform a seismic analysis using Byerlee's law. In the next section, the method of how to fit these models to the gravitational potential is discussed, followed by a summary of all model parameters used to answer each research question. In Chapter 4, the results of the research are given. This chapter starts with the three main steps of the research, and ends with a combination of all results where emphasis is put on answering the research questions. In Chapter 5 the results are discussed by putting them in perspective with previous research performed towards seismicity on Mars. The thesis will be concluded in Chapter 6 where a final answer to the main research question is given. Finally, in Chapter 7, recommendations for future research are given. The interested reader can find more information on the verification and validation of all software used in the Appendix, together with a more elaborate exploration of spherical harmonics. In the last appendix, the exact coordinates of often used locations in this research are given.

2. INPUT DATA

The input data used for this research consists of topography data and gravity data. In this chapter both the data sets are discussed, together with how they are represented and how this data can be used.

2.1. TOPOGRAPHY

First of all, the topography of Mars is used in this research. The Martian topography was analyzed by the Mars Orbiter Laser Altimeter (MOLA), an instrument on the Mars Global Surveyor (MGS). The MOLA instrument was functional until 2001. It works by sending a pulse back and forth to Mars and analyzing the travel time of the signal. Using this technique, the altitude of the spacecraft above Mars could be determined with an uncertainty of 30 meters. Combining this data and images from Mars (for example from HiRise on MRO), the topography up to spherical harmonic degree and order 2600 is defined. The data can be downloaded through Marc Wieczorek his Github account.[4]

In Figure 2.1 the topography is shown in high resolution. The elevations are shown with respect to the Martian areoid (see Section 2.2). The hemispheric dichotomy can clearly be seen. The northern lowlands are characterized by only few impact craters, whereas the southern highlands have many. This is an indication to the younger surface age of the north. Also clearly visible is the Tharsis rise with its three volcanoes and the Olympus Mons volcano. East of the Tharsis volcanoes, Valles Marineris reaches great depths. The InSight landing site is southwest from Elysium Mons. The impact basin Hellas Basin (Hellas Planitia) is the lowest topographic feature on the map.

2.2. GRAVITY

First of all, a general introduction into gravitational data is given before discussing the gravitational data of Mars. Equation 2.1 up to 2.9 are all from Root (2018). Gravitational force between two masses, m_1 and m_2, is best known as the second law of Isaac Newton:

$$F = G\frac{m_1 m_2}{r^2} \tag{2.1}$$

Where $G/(m_1 r^2)$ is the acceleration of m_1 on m_2 directed towards m_2 and $G/(m_2 r^2)$ is the acceleration of m_2 on m_1 directed towards m_1. Gravitational potential is also related to Newton's second law. Gravitational potential due to a mass, m_1, is defined as follows:

$$V = -\frac{Gm_1}{r} \tag{2.2}$$

Related to this is the gravitational potential energy on a second mass, m_2, due to m_1:

$$U = -\frac{Gm_1 m_2}{r} \tag{2.3}$$

When taking the derivative of the gravitational potential with respect to the radius, r, the gravity acceleration is found:

$$g = -\frac{\delta}{\delta r}V = -\frac{Gm_1}{r^2} \tag{2.4}$$

In three dimensions this becomes:

$$a = -grad(V) = -\nabla V \tag{2.5}$$

The gravitational potential can also be written as follows (Root, 2018):

$$V(x) = G\iiint_{\Omega}\rho(x_Q)\frac{1}{l}d\Omega(x_Q) \tag{2.6}$$

[4]URL https://zenodo.org/record/997406#.WtCj3pNuY1I [13-04-2018]
[5]URL https://attic.gsfc.nasa.gov/mola/images.html [08-04-2018]

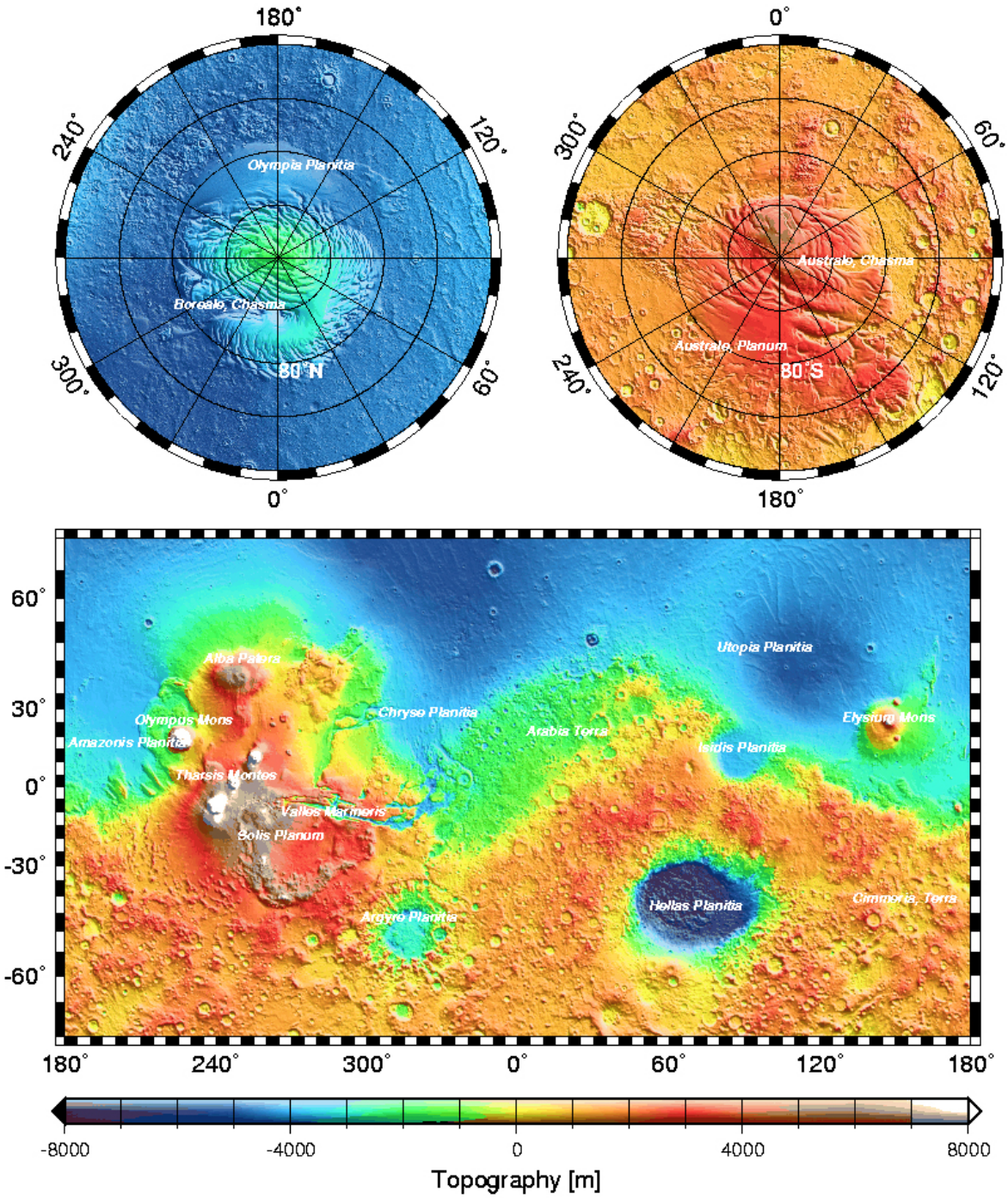

Figure 2.1: High resolution MOLA topographic data.[5] In the top figures, the two poles are seen, in the bottom figure, a complete map of Mars is shown. Mars has a hemispheric dichotomy, meaning that there is a large difference in altitude between the north and the south. The north has a lower altitude and less craters compared to the south, indicating that it is younger of age. High topographic rises are seen in the Tharsis region and at Olympus Mons, which is the highest volcano of the Solar System.

Important to keep into account is that there is also a centrifugal potential due to the rotating motion of the Earth:

$$Z(r,\theta,\lambda) = \frac{1}{2}\omega^2 r^2 sin^2\theta \tag{2.7}$$

The gravity potential, W, is the sum of the centrifugal potential, Z, and the gravitational potential, V. The

gradient of the gravity potential leads to the surface gravity:

$$W = Z + V \tag{2.8}$$

$$g = |\nabla W| \rightarrow g_{earth} \approx 9.81\ m/s^2, g_{mars} \approx 3.71\ m/s^2 \tag{2.9}$$

When measuring gravity and gravitational potential it is important that there is consensus about what the surface of the respective planet actually is. Since planets are usually not perfect spheres, there could be some disagreement. This is why for the Earth, the concepts of the ellipsoid and geoid are used. The ellipsoid is the shape of the planet when taking the polar flattening into account. The geoid is an equipotential surface referenced with respect to the ellipsoid. An equipotential surface means that the gravitational potential is the same everywhere on this surface, as is hidden in the name. The gravitational potential is representative to the areoid as the areoid is equal to the gravitational potential divided by the average constant gravitational acceleration: 3.711 m/s^2. For other planets and moons the same concept of the ellipsoid and geoid can be applied. It even has been used for an asteroid as well (Karimi et al., 2017). The term *geoid* often receives another name though, for example, on Mars it is called the *areoid* and on Venus it is called the *aphroditoid*. It has to be noted that scientists are not consistent with this naming and often use *geoid* as well when talking about Mars or other celestial bodies.

In order to determine the areoid, the center of mass of the planet and topographic data is needed. The center of mass is determined by the gravity field of the planet. By combination of this data with MOLA topographic data, the Martian areoid could be constructed. The average equatorial radius is 3397 km and areoid variations up to more than 1.2 km from this radius were found (whereas geoid variations are only up to 200 m). The areoid is shown in Figure 2.2 (Wieczorek, 2007). There is a large elevation at the Tharsis region and a second but smaller elevation around Elysium Mons (sides of the figure).

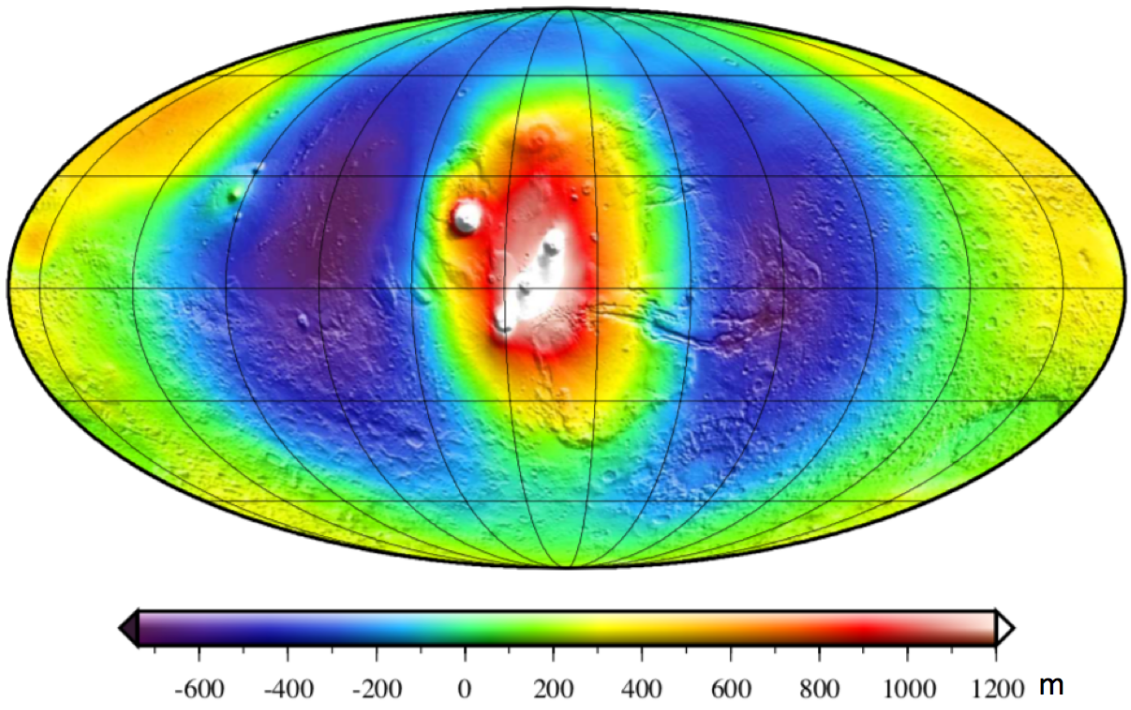

Figure 2.2: The Martian areoid, indicating the equipotential surface of Mars (Wieczorek, 2007).

The most used method to represent all this gravity data is the use of spherical harmonics (SH). Spherical harmonics is a very popular method to describe fields around a sphere, it can be seen as the Laplacian on a sphere. Besides gravity fields, also topography fields of the Earth and other planets are often described using spherical harmonics. In this research, the spherical harmonic representation is also used. In Appendix B, an introduction to spherical harmonics is given together with some often used applications of spherical harmonics. Below, the expression of the gravitational potential as a function of density in spherical harmonics

is derived. This allows for an easy way to derive the gravitational potential from density variations inside a planet. The derivation is taken from Klees (2000).

The starting point is the equation for the gravitational potential: $V = GM/r$. First of all a binomial expansion of $1/l$ is made, where l is a non-defined distance. Below, the expression $1/l$ between two points, $P(r,\theta,\lambda)$, which is the measurement point, and $Q(r_Q,\theta_Q,\lambda_Q)$, where the mass is concentrated, is written:

$$\frac{1}{l} = \left(r^2 + r_Q^2 - 2rr_Q\cos\psi\right)^{-1/2} \tag{2.10}$$

Where ψ is equal to the angle between the vectors x and x_Q. It is desired to have $1/l$ in a binomial series of monomials r_Q/r. This is done by defining $\alpha = r_Q/r$ and rewriting Equation 2.10 as follows:

$$\frac{1}{l} = \frac{1}{r}\left(1 - (2\alpha\cos\psi - \alpha^2)\right)^{-1/2} \tag{2.11}$$

Now $1/l$ needs to be developed as a power series of α. In order to do this, first of all, the binomial series of $(1-x)^{-1/2}$ when $|x| < 1$ is given:

$$(1-x)^{-1/2} = 1 + \frac{1}{2}x + \frac{1\cdot 3}{2\cdot 4}x^2 + \frac{1\cdot 3\cdot 5}{2\cdot 4\cdot 6}x^3 + ... \tag{2.12}$$

Using this and setting $|2\alpha t - \alpha^2| < 1$ and $t = \cos\psi$ results in Equation 2.13.

$$\left(1 - [2\alpha\cos\psi - \alpha^2]^2\right)^{-1/2} = 1 + \frac{1}{2}(2\alpha t - \alpha^2) + \frac{3}{8}(2\alpha t - \alpha^2)^2 + \frac{15}{48}(2\alpha t - \alpha^2)^3 + ... \tag{2.13}$$

It can be seen that this is a power series in $(2\alpha t - \alpha^2)$. By rearranging a power series in α, which converges for $|\alpha| < 1$, the following expressions can be found:

$$\left(1 - [2\alpha\cos\psi - \alpha^2]^2\right)^{-1/2} = 1 + t\alpha + \frac{3}{2}(t^2 - 1/3)\alpha^2 + \frac{5}{2}t\left(t^2 - \frac{3}{5}\right)\alpha^3 + ... \tag{2.14}$$

$$\rightarrow \left(1 - [2\alpha\cos\psi - \alpha^2]^2\right)^{-1/2} = P_0(t) + P_1(t)\alpha + P_2(t)\alpha^2 + P_3(t)\alpha^3 + ... \tag{2.15}$$

With $P_n(t)$ the Legendre polynomial. Hereof, it can be concluded that for $1/l$ the coefficients of its series expansion are the Legendre polynomials with $\cos\psi$ as argument:

$$\frac{1}{l} = \frac{1}{r}\sum_{n=0}^{\infty}\alpha^n P_n(\cos\psi) = \frac{1}{r}\sum_{n=0}^{\infty}\left(\frac{r_Q}{r}\right)^n P_n(\cos\psi) \quad \text{for } r_Q < r \tag{2.16}$$

Now that this has been derived, $1/l$ can be inserted in the equation for the gravitational potential (Equation 2.2). Assume there is a mass distribution inside a region Ω:

$$V(r,\omega,\lambda) = G\iiint_\Omega \rho_Q \frac{1}{l}d\Omega_Q = \frac{G}{r}\sum_{n=0}^{\infty}\frac{1}{r^n}\iiint_\Omega \rho_Q r_Q^n P_n(\cos\psi)d\Omega_Q \tag{2.17}$$

Note that $\rho_Q = \rho(r_Q,\theta_Q,\lambda_Q)$ and $\Omega_Q = \Omega(r_Q,\theta_Q,\lambda_Q)$ and that ψ still depends on the two points (P and Q) chosen, therefore:

$$\cos\psi = \cos\theta\cos\theta_Q + sin\theta sin\theta_Q\cos(\lambda - \lambda_Q) \tag{2.18}$$

Because of the addition theorem of Legendre polynomials the factorization of $P_n(\cos\psi)$ depending on P and Q is allowed:

$$P_n(\cos\psi) = \frac{1}{2n+1}\sum_{m=-n}^{n}\bar{Y}_{nm}(\theta,\lambda)\bar{Y}_{nm}(\theta_Q,\lambda_Q) \tag{2.19}$$

With;

$$Y_{nm}(\theta,\lambda) = \begin{cases}\bar{P}_{nm}(\mu)(\cos\theta)\cos(m\psi) & m = 0,1,...,n\\ \bar{P}_{n|m|}(\mu)(\cos\theta)sin(|m|\psi) & m < 0\end{cases} \tag{2.20}$$

And;

$$\bar{P}_{nm}(\mu) = \sqrt{(2-\delta_{0m})(2n+1)\frac{(n-m)!}{(n+m)!}}P_{nm}(\mu) \tag{2.21}$$

Where P_{nm} are the normalized Legendre functions:

$$P_{nm}(\mu) = (1-\mu^2)^{m/2}\frac{d^m}{d\mu^m}P_n(\mu) \tag{2.22}$$

$$P_n(\mu) = \frac{1}{2^n n!}\frac{d^n}{d\mu^n}(\mu^2-1)^n \tag{2.23}$$

Or, differently stated:

$$\bar{P}_{nm}(t) = H_{nm}(1-t^2)^{m/2}\frac{d^m P_n(t)}{dt^m} \tag{2.24}$$

$$H_{nm} = \begin{cases} \sqrt{2n+1} & m = 0 \\ \sqrt{2(2n+1)\frac{(n-m)!}{(n+m)!}} & m \neq 0 \end{cases} \tag{2.25}$$

Now the gravitational potential is obtained:

$$V(r,\theta,\lambda) = \frac{G}{r}\sum_{n=0}^{\infty}\frac{1}{r^n}\sum_{m=-n}^{n}\bar{Y}_{nm}(\theta,\lambda)\frac{1}{2n+1}\iiint_{\Omega}\rho_Q r_Q^n \bar{Y}_{nm}(\theta_Q,\lambda_Q)d\lambda_Q \tag{2.26}$$

Multiplying and dividing the right-hand side with Ma^n, with M a reference mass and R a reference radius the following equation is found:

$$V(r,\theta,\lambda) = \frac{MR^n}{MR^n}\frac{G}{r}\sum_{n=0}^{\infty}\frac{1}{r^n}\sum_{m=-n}^{n}\bar{Y}_{nm}(\theta,\lambda)\frac{1}{2n+1}\iiint_{\Omega}\rho_Q r_Q^n \bar{Y}_{nm}(\theta_Q,\lambda_Q)d\lambda_Q \tag{2.27}$$

From this, the following coefficients are defined:

$$\bar{C}_{nm} = \frac{1}{2n+1}\frac{1}{M}\iiint_{\Omega}\rho_Q\left(\frac{r_Q}{R}\right)^n\bar{Y}_{nm}(\theta_Q,\lambda_Q)d\lambda_Q \tag{2.28}$$

And the final expression for the gravitational potential in spherical harmonics with degree n and order m is found:

$$V(r,\theta,\lambda) = \frac{GM}{R}\sum_{n=0}^{\infty}\left(\frac{R}{r}\right)^{n+1}\sum_{m=-n}^{n}\bar{c}_{nm}\bar{Y}_{nm}(\theta,\lambda) \tag{2.29}$$

An important note is that in literature several different final equations of the gravitational potential in spherical harmonics are given. Therefore, it is important to think thoroughly about what kind of data and equations are being used before starting to model. Also, it is still not known how to calculate Equation 2.28. Methods to solve this part of the spherical harmonic equations are discussed by Sneeuw (1994). He proposes several methods of which the weighted least-squares was selected by Root et al. (2016) to be used in their software. For more information on the weighted least-squares the reader is referred to Sneeuw (1994).

Regarding the spherical harmonic coefficients, several common names are used, these are shortly summarized below:

- C_{nm} → positive orders
- S_{nm} → negative orders
- Zonal: C_{n0} coefficients
- Tesseral: C_{nm} and S_{nm} with $n > m$
- Sectoral: C_{nm} and S_{nm} with $n = m$

Some SH coefficients have a specific meaning, these are given below:

- Degree 0: mass of the planet

- Degree 1: depends on location of the centre of mass with respect to the origin of the coordinate system used. If the centre of mass and the centre of the coordinate system are the same: $C_{10} = C_{11} = S_{11} = 0$.
- C20: flattening of the planet. On Earth this is best known as the J2 effect. This effect is large both on the Earth and on Mars. By setting this coefficient equal to zero, the gravitational correction for flattening of the planet is approximated.
- C21, S21, C22, S22: depend on the principle axis of the moments of inertia their orientation with respect to the coordinate system used.

The low-mid degrees (1-10) point to gravity anomalies in the mantle, while the higher degrees point to small changes on the surface. Therefore, it is important to make a well thought-out decision about which degrees to use. In this project, the deeper mantle anomalies are not necessary, the order and degrees higher than 10 are used in this research.

The software written by Root et al. (2016) uses spherical harmonics to relate interior density layers to the gravitational potential. It was originally written for Earth, but it can be applied to any planet or moon. In Figure 2.3, a flow diagram of the software can be seen. The first step in this software is the creation of the input model, which contains the following data:

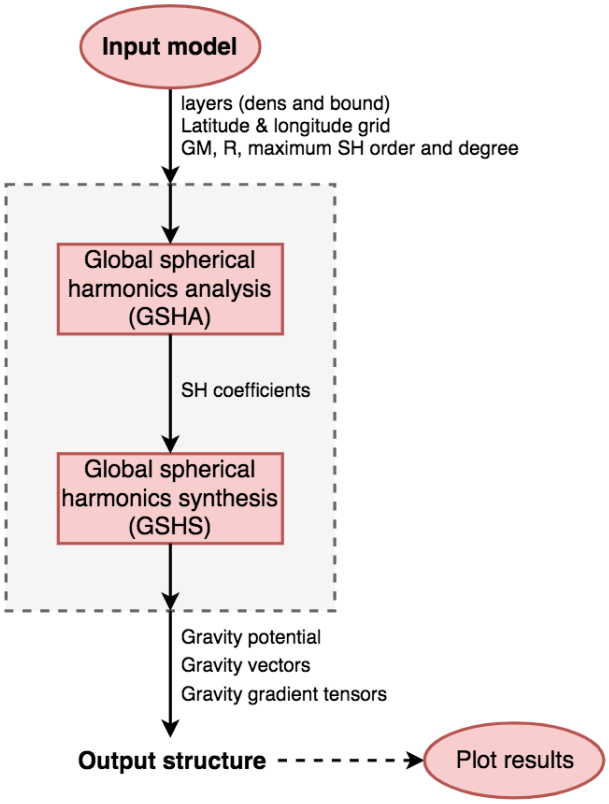

Figure 2.3: Flow diagram of the software created by Root et al. (2016). This software can be used to calculate the gravity field of a planet or moon from its interior density structure. Firstly, the spherical harmonic coefficients are calculated from input density layers (GSHA) and secondly, the gravity field is calculated using these coefficients (GSHS).

- Number of layers
- Latitude and longitude
- Files in `.txt` or `.gmt` format containing ASCII data on all boundaries and density profiles of each layer
- Standard gravitational parameter, GM (on Mars: $4.2828 \cdot 10^4$ km^3/s^2)

- Radius (Mars: $3.39600 \cdot 10^3$ km)
- Minimum and maximum spherical harmonics order and degree, n_{min}, n_{max}

The second step is the Global Spherical Harmonics Analysis (GSHA). By use of this function, the spherical harmonics coefficients of the input model are constructed (see Equation 2.28). For this, the weighted least-square method proposed by Sneeuw (1994) is used. Next, the Global Spherical Harmonics Synthesis (GSHS) is performed, where most importantly the gravitational potential is calculated using Equation 2.29. From the GSHS comes the output file, which is a Matlab structure. This output file can easily be used to create plots or as input in other programs. The output object contains the following items:

- Latitude and longitude
- Radius
- Gravitational potential
- Gravitational vectors (first derivative of the gravitational potential: R, T, L, X, Y and Z)
- Gravitational tensors (second derivative of the gravitational potential: T_{rr}, T_{tt}, T_{ll}, T_{rt}, T_{rl}, T_{tl}, T_{xx}, T_{yy}, T_{zz}, T_{xy}, T_{xz} and T_{yz})
- Spherical harmonics bounds
- Input model

This software is used by taking into account the correction Root et al. (2016) proposed. Using spherical harmonics with degree and order up to 100, the crust and upper mantle model should have a maximum thickness of 50 km for each layer. If thicker layers are used, incorrect results will be found due to the divergence of the binomial approximation. Following this correction, a small side tool is written to iteratively split layers with a thickness greater than 50 km in two smaller layers until all layers are sufficiently small.

The software's reference system is with respect to a spherical interface and not with respect to the areoid or ellipsoid. Topographic data is usually stated with respect to the areoid. As the areoid on Mars is in the range -700 to 1100 meter above its average radius (the Geoid of the Earth is in the range -100 to 100 meter), it is no valid assumption to use topographic data with respect to the areoid. Therefore, another side tool is written to subtract the areoid from the topographic data, which leads to the topographic data with respect to a sphere with a radius of 3396 km. The areoid data used is published by NASA and is not with respect to the ellipsoid but with respect to the Martian sphere with a radius of 3396 km.[1]

Gravity data of Mars is deducted mainly from three missions: Mars Global Surveyor (MGS), Mars Odyssey and Mars Reconnaissance Orbiter (MRO). All missions used radio tracking to model the gravity field. MGS was functional from 1997 until 2006. The Doppler shift of an X-band radio link with the Earth can be analyzed, such that it is known exactly where a spacecraft is located. This allowed for gravity variations to be measured. When starting its measurements, they were used to update Viking 1 and 2 and Mariner 9 gravitational data, later on it became a full MGS model. Mars Odyssey started operations in 2001 and is operational up to now. Mars Odyssey also uses Doppler tracking. Using MGS and Mars Odyssey data, a model up to spherical harmonic degree and order 95 was created in 2005. The earlier Viking and Mariner models were up to degree and order 50. Later on, MRO, which started operations in 2006 and is still functional today (late 2018), also uses Doppler data for its gravity field analysis. A gravity model up to degree and order 120 was created in 2016 by using MRO data as well. All these models are free to download on the NASA website.[2]However, even though a model up to degree and order 120 is available, for some research purposes it is more convenient to use a lower degree and order. The lower SH degrees point to gravitational anomalies in the mantle, while the higher degrees point to anomalies in the upper mantle and crust. Therefore, only the SH degrees starting from 10 and higher are used. SH degrees up to 100 are used (in stead of 120) due to large uncertainties in degree and order 100 up to 120.

[1]URL `http://pds-geosciences.wustl.edu/missions/mgs/megdr.html` [18-09-2018]
[2]URL `http://pds-geosciences.wustl.edu/dataserv/gravity_models.htm` [14-04-2018]

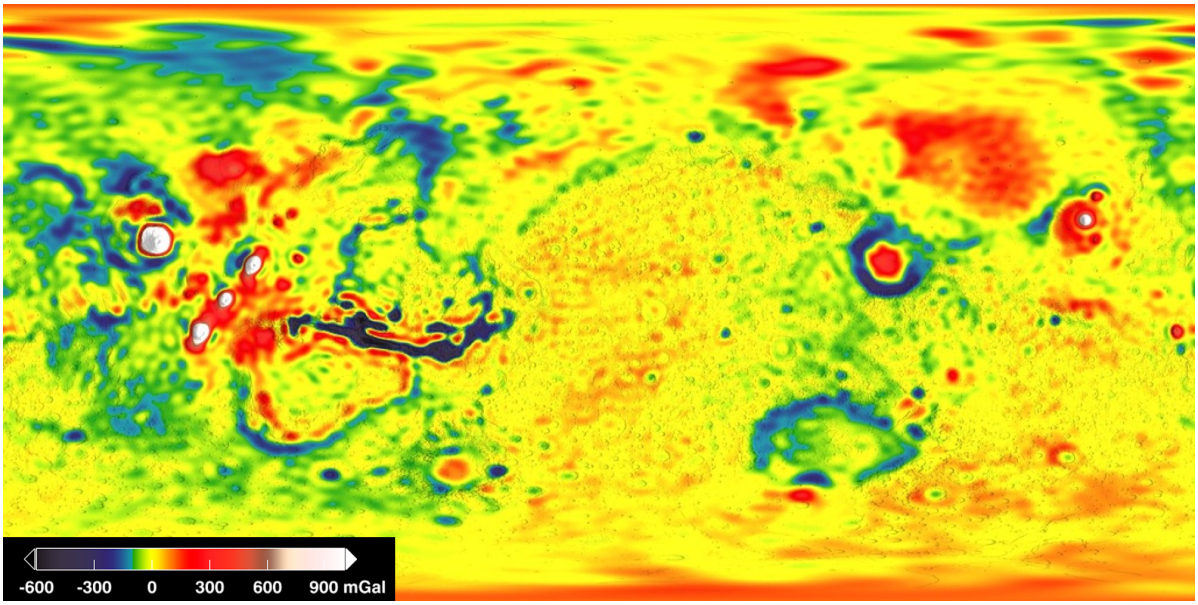

Figure 2.4: Free-air gravity anomaly map of Mars.[3] High free-air gravity anomalies are seen in the Tharsis region, Olympus Mons, Isidis Planitia, Utopia Planitia and Elysium Mons. Low free-air gravity anomalies are seen surrounding Olympus Mons, in Valles Marineris, Hellas Basin and around Isidis Planitia.

In Figure 2.4 the latest free-air gravity anomaly map can be seen.[3] It can be seen that the Tharsis volcanoes are indicated with a large free-air gravity anomaly and Valles Marineris with a large negative anomaly. It is suggested that Valles Marineris is not isostatically compensated yet. Hellas Basin has relatively small free-air anomalies, only the boundaries can clearly be seen. It can also be seen that the hemispheric dichotomy is not visible in the free-air gravity map. However, it can be concluded that in the northern lowlands there are more gravity anomalies compared to the southern highlands. This suggests that the south is more isostatically compensated compared to the north, which leads to the conclusion that the northern crust is younger than the southern crust as it had less time to reach isostatic equilibrium. This agrees with the previous section, where it is discussed that the north is younger than the south due to the lower amount of impact craters in the north.

[3] URL `https://svs.gsfc.nasa.gov/4436` [08-04-2018]

3. METHOD

The main outline of the method can be derived from the research questions. First, the interior density models need to be created by use of the Airy and Pratt isostatic principles, by use of the Bouguer gravity and by use of the Wieczorek (2015) and Goossens et al. (2017) models. Secondly, the gravitational potential stresses are calculated using the method of Pascal (2006). Third and last, the GPSt maps are compared with the yield stress envelopes created using the law of Byerlee (1978).

3.1. INTERIOR DENSITY MODELS

Before the gravitational potential stresses can be calculated, a density model of the crust and upper mantle of Mars is needed. By running this model in the Root et al. (2016) Matlab code, the resulting calculated gravitational potential can be compared with the measured gravitational potential. The residual between the calculated and measured gravitational potential can be minimized by adapting the radial density model in order to find the best fit. There are different methods to create interior density models: using Airy and Pratt isostasy, using the Bouguer gravity anomaly and using models created by other authors (here: Wieczorek (2015) and Goossens et al. (2017)). After evaluating all the methods, it is decided to create a set of different models focused on specific research questions. For each model, the most probable marsquake locations and governing stresses are identified. The relations of varying parameters in the different models with the final results are then analyzed. The research questions which have to be tackled in this part of the research are the following:

- What is the effect of varying the average crustal and mantle density?
- What is the effect of varying the average crustal thickness?
- What is the effect of density anomalies resulting from gravitational fitting put in the crust of mantle?
- What is the effect of fitting the original models with the gravitational gradient, vector of potential?

In this section, the theory of isostasy is explained, followed by an explanation on how to make interior density models by using the Bouguer gravity. Next, the state of the art interior density models are discussed, after which a method to fit all models to the gravitational potential is elaborated on. As last, a summary of all models used to answer each research question (presented above) is given.

3.1.1. ISOSTATIC MODELS

The theory of isostasy explains the establishment of a gravitational equilibrium by the lithosphere floating on the asthenosphere: at a certain depth the pressure is the same on the entire planet. The best example is a mountain which is underlain by a thick light root such that an equal buoyancy is reached. Up to today there is still not one single model for isostasy; there are three main ideas which are all three being used. These principles are the following: (1) Airy isostasy, (2) Pratt isostasy and (3) flexural isostasy. Airy and Pratt isostasy relate to local compensation while flexural isostasy relates to regional compensation.

In Figure 3.1, a schematic of Airy and Pratt isostasy can be seen (Close, 2010). Airy and Pratt both imply that at a certain depth the pressure of the lithosphere is the same at each place on the planet. The Airy isostatic theory implies that topography is a function of lithospheric thickness. Following this idea, a high mountain should be underlain with a thick root and a basin with a very small root. The combination of a higher constant density in the mantle and a lower constant density in the crust results in the same pressure (weight) applied at a certain depth. This can most easily be compared to a raft of wood floating on water, where the parts sticking out highest have the deepest roots and vice versa. In Figure 3.1a it can be seen that all the bars have an equal density. The compensation depth, D_c, is a measure for the depth where all topography has been compensated, this is equal to the deepest root of the system. The equations related to Airy isostasy are stated below (Watts, 2001):

$$\rho_m = \rho_c + \Delta\rho_{c-m} \tag{3.1}$$

$$r = \frac{h\rho_c}{\rho_{c-m}} \tag{3.2}$$

$$t_{crust} = r + t_{avg} + h \tag{3.3}$$

Where ρ_m and ρ_c are the mantle and crustal density respectively and ρ_{c-m} is the crust-mantle density contrast. The variable part of the crustal thickness is expressed as r, h is the altitude, t_{crust} is the final crustal thickness and t_{avg} is the average crustal thickness. Using this method an average crustal thickness needs to be assumed, as this is used as a reference value for the crustal thickness at each specific location. Since the crustal density is lower than the mantle density, the root of a mountain is thicker than the elevation of that mountain.

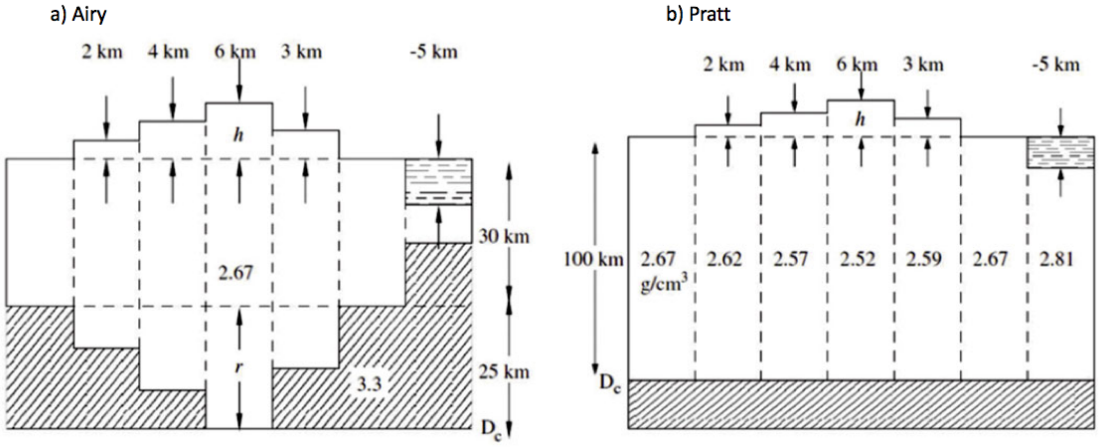

Figure 3.1: (a) Airy and (b) Pratt isostatic models (Close, 2010). The striped area is the asthenosphere and the white area the lithosphere. D_c is the compensation depth. The Airy theory says that every column has the same density but a different crustal thickness. The Pratt theory says that every column has the same crustal depth (= compensation depth) and a different crustal density.

The Pratt theory is shown on the right side of Figure 3.1b. Here, the crustal root of each column depth reaches up to the compensation depth, D_c. In order for the mass of each column to be the same, the densities of each column differ. When applying this theory, topographic elevations have a lower density and topographic lows have a higher density. The crustal density for each column can be calculated as follows (Watts, 2001):

$$\rho_{c_{h>0}} = \rho_{avg}\frac{D_c - h}{D_c} \tag{3.4}$$

$$\rho_{c_{h<0}} = \rho_{avg}\frac{D_c}{D_c + h} \tag{3.5}$$

It can be seen that for positive and negative topography a different equation has to be used. In these equations, ρ_{avg} is the average crustal density which needs to be assumed. The compensation depth, D_c, also needs to be assumed. Following this theorem; if the density of a column decreases, for example due to heating from below, the altitude of that column will increase. Using the Pratt theorem, it needs to be kept into account that the compensation depth is deep enough such that realistic densities are found. With a shallow compensation depth, very high outliers in density are found which only match with fluids (low density) or metals (high density). D_c can be determined by looking at reference values in literature and by iterating up to a depth where reasonable density variations in the crust are found.

Opposed to the Airy and Pratt theories, flexural isostasy implies regional compensation instead of local compensation. When assuming a lithosphere with a finite strength or rigidity, compensation will cover a wider region than only straight below the mass deficit or bulge to be compensated for. In Figure 3.2 an illustration of regional compensation of a load due to flexural isostasy can be seen, in the same figure the Airy model is also displayed. Related to flexural isostasy is the theory of elastic plates. This theory its best performing model is the thin-plate model. In the thin-plate model perfect elasticity is assumed and it is assumed that the radius of curvature is large compared to the plate thickness. Furthermore it is assumed that the stress in the

horizontal direction is very small and can be neglected (Watts, 2001; Watts and Moore, 2017). As the flexural theory is worth a whole thesis on its own, this theory is not used in this project. Using flexural theory would also result in large scale stress maps while for this research small scale, local stresses are needed. Despite it not being used, it is still worth noting for possible future research.

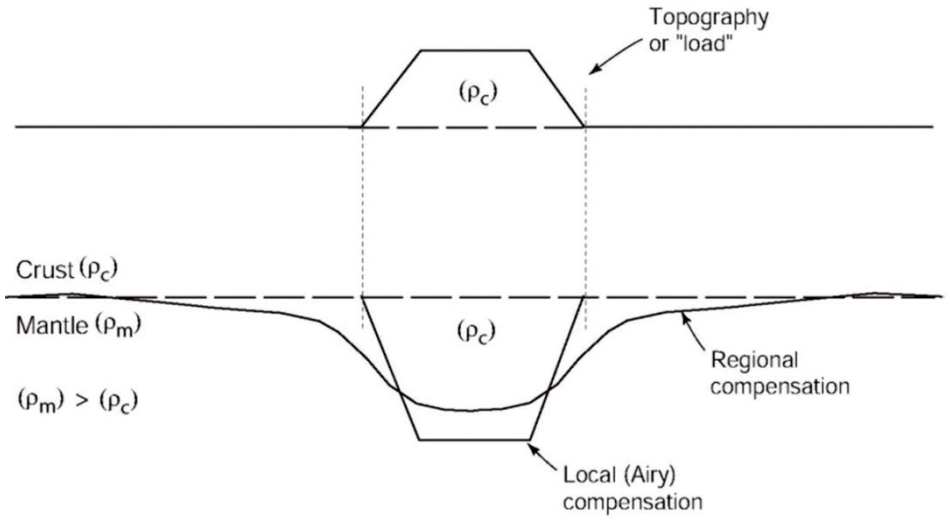

Figure 3.2: Regional compensation of a load in the flexural isostatic model compared to the Airy model (Close, 2010). Whereas Airy assumes that the lithosphere has no strength and compensation is only local, flexural theory assumes that the lithosphere has a finite strength which as follows results in regional compensation.

In literature all three theories are still widely being used (Close, 2010; Watts, 2001; Watts and Moore, 2017). Whereas Airy and Pratt assume that topography is compensated locally and thus the lithospheric material is brittle, the flexural isostasy and elastic plate theories imply that the lithosphere consists out of elastic material. Both assumptions have their strengths and weaknesses: at some temperatures and pressures certain materials are indeed elastic, but other materials are not. However, consensus is reached that the Airy theory overall works best on the Earth, except at mid-ocean ridges, where the Pratt theory proves to be true Watts (2001).

Important to keep into account is that there can also be mass variations in the mantle, which is well below the compensation depth of the previously mentioned models. Root et al. (2017) performs research towards this matter and uses density anomalies added in the lithospheric mantle when fitting models to the gravity field (see also Figure 3.6). Apart from this article, not much information or models can be found on density anomalies in the upper mantle. This also means that a lot of research can and will still be performed regarding isostatic models.

Knowing whether or not and how an area is isostatically compensated leads to conclusions about the crustal thickness of an area. This is important for stress modelling of the area. Knowing the stress field gives more indications towards places where quakes will most likely occur, which is an important conclusion to be made during the master thesis research. The best way to learn about the compensation of certain areas is by combining gravity and topography data. Topography indicates whether or not there is something to be compensated for and gravity indicates what is happening below the topography. Below, the method used in this research to make conclusions about isostatic compensation is discussed.

Seeing whether or not a region is isostatically compensated can be done by looking at the isostatically modelled gravity field. By looking at topography and using the equations for Airy or Pratt isostasy, a model can be created of what the gravity field should look like if it was perfectly compensated by using the software of Root et al. (2016) (see Section 2.2). As follows, isostatic gravity anomalies can be calculated by taking the difference between the observed gravity field and the isostatically modelled gravity field. If the difference is zero, the load is locally isostatically compensated. If the difference is not zero, there are three options; (1) it could be that there is regional compensation, (2) it could be that the region is not compensated yet or (3) it could be

that there is a density anomaly in the lithosphere of which there are no visible features. If there are no visible features this anomaly cannot be modelled by an isostatic model since there is no clue of anything happening at all (Close, 2010). In this thesis, only the Airy and Pratt isostatic principles are used to model the interior density of Mars, as mentioned before. The gravity field derived from these models is then compared to the actual gravity of the planet. Differences between the calculated and actual gravity indicate the amount of isostatic compensation on Mars.

3.1.2. BOUGUER GRAVITY MODELS

Once the gravitational map of a planet is created, as explained in Section 2.2, there are several reductions in order to improve insight into deviations. There are three main reductions: (1) the reduction for latitude and rotational velocity, (2) the free-air correction and (3) the Bouguer correction. It is important to check how gravity data has been modified and how it was measured before using it for calculations. All three reductions lead to a different view on gravitational anomalies. They are presented below, together with notes on why they are useful. The information is derived from Fowler (2005) unless stated otherwise.

First of all, gravity corrections start with the observed gravity: g_{obs}. On the observed gravity, corrections for instrumental drift and tides have already been performed. Then, the first correction takes the elliptical shape, the rotation of the planet and the mass increase around the equator (in the equatorial bulge) into account. It is represented using the following equation:

$$g(\phi) = g_{obs}\left(1 + \alpha sin^2(\phi) + \beta cos^4(\phi)\right) \tag{3.6}$$

Where ϕ is the latitude of the observation point and the values of α and β are planet dependent. Note that whether or not this correction is necessary depends on whether gravity is measured from space or from the surface of the body. On the Earth, gravity measurements are performed on the surface, however for other planets, so far, measurements have been performed from space. From space only the gravitational anomalies due to flattening of the planet are measured: gravity can also be corrected for this by taking away the effect of the C20 term of the spherical harmonics coefficients.

The second reduction is the free-air reduction, where the gravity at sea level is approximated. If there is a mountain, the gravity effect of this mountain is taken away until the gravity at sea level is known. In Equation 3.7 the free-air correction, δg_F, is shown. The free-air anomaly, g_F, can be seen in Equation 3.8.

$$\delta g_F = g_0 - g(h) = \frac{2hg_0}{R} \tag{3.7}$$

$$g_F = g_{obs} - g(\phi) + \delta g_F \tag{3.8}$$

Next, there is the Bouguer correction. The Bouguer reduction takes into account that the mass which is corrected for in the free-air gravity, also has a gravitational effect. It represents the gravity effect of all the mass below sea-level. In Equation 3.9 a simplification of the Bouguer correction is shown.

$$\delta g_B = 2\pi G\rho h \tag{3.9}$$

Here, it is assumed that the Bouguer correction is only made for mass directly above or below the point it is being calculated for. The software of Root et al. (2016) can also be used to calculate the Bouguer gravity anomaly more correctly compared to the topographic reduction shown in Equation 3.9. This can be done by creating two layers as shown in Figure 3.3: (1) a layer with everything above topographic zero and a zero boundary for all places with negative topography (orange in Figure 3.3) and (2) a layer with everything under topographic zero and a zero boundary for everything with positive topography (green in Figure 3.3). For the first layer (all positive topography) the density is equal to the positive crustal density, in the second layer (all negative topography) the density is set equal to the negative crustal density. By calculating the gravitational signal of only these two layers, the Bouguer correction can be calculated. This can, subsequently, be subtracted from the free-air gravity, resulting in the Bouguer gravity anomaly. This method is more complicated but also more precise than the topographic Bouguer correction. Whereas the simple Bouguer correction only looks at the point where it is being calculated for, the more elaborate Bouguer correction also takes into account its surroundings (the terrain correction). Therefore, this method is used in this research.
As last, there is also the terrain correction, which allows for derivations of the gravity due to variations in topography near each observation point. There is no simple equation for δg_T, it is computed with the use of

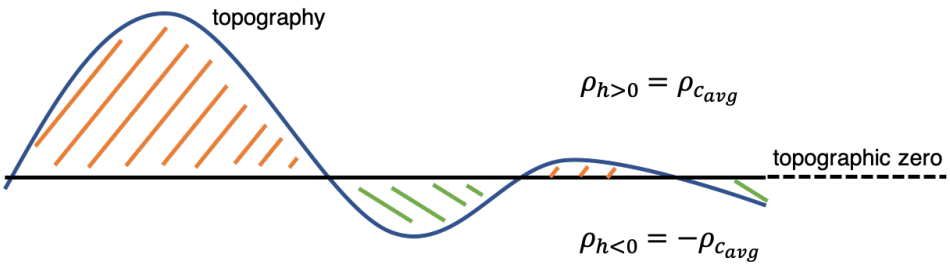

Figure 3.3: Two layers used to calculate the Bouguer correction. The density of the positive topographic layer is equal to the positive crustal density and the density of the negative topographic layer (green) is equal to the negative crustal density. These two layers are used in the software of Root et al. (2017) in order to calculate the Bouguer correction (see also Figure 2.3).

models. It is especially useful in mountain terrains. Finally, taking all these corrections into account (latitude and rotational velocity, free-air, Bouguer and terrain) the Bouguer anomaly can be calculated:

$$g_B = g_F - \delta g_B + \delta g_T = g_{obs} - g(\phi) + \delta g_F - \delta g_B + \delta g_T \tag{3.10}$$

The Bouguer gravity anomaly is especially useful to study gravity signatures which are completely unrelated to topography since all topographic effects are taken away. Therefore, the Bouguer anomaly is a popular tool used by a lot of Earth scientists. Studying the Bouguer anomaly on Mars leads to more knowledge of the interior of the planet as it is a signature for mass and density anomalies which are not expressed in topography. Hence, the Bouguer gravity can be used to calculate the crustal thickness by assuming that it only represents crustal thickness variations. As the Bouguer gravity tells us what is below the areoid, it can be used to linearly approximate the crustal thickness:

$$d_c = d_{c_{max}} + \frac{(d_{c_{min}} - d_{c_{max}})(g_b - g_{b_{min}})}{g_{b_{max}} - g_{b_{min}}} \tag{3.11}$$

$$c_t = d_c + h \tag{3.12}$$

Here, d_c stands for the part of the crustal thickness below the areoid, ie. the part described by the Bouguer gravity, in this research this part is called the depth of the crust. When this is calculated, the topography is added to the result and the final crustal thickness is found.

3.1.3. State of the art models

The last sets of models to be used are the models created by Wieczorek (2015) and Goossens et al. (2017). As mentioned before, Wieczorek (2007) created 5 models, each with a different crustal density and average crustal thickness. One of the models has a higher crustal density in the north compared to the south, which is a Pratt-like assumption as the topography in the north is lower compared to the topography in the south. In Figure 3.4 the crustal density and crustal thickness maps of these five models are shown. In the right column, the difference between the actual gravitational potential and the calculated gravitational potential (using Root et al. (2016)) for each model is shown. The model with the highest crustal density also has the highest average crustal thickness, this is because the same amount of mass needs to be accounted for with respect to the entire planet. A lower crustal density leads to a lower average crustal thickness as mantle material is denser compared to crustal material. However, the model with the highest crustal density shows the highest residuals, indicating that this model has the worst fit with the gravitational potential. The residuals of the model using a different crustal density in the north and south are not significantly higher than the residuals for the first three models, pointing towards the fact that a density dichotomy on Mars could indeed be happening. Comparing all five models with each other also indicates that divergent interior density models can have an equally good fit with the gravitational potential, confirming the non-uniqueness of gravity.

Goossens et al. (2017) created one model which has a lower average crustal density compared to other literature. The crustal density, crustal thickness and gravitational potential residual maps of this model are shown in Figure 3.5. The crustal density is significantly lower compared to the models of Wieczorek (2015) and with variations around the topographic highs. Higher densities are used around the volcanoes of Mars as these

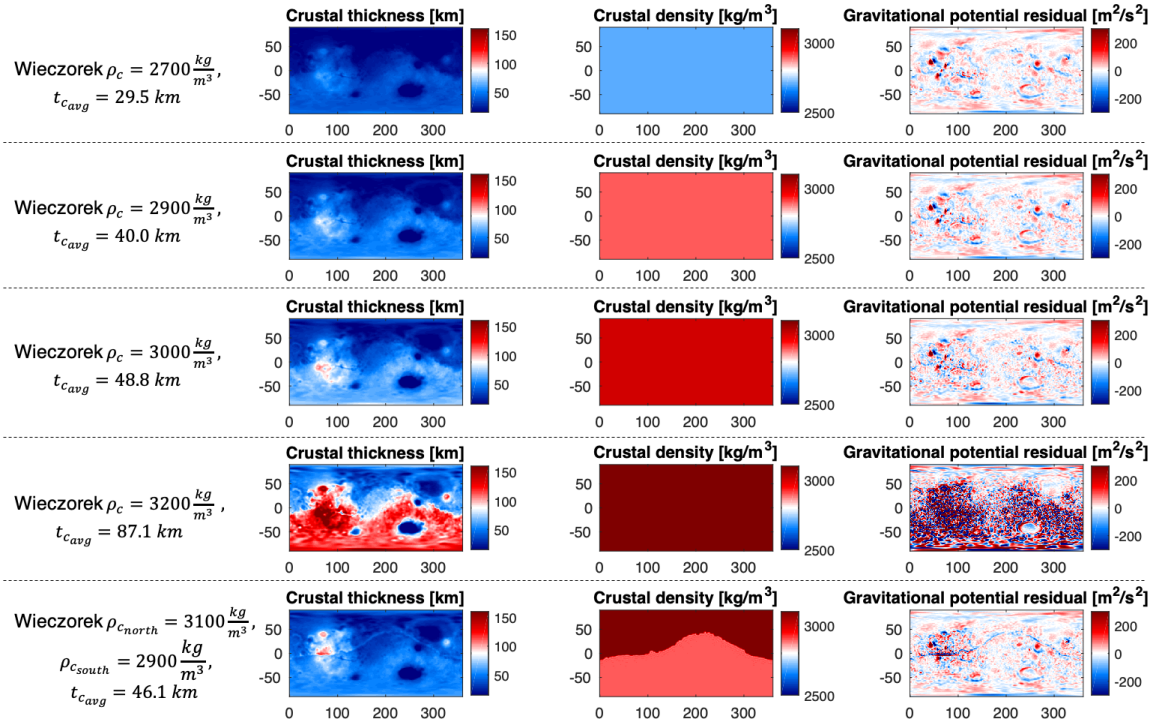

Figure 3.4: The crustal thickness, crustal density and residual of the gravitational potential of the models from Wieczorek (2015). Five different models are used, each with a varying average crustal thickness and average crustal density. The mantle density for all models is equal to 3498 kg/m^3. The model with the highest average crustal thickness and density (fourth row), results in the highest residuals with the gravitational potential, indicating that this is the least performing fit. The gravitational potential residuals of the model using a density dichotomy (fifth row) are similar compared to the first three models, indicating that a density dichotomy is equally likely as a crustal density which is the same over the entire planet.

are presumed to exist out of upcoming lava flows. The gravitational potential residual is higher compared to the models by Wieczorek (2015), this is because Wieczorek (2015) created his models by using the Bouguer gravity, while Goossens et al. (2017) did not.

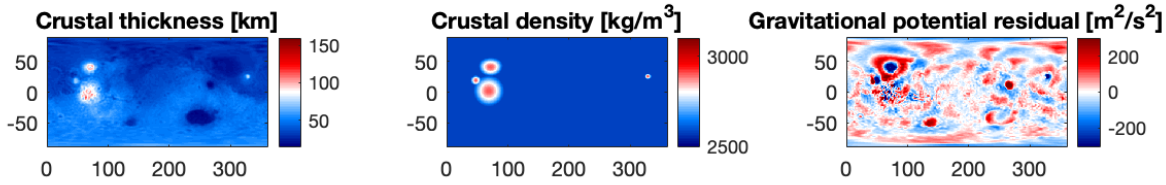

Figure 3.5: The crustal thickness, crustal density and residual of the gravitational potential of the model from Goossens et al. (2017). They created one model, using an average crustal thickness of 2582 kg/m^3. The density around the Martian volcanoes is higher as they exist out of upcoming lava. Relatively high gravitational potential residuals are found when using this model.

3.1.4. Fitting models to the gravitational potential

After each model has been created, the model is fitted to the measured gravitational potential. This is done by using the method of Root et al. (2017). In Figure 3.6 a flow diagram of this method can be seen. The first step is to make assumptions on the density in the crust and upper mantle; these are different for each model as shown in Table 3.1. This leads to an interior density model from which the gravitational potential can be calculated using the software of Root et al. (2016). This can then be compared with the actual (measured) gravitational potential, which results in a residual. Using Equation 3.13 a density anomaly can be calculated for each point on the density map, this is added to the crust or mantle of the original density model from where another iteration can start. In Equation 3.13, i stands for the number of the iteration, ρ is the density

anomaly, σ is the scaling factor, $V_{measured}$ and $V_{calculated}$ are the measured and calculated gravity respectively. The scaling factor makes sure that the iteration process goes as fast as possible.

$$\delta\rho_i = \sigma \frac{V_{measured} - V_{calculated,i}}{|V_{measured} - V_{calculated,i}|_{max}} \tag{3.13}$$

Density limits for the newly calculated density models are set to +200 and -200 kg/m^3 of the original model, as otherwise unrealistic densities are found. The density anomaly can be added to the crustal layer or to the mantle layer, for which different results will be found. Also, different results will be found by fitting the model with the gravitational potential, the gravity gradient or the gravity vector. Therefore, finding the sensitivity to the results from changing both these parameters are also two separate research questions as mentioned before. The default method used is fitting the interior density models to the gravitational potential by putting density anomalies in the crust. Usually about 10 to 20 iterations are needed for each model to converge. It can be seen whether convergence is reached by looking at the root mean square value (RMS) of the change in density: while this value is decreasing with iterations, a better solution is still found each iteration, once this value starts increasing with iterations the solutions with the minimum RMS value is the optimum solution for the interior density model.

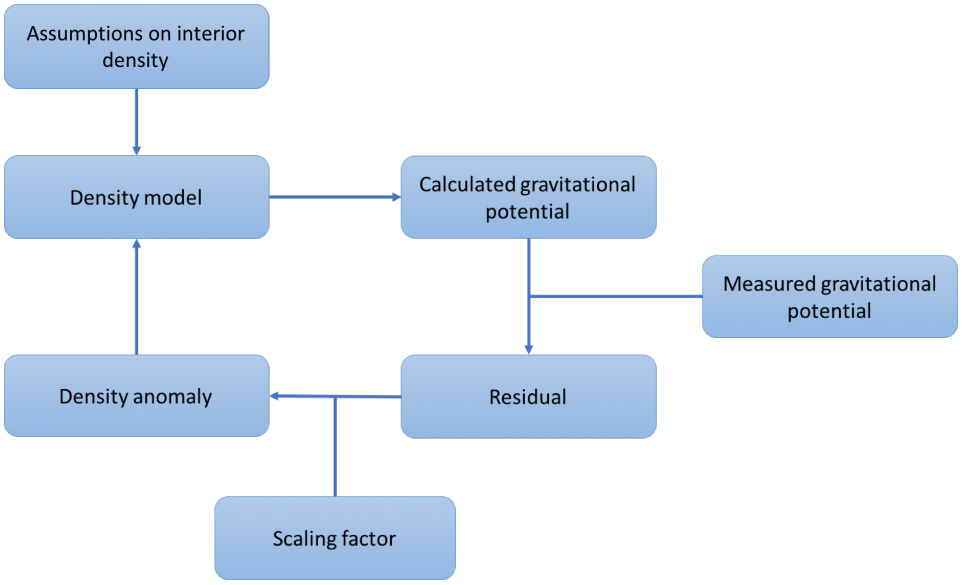

Figure 3.6: Flow diagram for fitting an interior density model to the gravitational potential, using the method of Root et al. (2017). The gravitational potential is calculated using the interior density structure, after which it is compared with the measured gravitational potential. Analogue to the gravitational potential residual, density anomalies are added to the interior density model. This method is iterated until an optimum solution for the interior density model is found.

3.1.5. Summary of model parameters

In Table 3.1, an overview of the different kinds of interior density models is given. For each model, the constant input data is given as well as the variable input parameters. Constant inputs are the ones which are measured and where literature is sure of its value. Variable parameters are values which can be changed as their correct value has not been confirmed by measurements yet. In Table 3.1 the equations or algorithm used are also shortly described together with the output parameters of each model, which is either the crustal thickness, crustal density or both. The Airy, Pratt and Bouguer models are used as end members in this research: their results will not be realistic but can be used in order to test the effect of certain varying parameters. In Figure 3.7 a schematic overview of the layers used in each model is shown. Each model, except Pratt, initially exists out of two layers before it is split into multiple layers which are all thinner than 50 km at each location of the planet. The Pratt model initially only exists out of one layer before it is split in layers smaller than 50 km. Also note that for the Bouguer model, the minimum crustal depth has to be deeper than the maximum topographic depth in order to avoid a negative crustal thickness at certain locations.

Model	Input data	Variable parameters	Method	Result
Airy	h	ρ_c, ρ_m, $t_{c_{avg}}$	$r = \frac{h\rho_c}{\rho_m - \rho_c}$, $t_c = r + t_{c_{avg}} + h$	t_c
Pratt	h	$\rho_{c_{avg}}$, D_c	$\rho_{c_{h>0}} = \rho_{avg}\frac{D_c - h}{D_c}$, $\rho_{c_{h<0}} = \rho_{avg}\frac{D_c}{D_c + h}$	ρ_c
Bouguer	h, g_F, G	ρ_c, $d_{c_{max}}$, $d_{c_{min}}$	Using software Root et al. (2016) for g_B $d_c = d_{c_{max}} + \frac{(d_{c_{min}} - d_{c_{max}})(g_B - g_{B_{min}})}{(g_{B_{max}} - g_{B_{min}})}$ $c_t = d_c + h$	t_c
Wieczorek (2015)	g, h	ρ_c, $t_{c_{avg}}$	Using Bouguer gravity and iterations while eliminating short wavelength amplifications	t_c
Goossens et al. (2017)	g, h	-	Using the SH admittance between the topography and gravity data	t_c, ρ_c

Table 3.1: Overview giving the input and output parameters and method of each type of interior density model: Airy, Pratt, Bouguer, Wieczorek (2015) and Goossens et al. (2017).

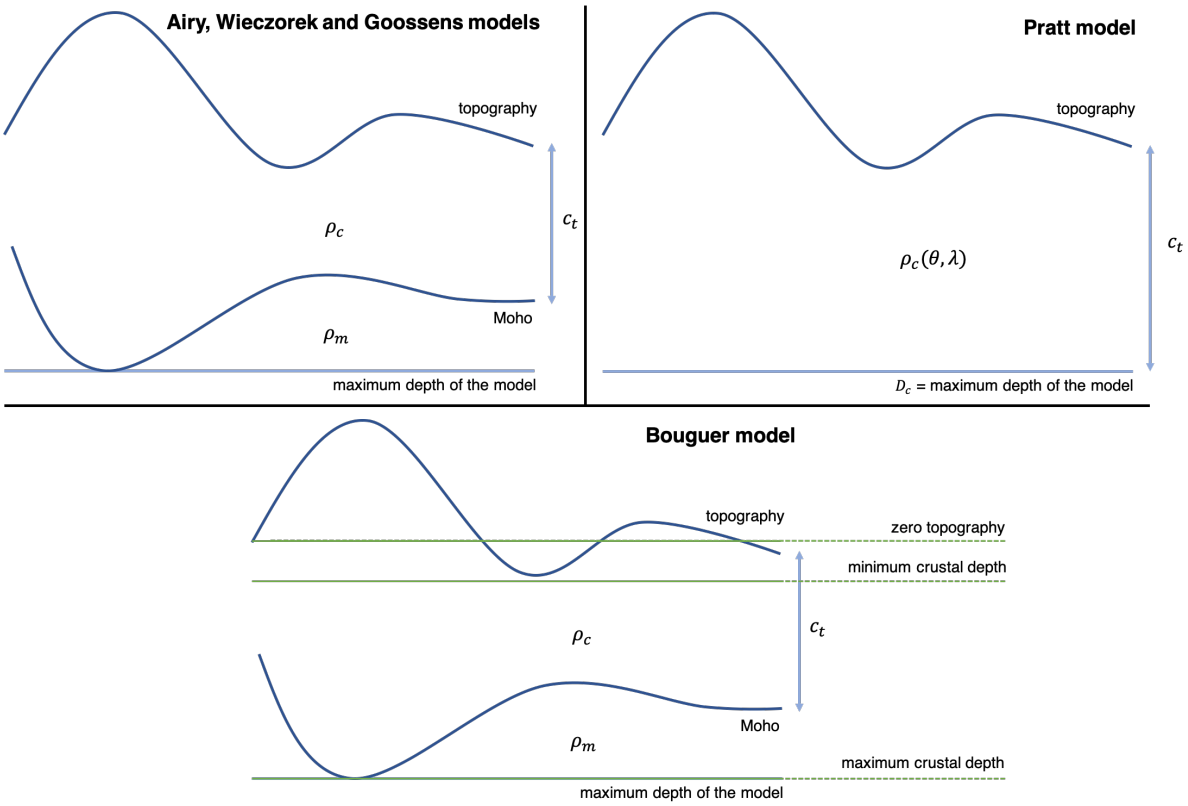

Figure 3.7: Schematic overview of each type of interior density models. The Airy, Wieczorek (2015) and Goossens et al. (2017) models consist out of a similar structure; important parameters are the Moho, the crustal density and mantle density. The Pratt models consists only out of crust; its important parameters are the crustal density and the compensation depth. The Bouguer models their important parameters are the Moho, crustal and mantle density and the minimum and maximum crustal depth. It is important that the minimum crustal depth is lower than the lowest topographic feature of Mars, otherwise negative crustal thicknesses are found.

The question left to be answered is which are the interesting models to create and test for seismicity for each research question. Below, each research question is discussed.

What is the effect of varying the average crustal and mantle density? As can be seen in Table 3.1, the den-

sity is a variable input parameter for every model. Therefore, for this question every model is tested with a different (average) crustal and/or mantle density. In Table 3.2 an overview of the models used with different parameters can be seen. The constant average crustal thickness is chosen to be 45 km as in literature, this is the most often used value. The minimum and maximum crustal thickness are usually 3 and 100 km respectively (Goossens et al., 2017; Neumann et al., 2004; Wieczorek, 2015).

Model	Variable inputs
Airy 1	$\rho_c = 2500$ kg/m^3, $\rho_m = 3000$ kg/m^3, $t_{avg} = 45$ km
Airy 2	$\rho_c = 2500$ kg/m^3, $\rho_m = 3200$ kg/m^3, $t_{avg} = 45$ km
Airy 3	$\rho_c = 2800$ kg/m^3, $\rho_m = 3300$ kg/m^3, $t_{avg} = 45$ km
Airy 4	$\rho_c = 2800$ kg/m^3, $\rho_m = 3500$ kg/m^3, $t_{avg} = 45$ km
Airy 5	$\rho_c = 3100$ kg/m^3, $\rho_m = 3600$ kg/m^3, $t_{avg} = 45$ km
Airy 6	$\rho_c = 3100$ kg/m^3, $\rho_m = 3800$ kg/m^3, $t_{avg} = 45$ km
Pratt 1	$\rho_{c_{avg}} = 2750$ kg/m^3, $D_c = 110$ km
Pratt 2	$\rho_{c_{avg}} = 2900$ kg/m^3, $D_c = 110$ km
Pratt 3	$\rho_{c_{avg}} = 3050$ kg/m^3, $D_c = 110$ km
Bouguer 1	$\rho_c = 2500$ kg/m^3, $\rho_m = 3000$ kg/m^3, $d_{c_{max}} = 3$ km, $d_{c_{max}} = 100$ km
Bouguer 2	$\rho_c = 2500$ kg/m^3, $\rho_m = 3200$ kg/m^3, $d_{c_{max}} = 3$ km, $d_{c_{max}} = 100$ km
Bouguer 3	$\rho_c = 2800$ kg/m^3, $\rho_m = 3300$ kg/m^3, $d_{c_{max}} = 3$ km, $d_{c_{max}} = 100$ km
Bouguer 4	$\rho_c = 2800$ kg/m^3, $\rho_m = 3500$ kg/m^3, $d_{c_{max}} = 3$ km, $d_{c_{max}} = 100$ km
Bouguer 5	$\rho_c = 3100$ kg/m^3, $\rho_m = 3600$ kg/m^3, $d_{c_{max}} = 3$ km, $d_{c_{max}} = 100$ km
Bouguer 6	$\rho_c = 3100$ kg/m^3, $\rho_m = 3800$ kg/m^3, $d_{c_{max}} = 3$ km, $d_{c_{max}} = 100$ km
Wieczorek (2015) 1	$\rho_c = 2700$ kg/m^3, $t_{c_{avg}} = 29.5$ km
Wieczorek (2015) 2	$\rho_c = 2900$ kg/m^3, $t_{c_{avg}} = 40.0$ km
Wieczorek (2015) 3	$\rho_c = 3000$ kg/m^3, $t_{c_{avg}} = 48.8$ km
Wieczorek (2015) 4	$\rho_c = 3200$ kg/m^3, $t_{c_{avg}} = 87.1$ km
Wieczorek (2015) 5	$\rho_{c_{north}} = 3100$ kg/m^3, $\rho_{c_{south}} = 2900$ kg/m^3, $t_{c_{avg}} = 46.1$ km
Goossens et al. (2017)	$\rho_c = 2582$ kg/m^3, $t_{c_{avg}} = 42$ km

Table 3.2: Models used to assess the effect of a varying density.

What is the effect of varying the average crustal thickness? The second variable input parameter which might have an effect is the crustal thickness. For the Airy model, an average crustal thickness needs to be given. For the Pratt model the compensation depth is needed as an input and for the Bouguer models the maximum and minimum crustal thickness are needed. In Table 3.3 the different input parameters are given. Here, a constant crustal density of 2900 kg/m^3 is used, as this is the most agreed upon value (Neumann et al., 2004; Wieczorek, 2007, 2015).

Model	Variable inputs
Airy 1	$t_{c_{avg}} = 35$ km, $\rho_c = 2900$ kg/m^3
Airy 2	$t_{c_{avg}} = 45$ km, $\rho_c = 2900$ kg/m^3
Airy 3	$t_{c_{avg}} = 55$ km, $\rho_c = 2900$ kg/m^3
Pratt 1	$D_c = 100$ km, $\rho_{c_{avg}} = 2900$ kg/m^3
Pratt 2	$D_c = 120$ km, $\rho_{c_{avg}} = 2900$ kg/m^3
Pratt 3	$D_c = 140$ km, $\rho_{c_{avg}} = 2900$ kg/m^3
Pratt 4	$D_c = 160$ km, $\rho_{c_{avg}} = 2900$ kg/m^3
Bouguer 1	$d_{c_{min}} = 7$ km, $d_{c_{max}} = 100$ km, $\rho_c = 2900$ kg/m^3
Bouguer 2	$d_{c_{min}} = 10$ km, $d_{c_{max}} = 100$ km, $\rho_c = 2900$ kg/m^3
Bouguer 3	$d_{c_{min}} = 7$ km, $d_{c_{max}} = 120$ km, $\rho_c = 2900$ kg/m^3
Bouguer 4	$d_{c_{min}} = 7$ km, $d_{c_{max}} = 90$ km, $\rho_c = 2900$ kg/m^3

Table 3.3: Models used to assess the effect of a varying crustal thickness.

What is the effect of density anomalies resulting from gravitational fitting put in the crust of mantle? For

this question, all models of the two previous questions will be used (Table 3.2 and 3.3). They will be fitted once by putting density anomalies in the crust and once by putting the anomalies in the mantle. For the seismic analysis, mainly the upper part of the crust is important, therefore it is expected that when fitting is done in the crust more interesting results will be found, which is why this is chosen as the default.

What is the effect of fitting the original models with the gravitational gradient, vector of potential? While fitting the data to the gravitational potential (using the method shown in Figure 3.6), the gravity gradient or the gravity vector can also be used instead of the potential. It is expected that by using the gradient, the model will be fitted better to the small surface changes. Several models are selected in order to test the influence of this variable. They are shown in Table 3.4. All are fitted to the gravity by putting density anomalies in the crust.

Model	Variable inputs	Fit with ...
Airy 1	$t_{c_{avg}} = 45$ km, $\rho_c = 2900$ kg/m^3	Gravitational tensor
Airy 2	$t_{c_{avg}} = 45$ km, $\rho_c = 2900$ kg/m^3	Gravitational vector
Airy 3	$t_{c_{avg}} = 45$ km, $\rho_c = 2900$ kg/m^3	Gravitational potential
Pratt 1	$D_c = 140$ km, $\rho_{c_{avg}} = 2900$ kg/m^3	Gravitational tensor
Pratt 2	$D_c = 140$ km, $\rho_{c_{avg}} = 2900$ kg/m^3	Gravitational vector
Pratt 3	$D_c = 140$ km, $\rho_{c_{avg}} = 2900$ kg/m^3	Gravitational potential
Bouguer 1	$d_{c_{min}} = 7$ km, $d_{c_{max}} = 100$ km, $\rho_c = 2900$ kg/m^3	Gravitational tensor
Bouguer 2	$d_{c_{min}} = 7$ km, $d_{c_{max}} = 100$ km, $\rho_c = 2900$ kg/m^3	Gravitational vector
Bouguer 3	$d_{c_{min}} = 7$ km, $d_{c_{max}} = 100$ km, $\rho_c = 2900$ kg/m^3	Gravitational potential
Wieczorek (2015) 1	$\rho_c = 2900$	Gravitational tensor
Wieczorek (2015) 2	$\rho_c = 2900$	Gravitational vector
Wieczorek (2015) 3	$\rho_c = 2900$	Gravitational potential

Table 3.4: Models used to assess the effect of fitting the models to the gravitational tensor, vector or potential.

3.2. GRAVITATIONAL POTENTIAL THEORY

In order to calculate gravitational potential stresses, the method from Pascal (2006) can be used. The biggest difference between Pascal (2006) and this research, is that they use the theory for an intraplate application on Earth and that in this research it is applied on Mars. In this section the equations to calculate the GPE and GPSt are given, together with a short explanation on how they are solved. The equations used are as follows:

$$\sigma_{zz} = g_0 \int_h^z \rho_L(l)\,dl \tag{3.14}$$

$$\sigma^R_{zz}(z) = g_0 \int_{h^R}^z \rho^R(l)\,dl \tag{3.15}$$

$$\Delta GPE = \int_h^{z_{bl}} (\sigma_{zz}(z) - \sigma^R_{zz}(z))\,dz \tag{3.16}$$

$$GPSt = \sigma_{xx} = \frac{\Delta GPE}{h - z_{bl}} \tag{3.17}$$

In these equations, σ_{zz} is the vertical stress, g_0 is the surface gravity ($g_0 = 3.711\ m/s^2$), the equations are integrated towards l, which is a signature of altitude or depth, h is the altitude, z is the depth and ρ_L is the density of the martian interior, which is variable with depth and location as specified by the interior density models. The suffix R is a signature of a reference column, ΔGPE is the change in gravitational potential energy, σ_{xx} is the horizontal stress, from now on called GPSt and as last, z_{bl} is the baseline depth, this is equal to the depth up to which the GPSt is calculated.

The value for the compensation depth is different for each interior density model. Important to note is that this will not lead to large differences in the results for different models as the results say something about the relative difference between the GPE in the reference column and the column calculated. However, as mentioned before, for performing a seismic analysis, only the upper 30 to 80 km of the lithosphere are needed,

therefore z_{bl} is taken as several values in between. For each value, the results will be calculated, leading to one of the research questions mentioned in Section 1.4: **What is the effect of changing the brittle-ductile transition depth?** In this research, the baseline depth and BDT depth always have the same value.

The only question left for the gravitational potential analysis is what the reference column should be. A reference column is used to compare the actual lithospheric density columns with. This column is in a state of equilibrium, or said otherwise, it is an average column of the planet. The choice of the reference column affects the results, as shown in equation 3.16. A state of equilibrium can be found when the topography is zero, therefore an existing column with zero topography is always chosen as a reference column. One other factor to keep in mind is the density of the reference column. When fitting the interior density models to the gravitational potential, the density in this column changes as well, and it might be possible that this is then not an *average* column anymore. Therefore, the crustal and mantle density of this column is changed to the average crustal and mantle density of the entire model. In Figure 3.8, the reference column is shown on the right side and several actual lithospheric columns are shown on the left side. Each column has a different density profile which is obtained using the interior density models, as explained in the previous section. The reference column always has the crustal thickness as calculated in the interior density models in places where the topography is zero, and the average crustal and mantle density of the model.

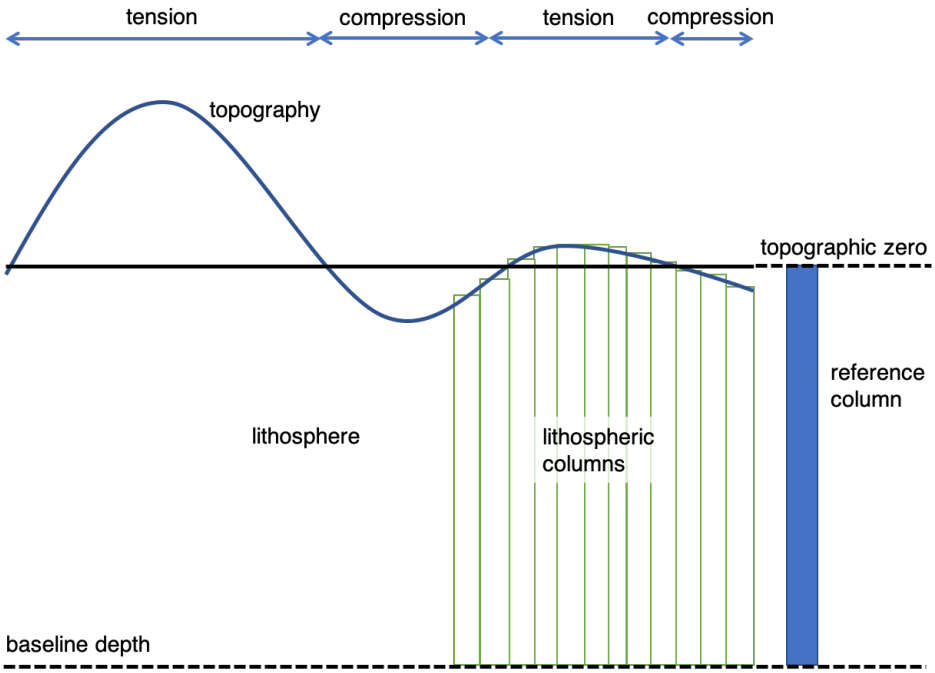

Figure 3.8: Schematic drawing of the GPSt calculations. The blue column is the reference column, which is chosen to be a column with zero topography. The green columns represent lithospheric columns as represented by the interior density models. All columns are used in the calculations up to the baseline depth. Compressional stresses are expected for topographic lows and tensional stresses for topographic highs.

Using the topographic map of Mars, several spots where the topography is equal to zero can be found on the 1 degree grid. Their coordinates and their location names are given in Table 3.5.
What is expected from this method are positive stresses (tension) in regions where the topography is positive and negative stresses (compression) in regions where the topography is negative. A simple comparison for this is a sand castle and sand pit: a sand castle experiences tensional stresses and will eventually collapse to the sides, a sand pit experiences compressional stresses and will eventually collapse to the inside. In Figure 3.8 a schematic of the expected stresses can be seen.

3.3. Seismic analysis

In this section it is discussed how high the stresses in the lithosphere can be before failure occurs and a marsquake will originate, ie. what the yield stress is of the lithosphere. Before starting this section, a small

	lon	lat	location
#1	-13	88	Amazonis Planitia
#2	-32	27	Chryse Planitia
#3	1	45	Cydonia Mensae
#4	74	-31	Hellas Planitia
#5	111	4	Isidis Planitia
#6	161	20	Elysium

Table 3.5: List of the coordinates and locations of reference columns.

summary of all different kinds of stresses is given, as it is important for the calculations to use the correct stresses at all times. First, the most important stresses and states with their meaning are summarized. When talking about stresses in this report, a 3D structure is always considered; ie. stresses in x-, y- and z-direction. If the surface is oriented such that the shear stresses vanish, the normal stresses left are called the principal stresses (this is related to Mohr circle). Deviatoric stresses are the principal stresses minus the mean stress of the principal stresses in x-, y- and z-direction. The difference between each principal stress can clearly be seen when examining deviatoric stresses. The differential stress is the difference between the largest and smallest stress on a point; the largest and smallest stress are always oriented perpendicular of each other. The yield stress is the maximum stress before failure occurs, this is the stress that needs to be calculated and compared with the gravitational potential stresses.

In order to know when the yield stress will be reached, the yield stress envelope can be used. An example of a yield stress envelope is shown in Figure 3.9. On the x-axis the difference between the maximum and minimum principal stress is shown. On the y-axis, the depth of the lithosphere is shown. As mentioned before, this plot is created by the use of two laws: Byerlee's law and the flow law. Byerlee's law indicates from where on brittle failure will occur and the flow law indicates the limit for ductile failure to happen. At a certain depth, the temperature is high enough for there to be no more brittle failure but ductile failure. At this point the highest stresses in the lithosphere can be found. This is called the brittle-ductile transition (BDT) layer. As an Earthquake occurs only due to brittle failure in the lithosphere (thus above the brittle-ductile transition), in this research the focus will only be on Byerlee's law and the BDT depth.

Byerlee (1978) performed research towards the kind of failure which leads to an earthquake. At small stresses, the yield stress depends on the friction coefficient, which is a variable dependent on the type of rock. Byerlee (1978) discovered that at high stresses (stresses which can be found in the Earth's lithosphere) the yield stress does not depend on the rock type but only on the pressure applied. This provides an explanation as to why faults on the Earth and other planets originate in depth and length over long distances independent of the stratification of the ground. In Figure 3.10 it can be seen how Byerlee himself plotted the shear stress, τ, against the normal stress, σ_N, when failure occurs for multiple types of rocks. In this case, σ_N is the stress perpendicular to the surface and τ is the stress parallel to the surface. He plotted each combination of σ_N and τ and saw a linear relation between the two. The relations he found are stated below (Byerlee, 1978):

$$\begin{cases} \tau = 0.85\sigma_n & \text{if } \sigma_n \leq 200\text{MPa} \\ \tau = 50\text{MPa} + 0.6\sigma_n & \text{if } \sigma_n > 200\text{MPa} \end{cases} \tag{3.18}$$

In literature, several different versions for Byerlee's law can be found, each using different constants (Azuma and Katayama, 2017; Burg, 2017; Burov, 2011; Stein et al., 2003; Watts and Moore, 2017). It is unclear why that is, most likely it is because different authors performed the analysis Byerlee performed themselves and came up with slightly different numbers for Equation 3.18. In this research the equations given by Byerlee himself, as given in Equation 3.10, will be used. This will not affect the final conclusions as the differences between Byerlee's law from varying authors are small and can thus be neglected.

Using Equation 3.19 and 3.20, Equation 3.18 can be translated to the principal stresses.

$$\sigma_n = \frac{1}{2}(\sigma_1 + \sigma_3) + \frac{1}{2}(\sigma_1 - \sigma_3)cos(2\theta) \tag{3.19}$$

$$\tau = \frac{1}{2}(\sigma_1 - \sigma_3)sin(2\theta) \tag{3.20}$$

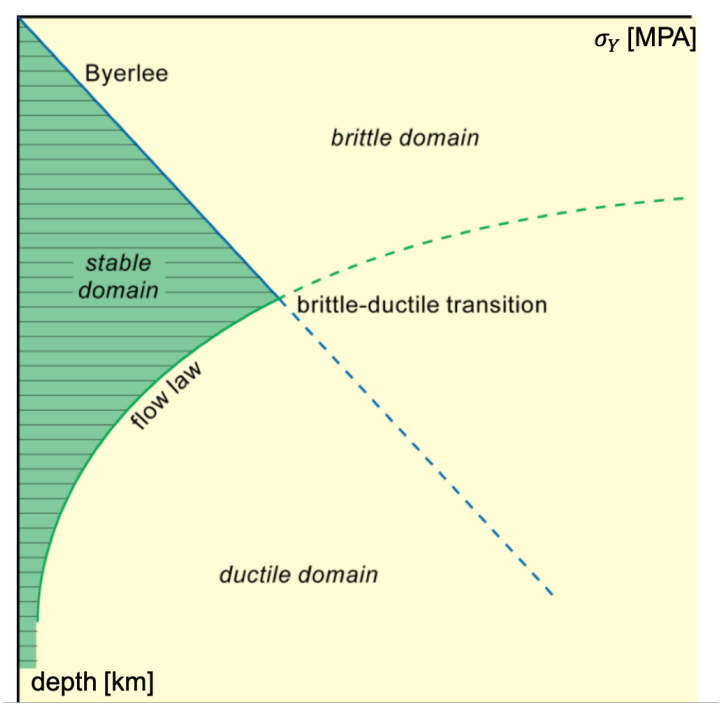

Figure 3.9: General overview of a yield stress envelope (Burg, 2017). The yield stress with respect to the lithospheric depth is shown. This plot consists out of two relations: Byerlee's law indicating the yield stress for brittle failure and the flow law indicating the yield stress for ductile failure. At their intersection, the maximum yield stress of the lithosphere can be found.

Here, θ refers to the angle between the normal stress and the direction of σ_1, σ_1 and σ_3 are the maximum and minimum principal stress respectively. For failure in rocks, θ is usually equal to $\pm$ 60 degrees (Burov, 2011). Performing the transfer to the principal stresses results in the following equations (Burov, 2011):

$$\begin{cases} \sigma_1 = 4.7\sigma_3 & \text{if } \sigma_3 \leq 114\text{MPa} \\ \sigma_1 = 3.1\sigma_3 + 177\text{MPa} & \text{if } \sigma_3 > 114\text{MPa} \end{cases} \tag{3.21}$$

The yield stress, σ_Y, is calculated in terms of the maximum difference between principal stresses. In the lithosphere these principal stresses are assumed to be horizontal and vertical, so the difference between maximum and minimum is calculated as follows: $\sigma_H - \sigma_V$. Small deviations from the vertical and horizontal can be possible, however in this research this is neglected as they would not result in significant anomalies in the results. Due to the weight of the rock above, the stresses in the lithosphere are all compressive. Therefore defining the maximum and minimum stress is all about which stress is the least compressive. There are two options: (1) the vertical stress (σ_V) is the most compressive which results in tension and (2) the vertical stress (σ_V) is the least compressive, resulting in compression.

In case of *tension*, the Byerlee equations are defined as follows:

- For low stresses ($\sigma_3 \leq 114$MPa):

$$\begin{cases} \sigma_V = \sigma_1, & \sigma_1 = -\rho g z \\ \sigma_H = \sigma_3, & \sigma_3 = \frac{\sigma_1}{5} = -\frac{\rho g z}{5} \end{cases} \tag{3.22}$$

- For high stresses ($\sigma_3 > 114$MPa):

$$\begin{cases} \sigma_V = \sigma_1, & \sigma_1 = -\rho g z \\ \sigma_H = \sigma_3, & \sigma_3 = \frac{\sigma_1 + 175\text{MPa}}{3.1} \end{cases} \tag{3.23}$$

In case of *compression*, the Byerlee equations are defined as follows:

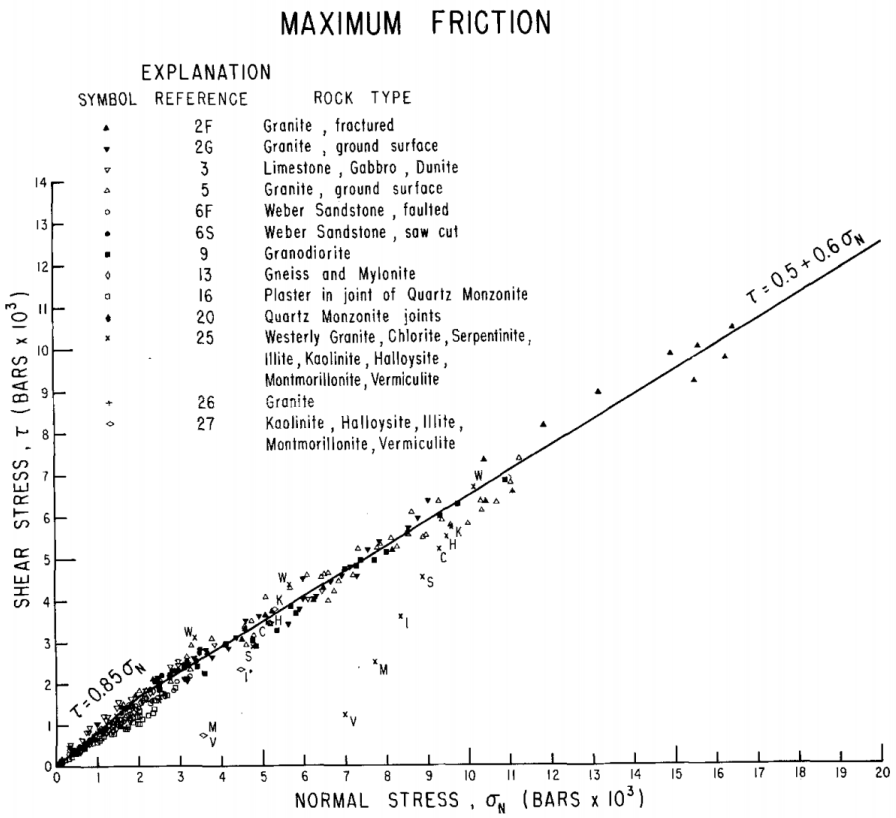

Figure 3.10: Experimental results of the normal and shear stress of multiple materials at yield conditions (Byerlee, 1978). This is the original plot Byerlee created when he came up with his law. A linear relation between the normal and shear stress can be seen when brittle failure occurs. 1 Bar is equal to 0.1 MPa.

- For low stresses ($\sigma_3 \leq 114$MPa):

$$\begin{cases} \sigma_V = \sigma_3 & \sigma_3 = -\rho g z \\ \sigma_H = \sigma_1 & \sigma_1 = 5\sigma_3 \end{cases} \tag{3.24}$$

- For high stresses ($\sigma_3 > 114$MPa):

$$\begin{cases} \sigma_V = \sigma_3 & \sigma_3 = -\rho g z \\ \sigma_H = \sigma_1 & \sigma_1 = 3.1\sigma_3 + 175\text{MPa} \end{cases} \tag{3.25}$$

Note that for all equation z is defined positive downwards.

In the compressional case, $\sigma_H - \sigma_V$ is equal to a negative number, while in the tensional case this is equal to a positive number. This agrees with the usual convention for stresses. Solving these equations, it becomes clear that the crust is able to support higher compressional stresses compared to tensional stresses. For both tensional and compressional stresses, the yield stress increases with depth due to an increasing normal stress.

In case the medium is not dry, but there is some liquid inside, the material is weakened. This can also be taken into account in Byerlee's law by using the pore pressure (Burov, 2011). The pore pressure needs to be subtracted from both σ_H and σ_V, this can be done easiest as follows:

$$\sigma_Y = (\sigma_H - \sigma_V)(1 - \lambda) \tag{3.26}$$

Where λ is the fluid pressure factor which represents the ratio between the amount of liquid pressure present and the amount of rock pressure present (confining pressure). In case of a dry medium, λ is equal to zero. A value of 0.7 for λ points to a wet medium and a value of 0.37 points to a hydrostatic equilibrium (Byerlee, 1978). On Mars, there have been suggestions of there being liquid water present in the crust (Mueller and

Golombek, 2004). Therefore, it is important to take this into account when solving the equations. This parameter is made a variable throughout the entire research and can be seen in the following research question (see 1.4): **What is the effect of a dry or wet lithosphere on the failure criteria?**

Another important question left, is up to what depth marsquakes occur. On Earth, intraplate earthquakes are usually above 40 km (Burov, 2011). At subduction zones these can be deeper, but there are no subduction zones on Mars. According to Burov (2011) there are two reasons why there will be no deeper earthquakes: (1) a stress drop is present at the Moho due to the mechanic decoupling of the crust and mantle and (2) the failure mode for quakes is brittle and not ductile, whereas the conditions below the Moho lead to ductile behaviour. The question now is, whether on Mars the same behaviour can be expected and what the maximum marsquake depth is. As mentioned in Chapter 1.3, Plesa et al. (2018) and Azuma and Katayama (2017) performed research towards the brittle-ductile transition depth on Mars. The BDT depths found by both of them are significantly deeper compared to the Earth. The variable depth for the BDT is taken into account in this research by the following research question: **What is the effect of changing the brittle-ductile transition depth?** The seismic analysis will be performed for a BDT depth of 30, 65 and 80 km in a wet, dry and hydrostatic regime. The dryer ($\lambda \approx 0$) and stronger regime being the more likely to be close to reality according to Azuma and Katayama (2017).

The last factor left to solve this problem is how to compare all data with each other. For this, the ratio between the intersection depth of the YSE and the stress in the respective column to the baseline depth is used. In Figure 3.11 the intersection depth between the YSE and the stress, z_i, is shown together with the baseline depth, z_{bl}. Note that z_{bl} is also equal to the BDT depth. The part of the stress line which is above the YSE can fail and the part of the stress line under the YSE will not fail. Therefore, the ratio between the failing part and non-failing part gives an idea of how likely the entire column is to fail. From now on, this ratio is called the failure ratio or FR. The higher this ratio, the more likely failure is. The ratio is expressed in % in the remainder of this report. For evident comparison purposes, the FR is shown negatively when talking about compressional stresses (negative stresses) and positively when talking about tensional stresses (positive stresses):

$$FR = sign(GPSt)\frac{z_i}{z_{bl}} \tag{3.27}$$

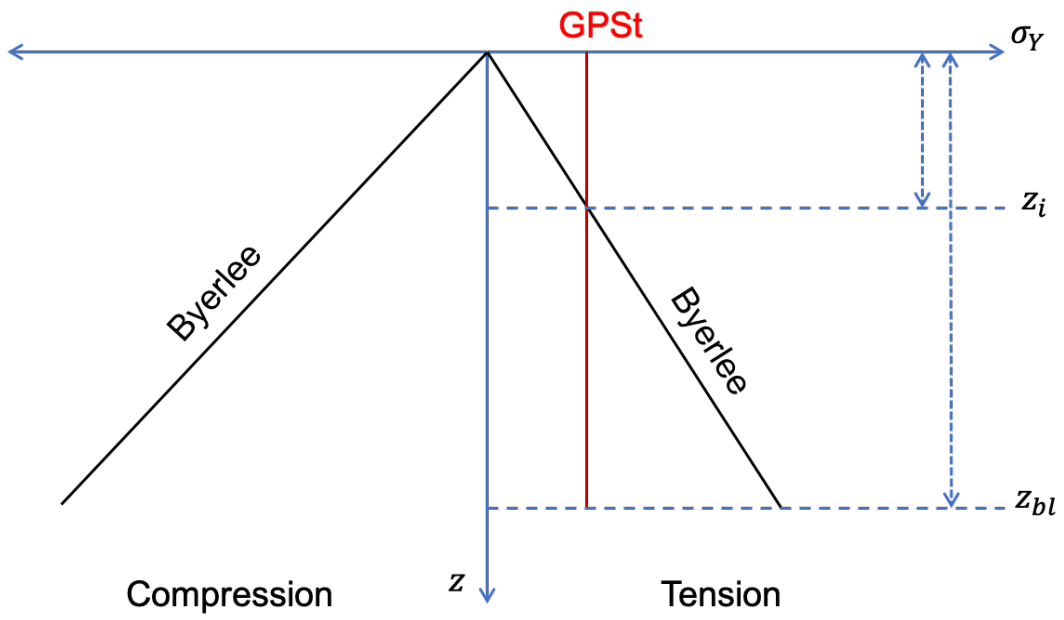

Figure 3.11: Schematic of Byerlee's law overplotted by a positive GPSt. The ratio between the depth at which the yield stress is reached, z_i, and the brittle-ductile transition or baseline depth, z_{bl}, is called the failure ratio or FR.

4. RESULTS

The final results could be produced after the validation and verification of all used programs (as described in Appendix A). This chapter is divided into three main steps: (1) the interior density models, (2) the potential theory and (3) the seismic analysis. After the aforementioned has been discussed, the six research sub-questions which were highlighted in the previous chapter are repeated and answered together with an elaboration on important locations on Mars.

4.1. INTERIOR DENSITY MODELS

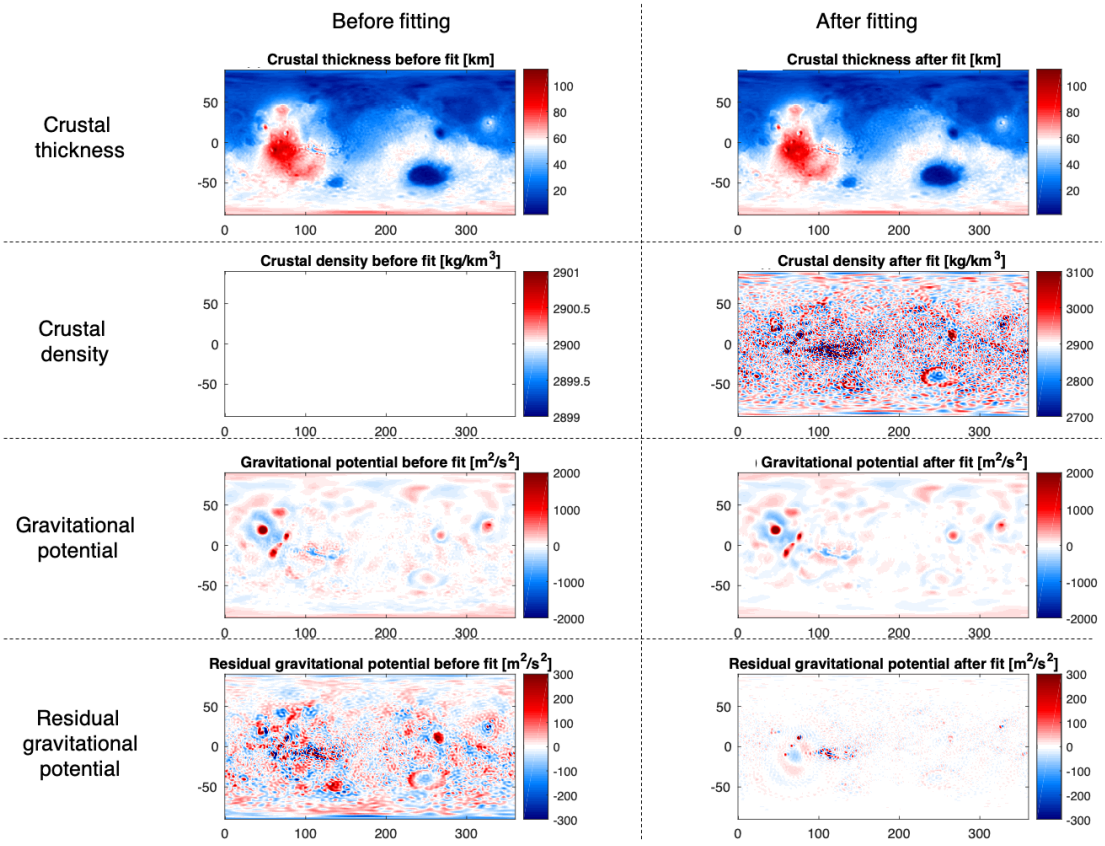

Figure 4.1: Crustal thickness, crustal density, gravitational potential and the gravitational potential residual for a Bouguer model with a crustal depth between 7 and 100 km and a crustal density of 2900 kg/m^3. The results are shown before (left side) and after (right side) fitting the model with the gravitational potential. The crustal thickness stays the same before and after the fit, as it is chosen not to fit the model by changing the crustal thickness. The crustal density is not constant anymore after fitting. The gravitational potential residual is lower over the entire map after the fitting process.

An important step in creating the interior density models is fitting them to the gravitational potential by putting density anomalies in the crust (or mantle). In Figure 4.1 the Bouguer model with a crustal depth between 7 and 100 km and a crustal density of 2900 kg/m^3 is shown. In the left column, the results of simply applying the Bouguer equations are shown. The crustal thickness and crustal density are shown, together with the calculated gravitational potential from this model and its residual with the actual gravitational potential. In the right column, the results after fitting the calculated gravitational potential with the actual gravitational potential by putting density anomalies in the crust are shown. This model was created by minimizing the gravitational potential residual with several iterations. By comparing the left and right column, it can be seen that there is no difference in crustal thickness, as it is chosen to not fit to the gravitational potential by changing the crustal thickness. The crustal density is the variable parameter when fitting to the gravitational

potential, it can be seen that before fitting, the crustal density is constant everywhere and after fitting, there are small changes present. The residuals after the fitting process are significantly smaller than before fitting. A signature for a good fit is that it is not possible to identify topographic features on the residual map. The only features which can still be seen are the Tharsis volcanoes, Valles Marineris, Elysium Mons and Isidis Planitia. This is due to the limits put on the density changes in the crust (maximum -200 or +200 kg/m^3 while fitting), when taking higher limits unrealistic densities would be found. When also using a varying crustal thickness this problem could be tackled, however it is chosen not to focus on this during this research. The locations where the highest crustal density anomalies can be seen are places where this model fits worst. This is at the same locations as where the residuals are still highest after fitting: Tharsis volcanoes, Valles Marineris, Elysium Mons and Isidis Planitia.

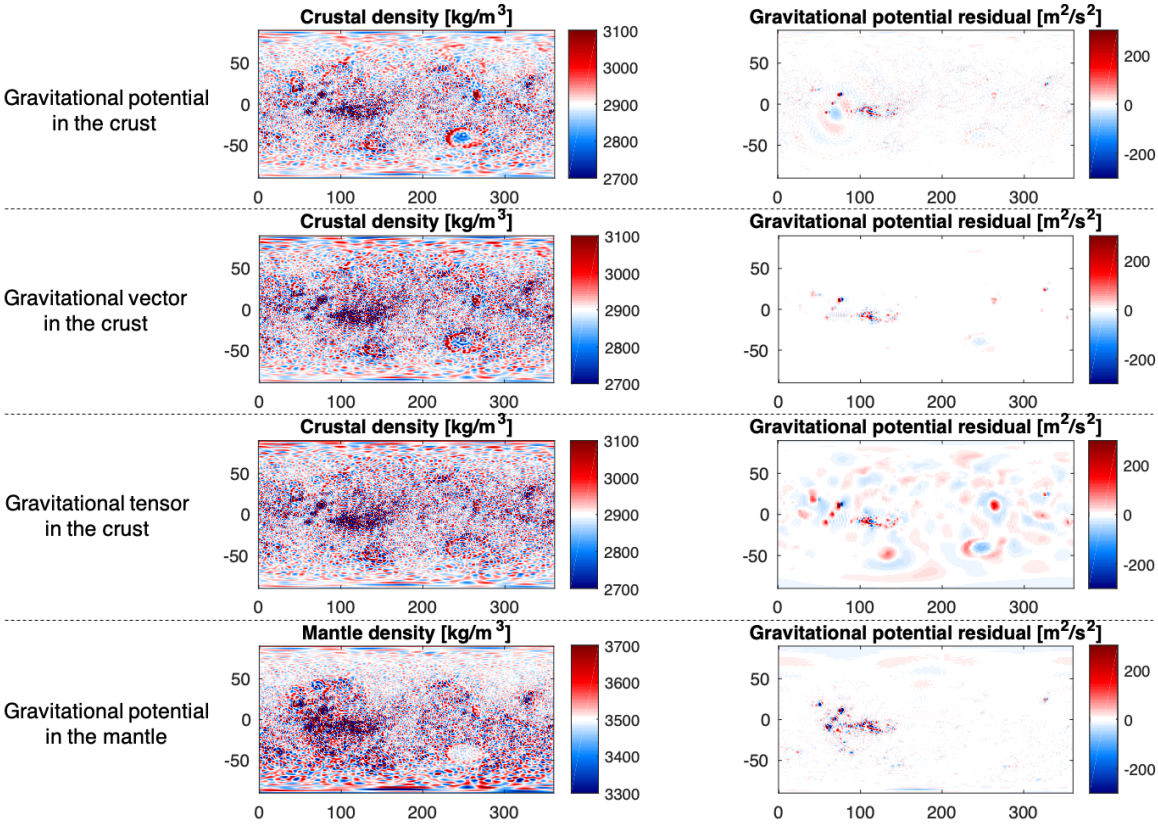

Figure 4.2: Comparison of the crustal density and gravitational potential residual for fitting with the gravitational potential, vector or tensor in the crust or mantle. All results are for the Bouguer model with a crustal depth between 7 and 100 km and an average crustal density of 2900 kg/m^3. The highest residuals after fitting are found when using the gravitational tensor and the crust, the lowest are found when using the gravitational vector in the crust.

In Figure 4.2 the difference of fitting the same Bouguer model with (1) the gravitational potential in the crust, (2) the gravitational tensor in the crust, (3) the gravitational vector in the crust and (4) the gravitational potential in the mantle is shown. For each different type of fitting, the crustal density and residual of the actual and calculated gravitational potential are shown. Also, for each type, a similar amount of iterations is used. In the first column, the crustal density can be seen to differ most from 2500 kg/m^3 for fitting in the crust with the gravitational vector and tensor. While fitting in the mantle, the crustal density is constant as density anomalies due to fitting can be found in the mantle. The residual of fitting with the tensor is the worst, this can be concluded because the highest deviations from zero can be seen. The other three fits are similar to each other in terms of quality. Fitting in the crust is presumed to lead to more interesting results, as crustal density is a direct input parameter for the GPSt and YSE. When using the gravitational potential, less density anomalies are found compared to using the gravitational vector. This is preferred over a slightly better fit which is found when using the gravitational vector. Taking all these factors into account, the default fitting method is chosen to be fitting in the crust by use of the gravitational potential. Use of the gravitational vector would have been

an equally well choice, but only one method is needed.

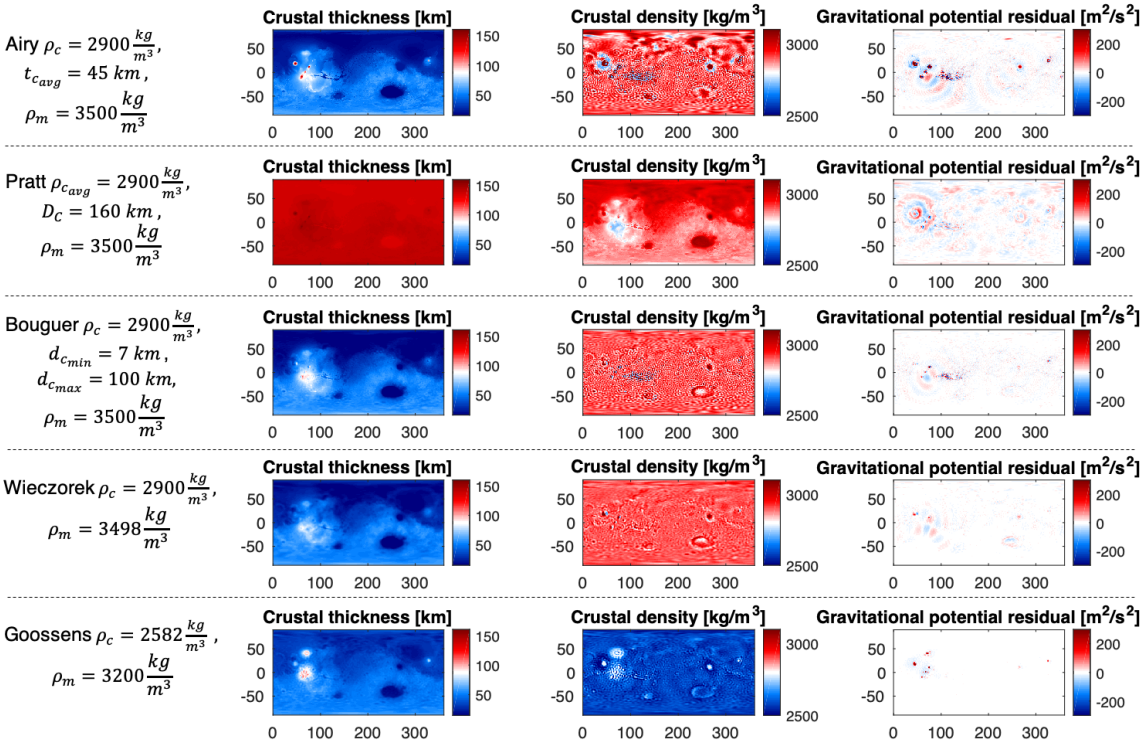

Figure 4.3: Comparison of the interior structure and fit with gravity of five different models, one model of each type. In the left column, the crustal thickness can be seen, in the middle column, the crustal density is shown and on the right side, the residual between the calculated and measured gravitational potential is shown.

In Figure 4.3 a comparison between one model of each type is shown. Similar parameters for each model are chosen as can be seen in the most left column. For each model the crustal thickness, crustal density and the residual between the actual and calculated gravitational potential is shown. Regarding crustal thickness: it can be seen that the Airy, Bouguer and Wieczorek models correlate with the topography, the Goossens model also looks similar but with lower minima in the north. For the Pratt model, the crustal thickness is equal to the compensation depth added together with the topography, therefore the crustal thickness is large at each location with small relative differences. Secondly, the crustal density is shown. Here, the crustal density is not constant in any of the models because fitting with the gravitational potential is done by putting density anomalies in the crust. Therefore, by looking at the deviations of the crustal density (which is given as input parameter), the quality of the original fit can be seen. For example, in the first model, Airy with $\rho_c = 2900$ kg/m^3 and $t_{c_{avg}} = 45$ km, large deviations from the crustal density of 2900 kg/m^3 can be seen, which is a signature of the original model being a relative bad fit with respect to the other models. In the Airy model, also a large difference in density anomalies can be seen between the north and south; in the north, larger density anomalies are needed in order to reach the best fit compared to the south. This is due to the fact that the north is younger of age compared to the south and has as follows not reached a high degree of compensation yet. The Airy model assumes full isostatic compensation, hence resulting in an initial less performing fit in the north compared to the south of the planet. The crustal density for the Pratt model is correlated to the topography of Mars (see Figure 1.1), which is due to the assumptions made when using the Pratt model. In this model it is harder to see the deviations from the actual value as there is no constant density. Therefore, in Figure 4.4 the residual of the density before and after fitting of the Pratt model is shown. Similar as to the Airy model, the anomalies in the north are higher compared to the south, indicating that the north is less isostatically compensated compared to the south. This is also in accordance with the younger surface age of the north compared to the south In the Bouguer and Wieczorek model (both based on the Bouguer gravity) the difference between north and south cannot be seen, as these models do not assume a state of isostatic compensation. In the fitted model by Goossens et al. (2017), large deviations in crustal density can

be seen at the Tharsis region and Alba Patera, this is because in his model a higher density for the volcanoes is used as they are made up out of upcoming lava, which has a higher density than crustal material. In the right column, where the residual between the actual and calculated gravitational potential is shown, it can be seen that most plots are simply green, implying that the fits are mostly good. For most models, the Tharsis volcanoes can clearly be seen, indicating that those are hard to model using the data currently available. This agrees with the fact that it is not known yet how the load of Tharsis is distributed over the lithosphere. The Wieczorek model provides the best fit for the Tharsis region. The Airy and Pratt models have the least performing fits with the gravitational potential. This is because these models initially only use topographic data as input and because both of them assume an isostatic equilibrium. Using the Bouguer gravity, the fit for the Tharsis volcanoes improved, however in this model Valles Marineris cannot be fitted. Important to keep into account is that seismic predictions based on these models are the least accurate at locations where the gravitational potential residual is highest. This is because the modelling of these locations has the highest uncertainty.

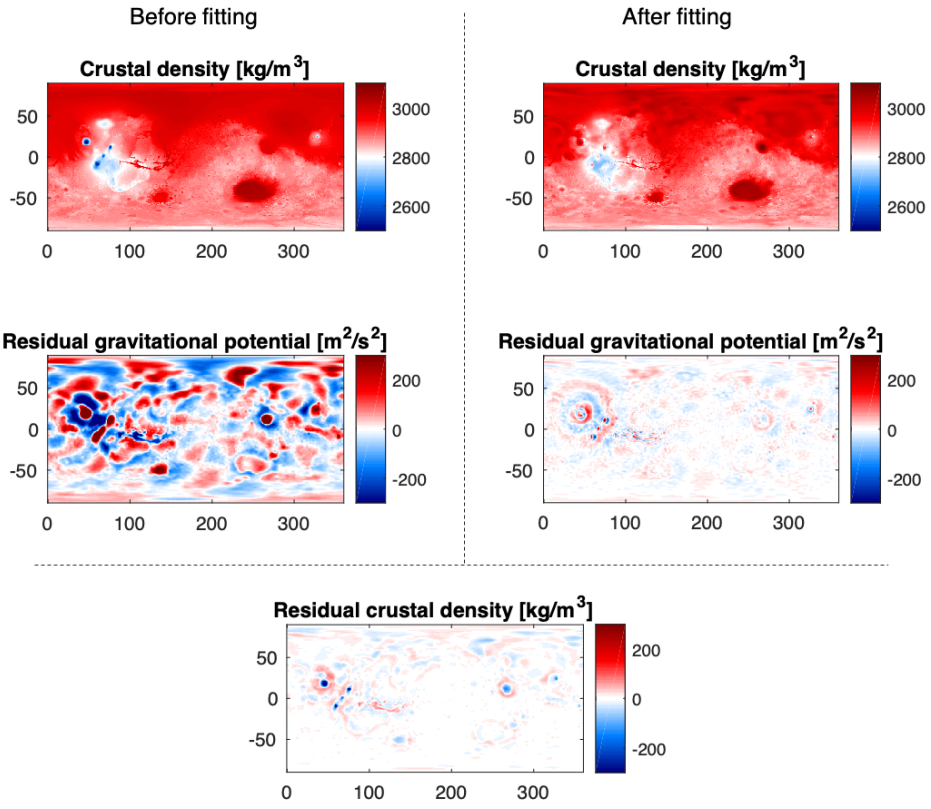

Figure 4.4: The crustal density and residual with the gravitational potential of a Pratt model before and after fitting to the gravitational potential. The Pratt model using a compensation depth of 140 km and average crustal density of 2900 kg/m^3 is shown. In the bottom plot the residual between the crustal density before and after fitting to the gravitational potential can be seen. Higher anomalies can be seen in the north for both the crustal density residual and the fit with gravitational potential before fitting. This leads to the conclusion that the north is less isostatically compensated compared to the south.

In Table 4.1 the quality of all models is shown. This is done by use of the root mean square (RMS) of the residual between the actual and calculated gravitational potential. This value is also used as iteration criteria, when the optimum fit is found this value is minimum, and making more iterations only increases the RMS. Results are shown for fitting to the gravitational potential in the crust and in the mantle. Overall, the best fits are found by fitting to the gravitational potential in the crust. This is because the largest part of each model consists out of crust and not mantle, so there is a larger part of the lithosphere that is adapted with adding density anomalies in the crust. The Pratt models fitted in the mantle show the worst results. This is because the mantle is not modelled in here, as in the Pratt model every column consists out of crust up to the compensation depth. The smallest RMS values are found for the Bouguer model with a low crustal and mantle density and the models by Wieczorek (2015) with a crustal density of 2700 kg/m^3 and 2900 kg/m^3.

Model type	Input parameters	Crust	Mantle
Airy	$\rho_c = 2500\ kg/m^3$, $\rho_m = 3000\ kg/m^3$, $t_{avg} = 45\ km$	23.17	43.57
Airy	$\rho_c = 2500\ kg/m^3$, $\rho_m = 3200\ kg/m^3$, $t_{avg} = 45\ km$	24.17	24.17
Airy	$\rho_c = 2800\ kg/m^3$, $\rho_m = 3300\ kg/m^3$, $t_{avg} = 45\ km$	21.17	62.88
Airy	$\rho_c = 2800\ kg/m^3$, $\rho_m = 3500\ kg/m^3$, $t_{avg} = 45\ km$	34.49	34.49
Airy	$\rho_c = 3100\ kg/m^3$, $\rho_m = 3600\ kg/m^3$, $t_{avg} = 45\ km$	18.42	105.49
Airy	$\rho_c = 3100\ kg/m^3$, $\rho_m = 3800\ kg/m^3$, $t_{avg} = 45\ km$	45.60	45.60
Airy	$\rho_c = 2900\ kg/m^3$, $\rho_m = 3500\ kg/m^3$, $t_{c_{avg}} = 35\ km$	35.51	37.89
Airy	$\rho_c = 2900\ kg/m^3$, $\rho_m = 3500\ kg/m^3$, $t_{c_{avg}} = 45\ km$	30.14	48.05
Airy	$\rho_c = 2900\ kg/m^3$, $\rho_m = 3500\ kg/m^3$, $t_{c_{avg}} = 55\ km$	23.28	40.17
Pratt	$D_c = 110\ km$, $\rho_{c_{avg}} = 2750\ kg/m^3$	15.61	118.03
Pratt	$D_c = 110\ km$, $\rho_{c_{avg}} = 2900\ kg/m^3$	17.03	117.27
Pratt	$D_c = 110\ km$, $\rho_{C_{avg}} = 3050\ kg/m^3$	16.64	116.53
Pratt	$D_c = 100\ km$, $\rho_{c_{avg}} = 2900\ kg/m^3$	14.34	119.62
Pratt	$D_c = 120\ km$, $\rho_{c_{avg}} = 2900\ kg/m^3$	16.10	115.18
Pratt	$D_c = 140\ km$, $\rho_{c_{avg}} = 2900\ kg/m^3$	17.04	111.92
Pratt	$D_c = 160\ km$, $\rho_{c_{avg}} = 2900\ kg/m^3$	20.85	109.57
Bouguer	$\rho_c = 2500\ kg/m^3$, $\rho_m = 3000\ kg/m^3$, $d_{c_{max}} = 7\ km$, $d_{c_{max}} = 100\ km$	**9.53**	17.18
Bouguer	$\rho_c = 2500\ kg/m^3$, $\rho_m = 3200\ kg/m^3$, $d_{c_{max}} = 7\ km$, $d_{c_{max}} = 100\ km$	11.28	17.72
Bouguer	$\rho_c = 2800\ kg/m^3$, $\rho_m = 3300\ kg/m^3$, $d_{c_{max}} = 7\ km$, $d_{c_{max}} = 100\ km$	11.73	19.58
Bouguer	$\rho_c = 2800\ kg/m^3$, $\rho_m = 3500\ kg/m^3$, $d_{c_{max}} = 7\ km$, $d_{c_{max}} = 100\ km$	12.77	18.76
Bouguer	$\rho_c = 3100\ kg/m^3$, $\rho_m = 3600\ kg/m^3$, $d_{c_{max}} = 7\ km$, $d_{c_{max}} = 100\ km$	14.21	21.25
Bouguer	$\rho_c = 3100\ kg/m^3$, $\rho_m = 3800\ kg/m^3$, $d_{c_{max}} = 7\ km$, $d_{c_{max}} = 100\ km$	14.50	19.49
Bouguer	$\rho_c = 2900\ kg/m^3$, $\rho_m = 3500\ kg/m^3$, $d_{c_{min}} = 7\ km$, $d_{c_{max}} = 100\ km$	22.41	43.13
Bouguer	$\rho_c = 2900\ kg/m^3$, $\rho_m = 3500\ kg/m^3$, $d_{c_{min}} = 10\ km$, $d_{c_{max}} = 100\ km$	12.70	19.17
Bouguer	$\rho_c = 2900\ kg/m^3$, $\rho_m = 3500\ kg/m^3$, $d_{c_{min}} = 7\ km$, $d_{c_{max}} = 120\ km$	14.83	19.07
Bouguer	$\rho_c = 2900\ kg/m^3$, $\rho_m = 3500\ kg/m^3$, $d_{c_{min}} = 7\ km$, $d_{c_{max}} = 90\ km$	17.38	17.52
Wieczorek (2015)	$\rho_c = 2700\ kg/m^3$, $t_{c_{avg}} = 29.5\ km$	**9.26**	15.73
Wieczorek (2015)	$\rho_c = 2900\ kg/m^3$, $t_{c_{avg}} = 40.0\ km$	**7.72**	11.37
Wieczorek (2015)	$\rho_c = 3000\ kg/m^3$, $t_{c_{avg}} = 48.8\ km$	12.64	10.64
Wieczorek (2015)	$\rho_c = 3200\ kg/m^3$, $t_{c_{avg}} = 87.1\ km$	347.39	301.37
Wieczorek (2015)	$\rho_{c_{north}} = 3100\ kg/m^3$, $\rho_{c_{south}} = 2900\ kg/m^3$, $t_{c_{avg}} = 46.1\ km$	18.61	25.14
Goossens et al. (2017)	$\rho_c = 2582\ kg/m^3$, $t_{c_{avg}} = 42\ km$	10.51	16.76

Table 4.1: RMS of the graviational potential residual for the models used when fitting with the gravitational potential by placing density anomalies in the crust or mantle. All RMS values are shown in m^2/s^2.

The model by Wieczorek (2015) using a crustal density of 3200 kg/m^3 results in the highest RMS values. This is because this model consists out of 16 layers, due to the correction introduced by Root et al. (2017), that the maximum thickness for each layer cannot be larger than 50 km (see Section 2.2). The other models exist on average out of 6 layers. Therefore, the program has a long running time to find the best fit. This and the fact that the crustal thickness in this model is higher than average (87.1 km compared to 45 km), results in this model being the worst fit. Looking only at the model types, it can be seen that the Wieczorek (2015) and Goossens et al. (2017) models show the best fits, followed by the Bouguer models. The worst fits are found by using the Pratt and Airy models. This is as expected as these models assume an isostatic equilibrium and only use topography as initial input. As conclusion it has to be said that all models have an appropriate fit with the gravitational potential. There are no high RMS values (>150 m^2/s^2), except for the Wieczorek (2015) model with a 3200 kg/m^3 crustal density. Another method for comparison between different models is by looking at density variations; however this is harder as for each model the crustal density variations are 400 kg/m^3, which is the limit imposed on the models during the fitting process (see Section 3.1.4).

4.2. Gravitational potential theory

The main variable of the gravitational potential stresses is the depth up to which it is calculated (referred to as the baseline depth). As mentioned before, the best thing to do is to choose this depth in accordance with

the brittle-ductile transition depth regarding yield stresses. In Figure 4.5, the GPSt for seven specific locations at Mars is shown as a function of the baseline depth. The exact locations can be found in Appendix C. All results shown are for the Airy model with $t_{c_{avg}}$ = 45 km and ρ_c = 2900 kg/m^3. The greatest tensional stresses can be seen at Olympus Mons and the greatest compressional stresses in Valles Marineris. When looking at the course of each line, it can be seen that they exist out of mostly linear lines with a kink in the middle. The kinks are signatures of the crust-mantle boundary or Moho. The Moho for the reference column is at 45 km depth. Depending on its interaction with the Moho of the locations plotted, the kink in the GPSt plot is higher or lower. For example, Tharsis has a deeper Moho, therefore the kink in the line is deeper. The slopes of the lines are a representation of the mass difference between the reference column and the plotted column. A higher mass difference leads to a steeper slope. The line of Elysium Mons intersects with the line of zero GPSt for the reference column. At this intersection, the column is in a state of equilibrium. In the reference column the stresses are zero for all depths as this column is compared with itself.

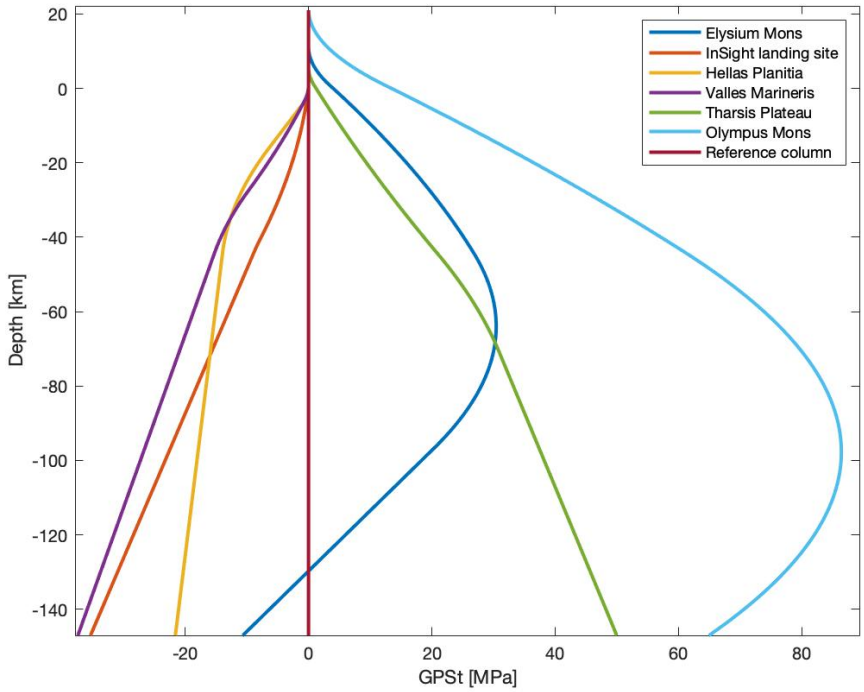

Figure 4.5: GPSt as a function of the baseline depth for seven different locations on Mars using the Airy model with $t_{c_{avg}}$ = 45 km and ρ_c = 2900 kg/m^3. The kinks in the lines are signatures of the Moho of the governing column and the reference column. The GPSt of the reference column is zero at all depths as this column is compared with itself.

In Figure 4.6, the gravitational potential stress maps for five models (one of each type) are shown for three different baseline depths: 30 km depth, 65 km depth and at the maximum depth for each model, ie. the depth up to which each model's density profile is calculated. For the Airy, Bouguer, Wieczorek (2015) and Goossens et al. (2017) models, this depth is equal to the maximum crustal thickness of the model. For the Pratt model, this depth is equal to the compensation depth. Note that for each model the crust mantle density contrast is similar and equal to 600 kg/m^3, except for the Goossens et al. (2017) model where it is equal to 618 kg/m^3. In the first column of Figure 4.6, with GPSt calculated for the first 30 kilometers, it can be seen that the GPSt is largely dependent on the topography. Compression can be seen in topographic lows and tension at topographic highs. This is as none of the models has reached a significant depth up to which some kind of compensation is present. The main stress indicator is simply the weight of the mass above, which is at 30 km depth mainly the topography. This already leads to the conclusion that seismic predictions will not differ between different models when looking only at the first 30 km, unless there are significant lateral density variations between different models.

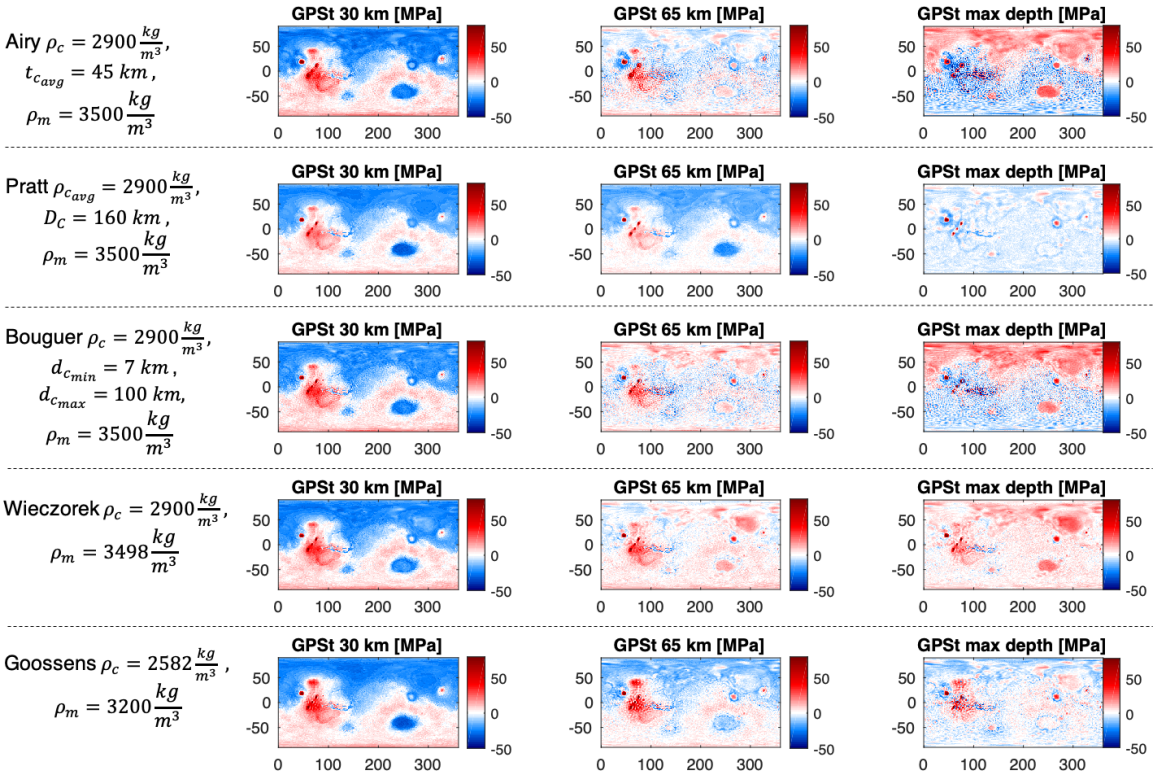

Figure 4.6: Comparison of GPSt for three different baseline depths of five different models. The baseline depths used are 30 km, 65 km and the maximum depth of each model. The maximum depths are 147, 140, 100, 81 and 106 km for the Airy, Pratt, Bouguer, Wieczorek (2015) and Goossens et al. (2017) model respectively.

In the second column of Figure 4.6, where GPSt is calculated up to 65 km, there are already other signatures present aside from topography. In the Airy, Bouguer and Wieczorek model the crustal dichotomy is not clearly present anymore, which is as expected at this depth. At 65 km depth, the overall crustal thickness for both the north and south has already been reached, which means that a regular column in the north and south have the same mass when looking up to 65 km. This results in GPSt maps at 65 km depth where the crustal dichotomy cannot be seen anymore. In the Pratt model the dichotomy can be seen, as the density (which appears in the GPSt equation) differs linearly with the topography. For the Pratt model it is expected that the deeper the GPSt baseline depth, the lower the absolute values of the GPSt become. Goossens et al. (2017) has a higher crustal thicknesses in the north compared to Airy, Bouguer and Wieczorek (2015), which results in lower masses compared to the reference column. This leads to higher compressional stresses in the north compared to the other models. The equilibrium between the north and south has as follows not been reached yet for this model. This is why the crustal dichotomy can still be seen at 65 km depth for the Goossens et al. (2017) model and not for the other models.

When looking at the most right column of Figure 4.6, where GPSt is calculated up to the maximum depth of each type of model even more divert results can be seen. The maximum depths are 147, 140, 100, 81 and 106 km for the Airy, Pratt, Bouguer, Wieczorek (2015) and Goossens et al. (2017) model respectively. For all models, except Airy, the absolute value of the GPSt becomes lower when using a deeper baseline depth. This is because the difference in mass between the reference column and calculated columns becomes smaller when going deeper, as a higher state of compensation is reached. However, in the Airy model, high compressional stresses can be seen in the southern hemisphere. Note that for the Airy model with a baseline depth of 30 km, the compressional stresses are found in the northern hemisphere. When using a deeper baseline depth (147 km in this case), the columns with high topography actually become lighter compared to the places with high topography. This has one main reason which is the high maximum depth (which is equal to the highest crustal thickness of the model). This leads to the conclusion that the Airy model in this case does not reach compensation at its maximum crustal thickness depth. For the Pratt model, the stress is equal to each other

almost everywhere, this is as it should be as the mass in each column should be the same at the compensation depth. The deviations are due to the fitting of the model with the gravitational potential. The locations where the GPSt is not equal to zero (or almost zero), are spots where the Pratt model matches worst with the gravitational potential before being fitted to the gravitational potential. For the Bouguer model, the crustal dichotomy can again slightly be seen, contrary to with a more shallow baseline depth (65 km). The south shows more compressional stresses and the north more tensional stresses. This is because at this depth the weight from the south is lower compared to the weight from the north. As for the Wieczorek (2015) model, the maximum depth does not differ much from 65 km, those two plots are very similar. The Goossens et al. (2017) model has reached a state of compensation at this point, as the crustal dichotomy is not visible anymore.

4.3. SEISMIC ANALYSIS

In Figure 4.7 the yield stress envelope (YSE) for the Earth and for Mars in different configurations is shown. The cases shown are as follows:

- Earth: $g_e = 9.81$ m/s^2, $\rho_c = 2800$ kg/m^3 and $\lambda = 0$
- Mars: $g_m = 3.711$ m/s^2, $\rho_c = 2900$ kg/m^3 and $\lambda = 0$
- Mars lower density: $g_m = 3.711$ m/s^2, $\rho_c = 2500$ kg/m^3 and $\lambda = 0$
- Mars higher density: $g_m = 3.711$ m/s^2, $\rho_c = 3100$ kg/m^3 and $\lambda = 0$
- Mars wet: $g_m = 3.711$ m/s^2, $\rho_c = 2900$ kg/m^3 and $\lambda = 0.7$
- Mars hydrostatic: $g_m = 3.711$ m/s^2, $\rho_c = 2900$ kg/m^3 and $\lambda = 0.37$

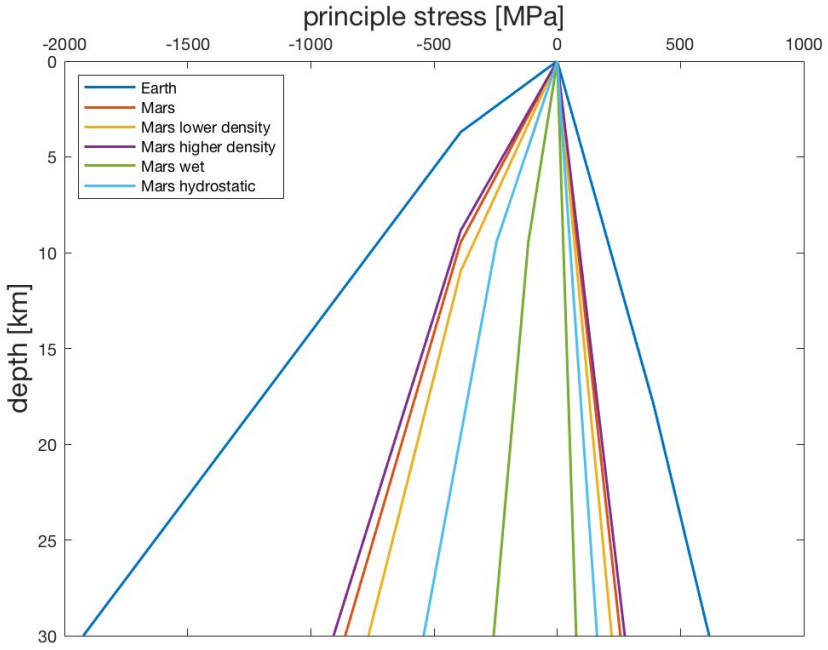

Figure 4.7: Calculated YSE for the Earth and for Mars in different configurations. The Earth is stronger than Mars. Both planets are able to withstand higher compressional stresses compared to tensional stresses. In case the lithosphere contains more fluids and has a lower density, it becomes weaker.

The Earth is stronger than Mars in all cases, as can be seen in Figure 4.7. This is due to the higher gravity on the Earth; gravity is a direct input parameter of Byerlee's law. A planet (in this case Mars) becomes stronger when its density increases and the dryer the lithosphere is. Contrary, it becomes weaker with decreasing density and with a wetter lithosphere. It can also be seen that the yield stress for compression is higher than the

yield stress for tension, which is as expected from literature.

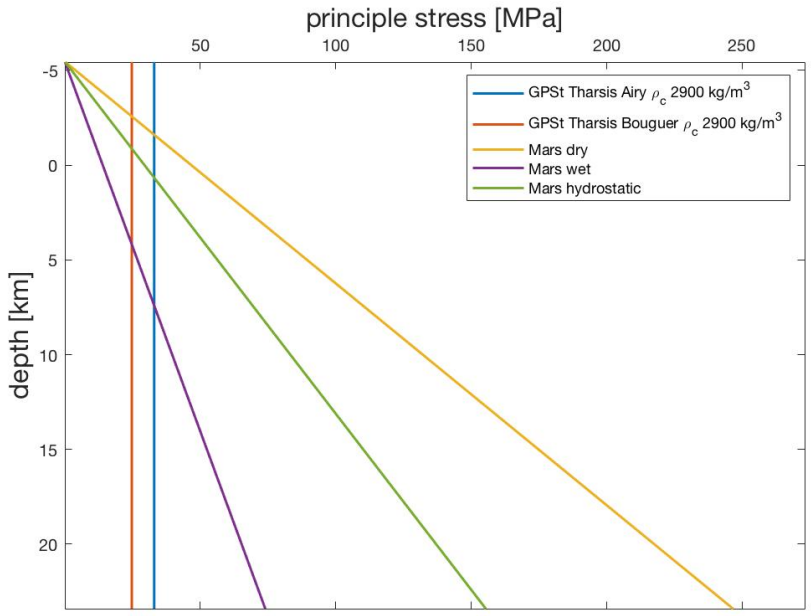

Figure 4.8: YSE of Mars in a dry, wet and hydrostatic state against the GPSt in the Tharsis region for one Airy model (ρ_c = 2900 kg/m^3 and $t_{c_{avg}}$ = 45 km) and one Bouguer model (d_c = [7 km - 100 km], ρ_c = 2900 kg/m^3). This is an example as to how the failure ratio is calculated. The intersection depth of the GPSt and YSE divided by the BDT depth results in the failure ratio.

In Figure 4.8, an example can be seen for the calculated GPSt plotted against the YSE for the Tharsis region of two different models. This plot is only for illustrating purposes, actual results on these values are shown in the remainder of this section and in the next section. Important to note is that the ratio that will be used for comparison purposes (failure ratio or FR) is clearly visible in this figure: the part of the GPSt bar above the intersection with the YSE against the entire depth of the bar. Note that calculation of the YSE starts at the topographic altitude, which is in this case a little bit more than 5 km. In this plot it can be seen that if the actual situation on Mars is more like the Airy case contrary to the Bouguer case at this specific spot, a quake is more likely to happen.

Next, in Figure 4.9, for five models (the same as the five models previously used), a plot of the failure ratio can be seen for dry, wet and hydrostatic conditions on Mars. It can be seen that all figures have low values on the colorbar, indicating that high failure conditions are not found. The highest chances of failure can mostly be seen around Tharsis but also at Elysium Mons. The differences between dry, wet and hydrostatic can clearly be seen: the wetter, the more likely failure is. As discussed before, the GPSts are relatively high when looking at the first 30 km of the lithosphere. This is because the difference between the reference column and the column being calculated for is higher when only a small part of the lithosphere is taken into account as therefore also a small part of the isostatic equilibrium is taken into account. For the same reason, the FR maps are all very similar to the topography of Mars as this is the dominant input parameter and there are small differences between the different types of models. It needs to be noted though that a *high* failure ratio is only relative and all failure ratios are actually small (mostly blue on the plots, close to 0%). This is as predicted, because when all failure ratios would be high (>0.5), the entire planet would collapse.

Comparing the results of Figure 4.10 to those shown in Figure 4.9, where the BDT depth is 65 km, significantly smaller failure ratios can be found, but these failure ratios are less related to the topography. This is because the GPSt maps calculated up to 65 km are also less related to topography, as discussed in the previous section. The FR maps look mostly alike the GPSt maps, with varying ranges of FR depending on whether or not the lithosphere is assumed to be wet, dry or hydrostatic. The highest FRs are present in the Wieczorek (2015) and Goossens et al. (2017) model. In the Wieczorek (2015) model, high FR regions can be seen around Tharsis,

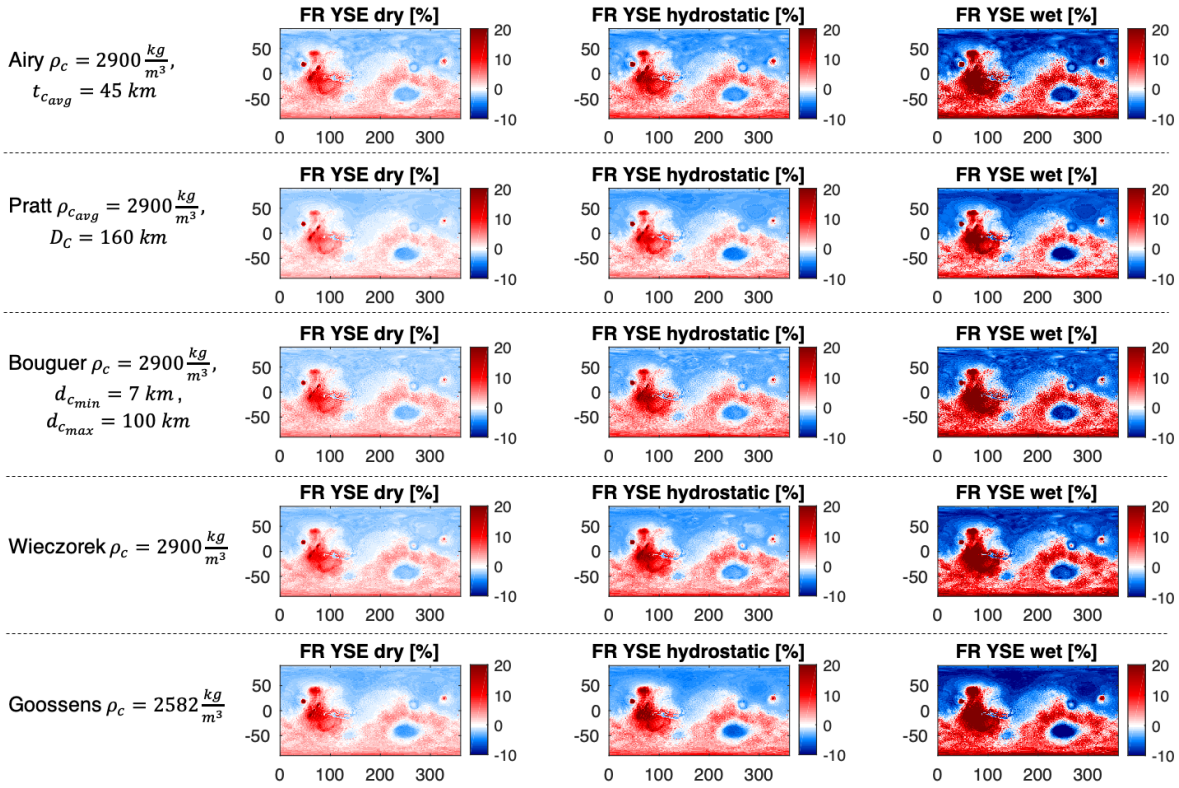

Figure 4.9: Failure ratio maps of five different models for a dry, wet and hydrostatic Mars. The BDT depth is 30 km. The more liquid present in the lithosphere, the higher the FRs become. All models are similar to each other and highly correlate with the topography of Mars. This is because up to 30 km depth, the topography is the main driver when calculating gravitational potential stresses.

Utopia Planita, Isidis Plantia and Hellas Basin. Utopia Planitia is interesting as this zone is not identified as a high FR zone in the other models. Hellas Basin shows diverging results for all models, eg. in the Bouguer and Wieczorek (2015) model it is shown in tension, while in the other models it is shown with very low compressional FRs. Figure 4.3 shows that for the Wieczorek (2015) and Bouguer models, the density inside Hellas Basin is lower than the average density and that the density at the boundary of Hellas Basin is higher than its surroundings. The Airy models show the density variations the other way around (high in the middle and low at the boundaries). This higher density in the middle is why Bouguer and Wieczorek (2015) show Hellas Basin to be in tension, while there are low FRs present for the other models. Interesting to note is that it can clearly be seen that compressive failure ratios (blue) are lower compared to tensional failure ratios, this agrees with the fact that the lithosphere is able to support higher compressional stresses compared to tensional stresses.

4.4. Results research questions

So far, all the results for each main step in the project are shown: (1) the interior density analysis, (2) the calculation of gravitational potential stresses and (3) the seismic analysis by looking at yield stress envelopes. The question now is what does this all mean and what are the differences between models when changing input parameters? Therefore, in this section, all results are combined in order to see clear relations between variable input parameters and outcomes. Each of the six research sub-questions mentioned in Section 1.4 as well as several interesting locations will be reviewed in this section. The default parameters for the models are an average crustal density of 2900 kg/m^3, an average crustal thickness of 45 km, fitted with the gravitational potential by placing density anomalies in the crust, a dry lithosphere and a BDT depth of 65 km. The BDT depth of 65 km is chosen because it is more likely that the BDT depth is closer to 65 km than to 30 km and this shows the most interesting results. When using a BDT depth of 30 km, the results for different models are almost the same and largely dependent on topography, as discussed in the previous section. For each question, one of these parameters will differ. If the value of a certain parameter is not mentioned, the default

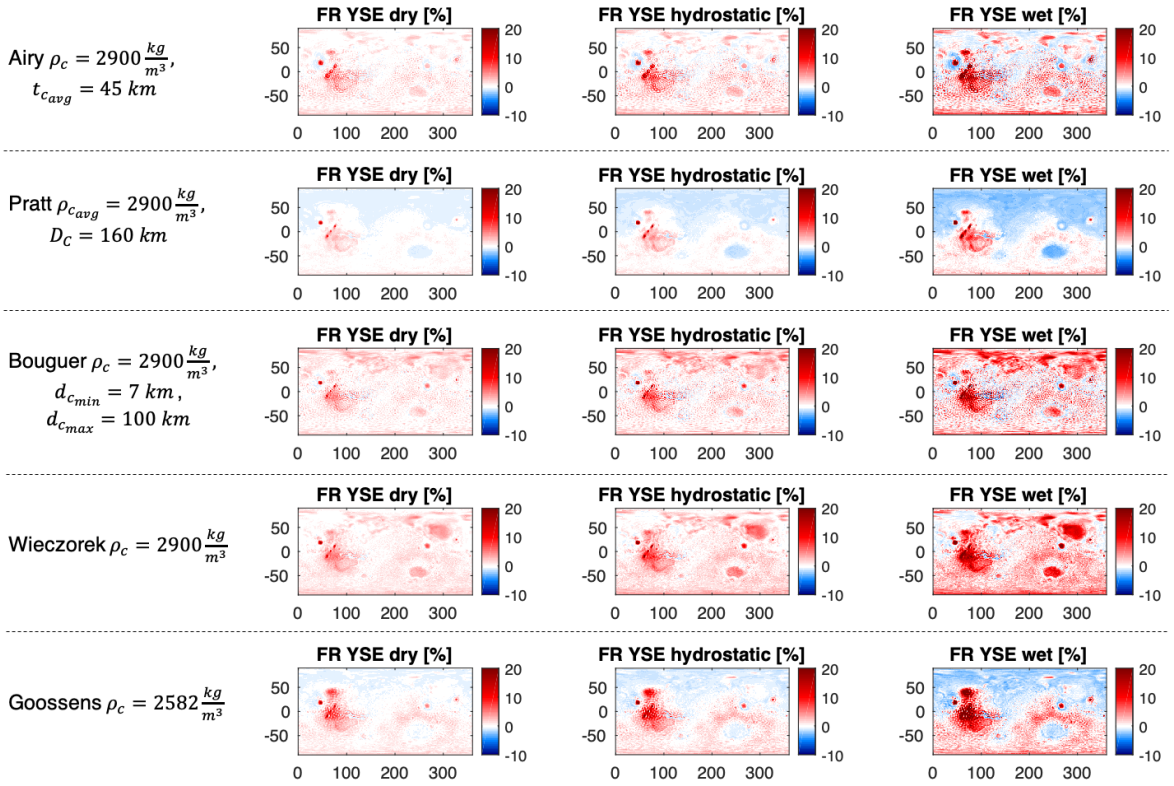

Figure 4.10: Failure ratio maps of five different models for a dry, wet and hydrostatic Mars. The BDT depth is 65 km. The more liquid present in the lithosphere, the higher the FRs become.

value is used. In Figure 4.11, several spots which are used for comparison in other figures in this section are shown on a MOLA topographic map of Mars.[1]

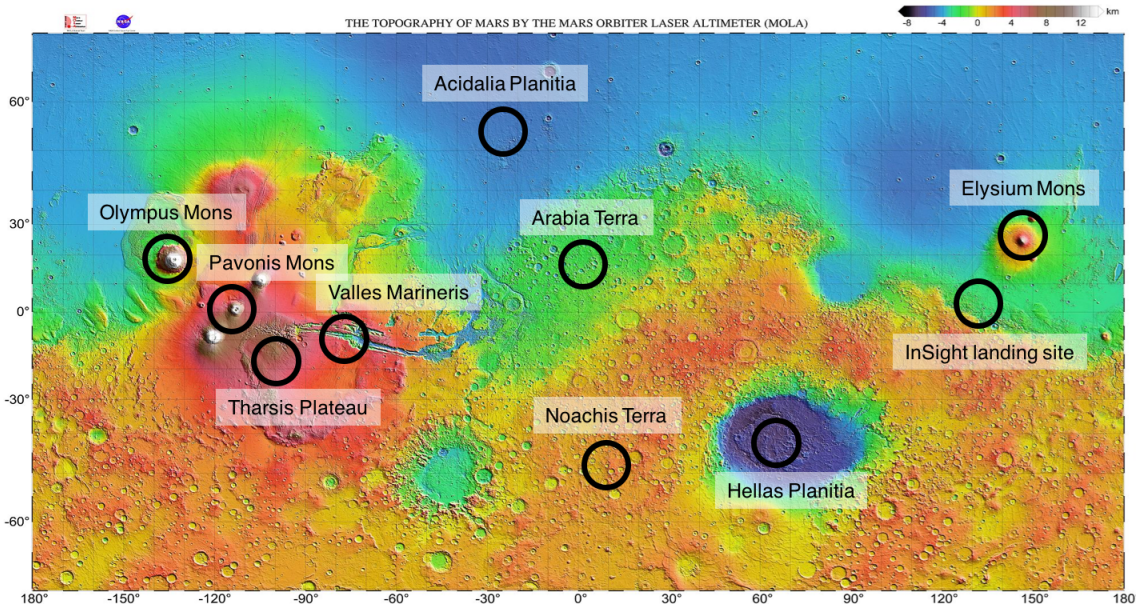

Figure 4.11: Topographic map of Mars (MOLA)[1], locations used for comparison are circled and labeled.

[1] URL `https://attic.gsfc.nasa.gov/mola/images.html` [11-10-2018]

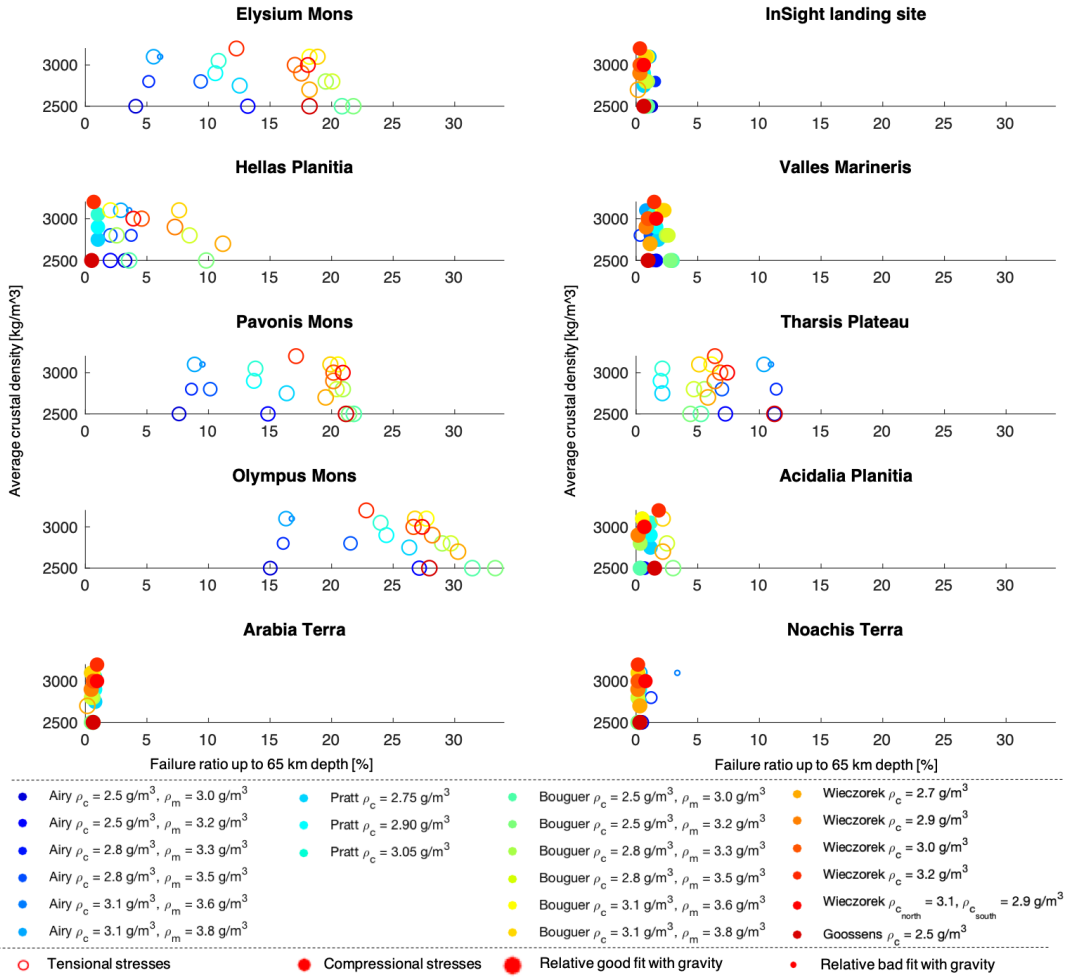

Figure 4.12: Bubble plot showing the effect of changes in average crustal density for a dry lithosphere with a BDT depth of 65 km. No straightforward relation between average crustal density and FR can be seen. When the average FR is higher at a certain spot, the spread of FRs for different models is also higher. This is because there are more modelling uncertainties at these locations.

What is the effect of varying the average crustal and mantle density? In Figure 4.12 a bubble plot that shows the effect of changing the crustal and mantle densities can be seen. Each subplot shows a different location on the planet. The locations are shown in Figure 4.11 and exact coordinates can be found in Appendix C. On the x-axis, the failure ratio is shown and on the y-axis the average crustal thickness. All these models are calculated with the parameters stated in the legend and by fitting with the gravitational potential by putting density anomalies in the crust. The lithosphere is assumed to be dry and a BDT depth of 65 km is used. The size of the bubble is representative for the quality of the fit with the gravitational potential; a larger bubble is a signature for a better fit and a smaller bubble means that the fit is worse. For tensional FRs the bubbles are empty and for compressional FRs the bubbles are filled.

A first item that jumps to mind when looking at Figure 4.12, is that no clear relation between the density and FRs can be seen, for none of the locations. This means that changing the density has no effect on the failure ratio (FR). This can be explained because density appears in the GPSt equation and in the YSE equation (Equation 3.14 to 3.17 and Equation 3.26), and therefore its effect is cancelled out. It can also be seen that the same types of model show similar failure ratios. By looking at the numbers on the x-axis, it can be seen that the larger the FR is, the larger the spread of different FR values is at a certain location. This is at locations of topographic highs, where the fits with gravity are worst in most models. Because there is more uncertainty of the density in columns below these locations, more extreme values are found when comparing different models.

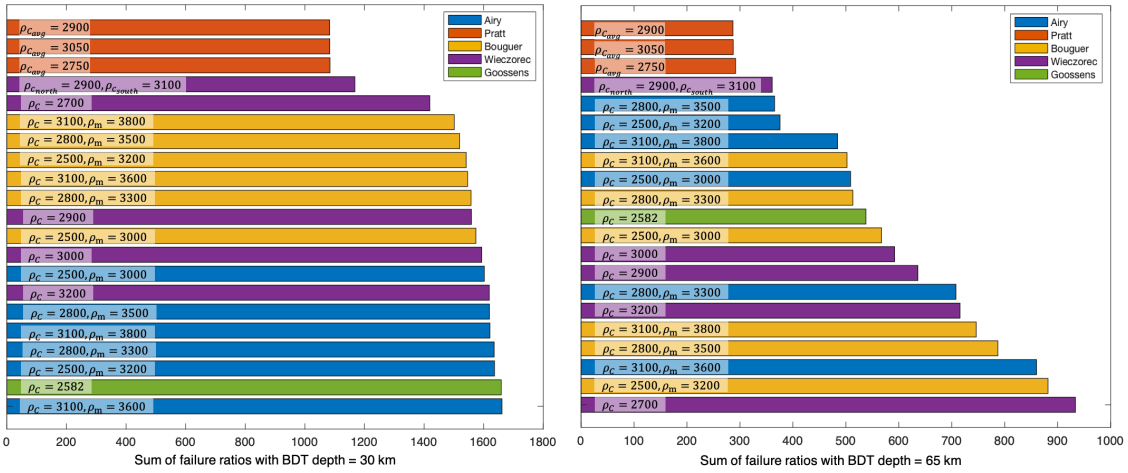

Figure 4.13: Sum of all absolute failure ratios of the models used to test the effect of density on the FRs. On the left side, the results are shown for a BDT depth of 30 km and on the right side for a BDT depth of 65 km. The sum of FRs is higher when the BDT depth is 30 km for each model. Models where isostatic compensation is assumed result in lower FRs.

The statement that density does not have a large effect on the FRs is reinforced by Figure 4.13. Here, the sum of the absolute value of all the failure ratios of the entire map of the same set of models are shown. The sum of all the FRs is representative for the total seismic moment of the planet. On the left side, a BDT depth of 30 km is used and on the right side a BDT depth of 65 km is used. What stands out first is that the results with a smaller BDT depth are significantly higher compared to a deeper BDT depth. This agrees with what was found in the previous sections: that the stresses (and thus FRs) are higher when looking at a more shallow depth because a lower state of compensation has been reached compared to a deeper BDT depth. Using a BDT depth of 30 km, most models have a similar sum of FR, only the Pratt models and Wieczorek (2015) models with a density dichotomy and a crustal density of 2700 kg/m^3 have a lower FR sum. The Pratt models have already reached some kind of compensation, therefore these FRs are low. The Wieczorek (2015) model with a crustal density of 2700 kg/m^3 has a low average crustal thickness, which also means that in this model a larger amount of compensation has been reached at 30 km depth compared to the other models. The Wieczorek (2015) with a crustal dichotomy also applies a Pratt-like theorem, resulting in lower FRs. Looking at the right figure, where the BDT depth is equal to 65 km, it can be seen that the Airy and Pratt models lead to relatively low FRs compared to the other models. Bouguer and Wieczorek (2015) models lead to higher FRs. This is because the Bouguer and Wieczorek (2015) models do not assume isostatic compensation. More explicit, GPSt is equal to zero when a complete state of compensation is reached. For the Pratt and Airy cases, isostatic equilibrium is an assumption when creating the initial models, thus overall a lower sum of FR can be found.

The effect of lateral density variations is also interesting, even though it is not directly related to a research question. In Figure 4.14 the GPSt and FR of the model created by Wieczorek (2015) with a density dichotomy is shown. A BDT depth of 30, 65 and 80 km is used, a dry lithosphere is assumed. The highest stresses and FRs are found when using a shallow BDT depth. With the low BDT depth, the dichotomy can clearly be seen, despite the density dichotomy. Using a BDT depth of 65 km, the dichotomy disappears in both the GPSt map and FR map. It reappears slightly using a BDT of 80 km, indicating that its state of compensation is highest around 65 km depth. High FR regions are Tharsis, Isidis Planitia, Utopia Planitia, Elysium Mons and Hellas Basin. Also the region northwest from Utopia Planitia shows high FRs.

What is the effect of varying the average crustal thickness? In Figure 4.15 the relation between the average crustal thickness and the failure ratio is shown. In this figure, several straight vertical lines can be seen. These straight vertical lines are mostly for the Pratt cases, indicating a complete absence of a relation between the Pratt compensation depth and failure ratio at those locations. Overall, no clear relation between the different FR at different locations can be seen. Therefore, a different plot is used to analyze this relation.

When looking at Figure 4.16 the effect of changing the average crustal thickness on the sum of absolute FRs can be seen. By using this figure it is easier to make a concise conclusion. The Bouguer models show the

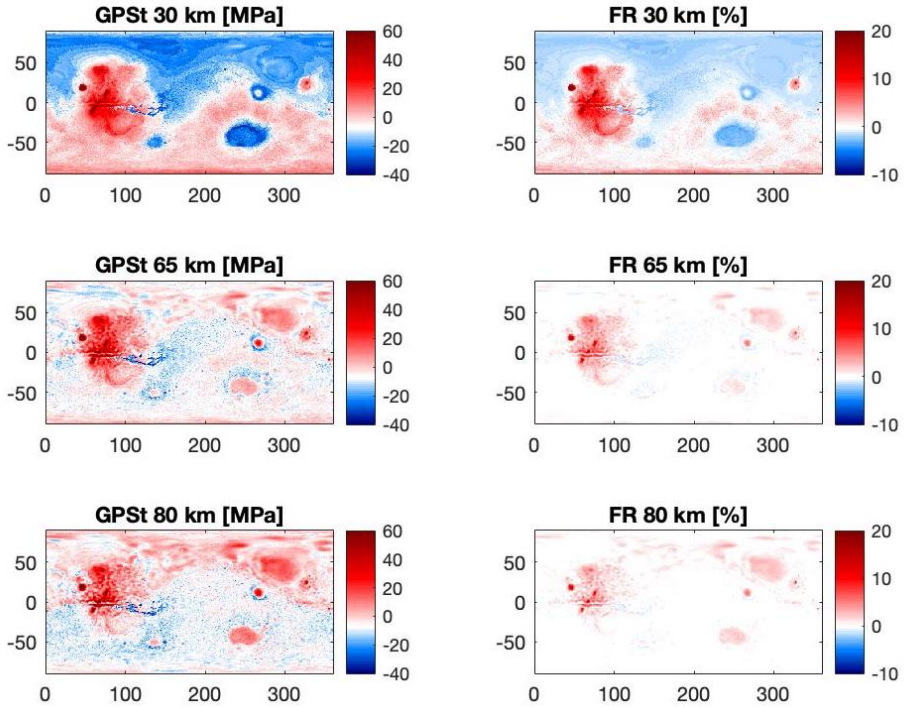

Figure 4.14: The GPSt and FR for the model of Wieczorek (2015) where a density dichotomy is used. The density of the northern hemisphere is 3100 kg/m^3 and the density of the southern hemisphere is 2900 kg/m^3. Results are shown for a BDT depth of 30, 65 and 80 km. The highest stresses and FRs are found using the BDT depth of 30 km.

highest seismicity for both a BDT depth of 30 km and of 65 km. This is again because these models do not assume compensation. The smaller the range for crustal thickness of the Bouguer models, the higher the FR sum. This is because the differences in density for each respective column is higher when the crustal thickness range is smaller. Easier said: there is a lower amount of distance to achieve a similar fit with the measured gravitational potential. For the Pratt models, the FR sum increases with increasing compensation depth. A lower amount of compensation has been reached at the BDT depth (both 30 and 65 km) when the compensation depth is deeper, which results in higher FRs. For the Airy models, the sum of FRs increases with increasing average crustal thickness when the BDT depth is 30 km. This can be explained with the level of compensation reached at this depth. When the average crustal thickness is 35 km, more compensation has been reached at 30 km compared to a higher average crustal thickness. Similar, when the BDT depth is 65 km, the model with a crustal thickness of 45 km is closest to compensation. Concluding, (1) a smaller range of crustal thickness over the entire planet leads to higher failure ratios, as this implies that larger density differences are needed and (2) if the average crustal thickness and BDT depth are further from each other, high FRs are found.

What is the effect of density anomalies resulting from gravitational fitting put in the crust of mantle? In Figure 4.17 the same models which were used in Figure 4.12 are shown, but now for them being fitted by placing density anomalies in the crust ánd in the mantle, in order to see the influence of the modelling choice. The models used are the ones created to test the effect of changing the average density on the failure ratio, a list the models is shown in Table 3.2. The models which are fitted in the crust are shown as circles, the models being fitted in the mantle are represented by diamonds. In Figure 4.18 the same relation is shown but now by using the average crustal thickness models, shown in Table 3.3. At first sight of both figures it already becomes clear that the results are not the same for both modelling options. If all results would be the same, the same colors (pointing towards the same models) would be exactly above each other in the plots. This leads to the conclusion that density anomalies put in the crust or mantle do matter while making seismic predictions. Looking at Figure 4.17, it can be seen that there is no clear relation of whether seismic predictions become higher or lower when changing the fitting choice. This is as predicted, because while fitting to the gravitational potential, there does not arise one unambiguous relation with the density anomalies for

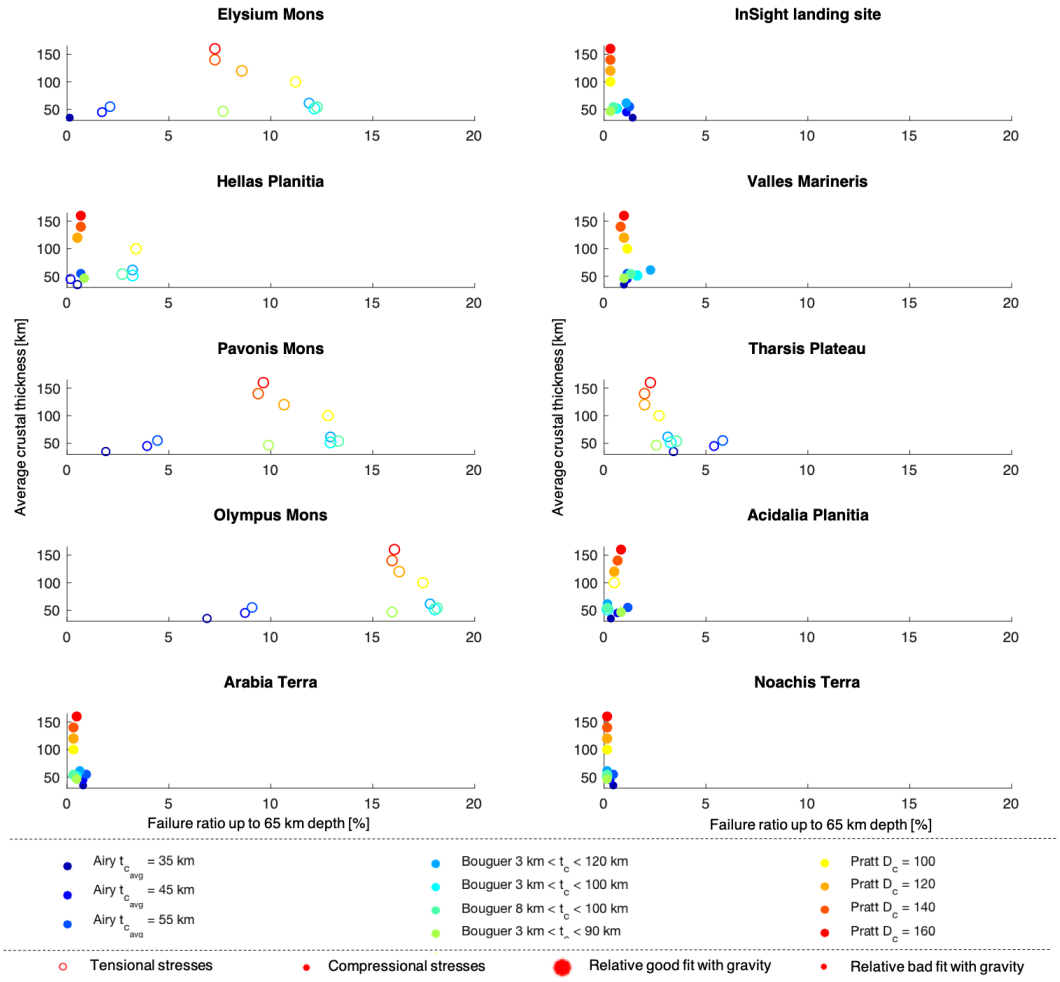

Figure 4.15: Bubble plot showing the effect of changes in average crustal thickness for a dry lithosphere with a BDT depth of 65 km. Each type of models has similar failure ratios.

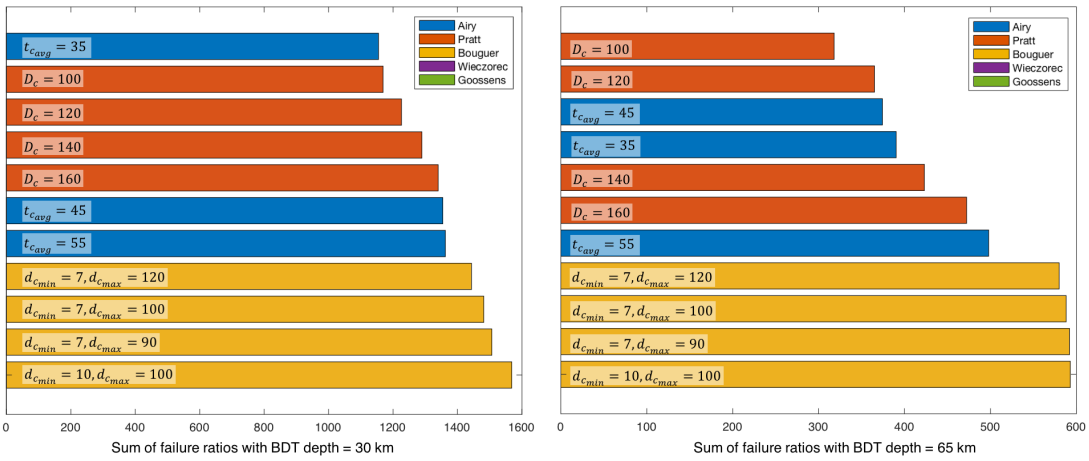

Figure 4.16: Sum of all absolute failure ratios of the models used to test the effect of the average crustal thickness on the FRs. On the left side, the results are shown for a BDT depth of 30 km and on the right side for a BDT depth of 65 km. Models where isostatic compensation is assumed result in a low sum of FRs.

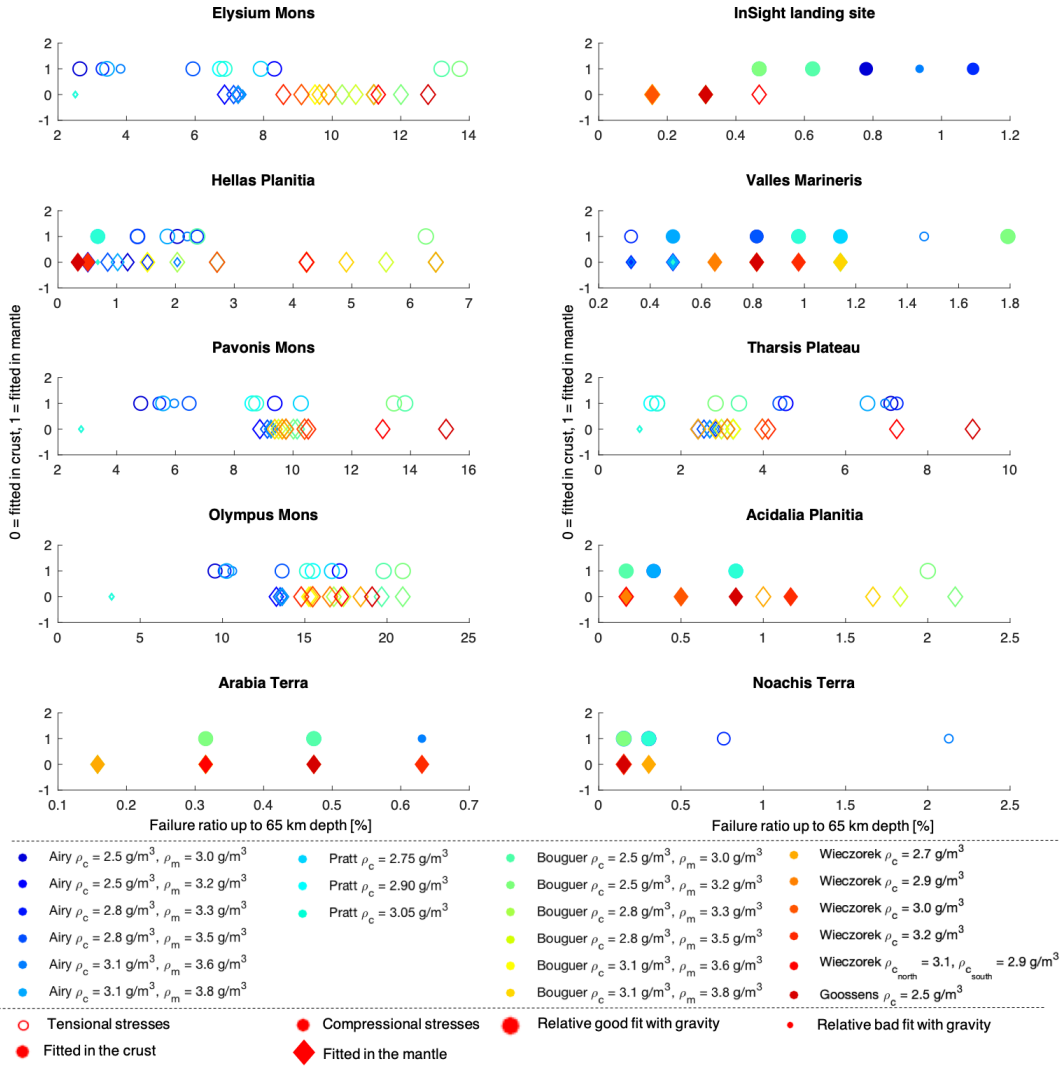

Figure 4.17: Bubble plot showing the effect of fitting with gravitational potential by placing density contrasts in the crust or mantle for a dry lithosphere with a BDT depth of 65 km. The models used for the question on the effect of crustal and mantle density are used.

all different models. All crustal and density anomalies differ form each other depending on the initial model and on its fit with the gravitational potential. However, in Figure 4.18, it can be seen that overall, fitting the models in the crust leads to higher failures ratios compared to fitting with density anomalies in the mantle. This is presumed to be because the relative differences between density in the columns become larger when fitting in the crust as most of the layer calculated for consists out of crust for some of these models (models with a high average crustal thickness). This is different from the relation of fitting in the crust of mantle with the density models, shown in Figure 4.17, where the average crustal thickness is 45 km for each model. In this figure it cannot be seen that fitting in the crust mostly leads to higher stresses as the crustal thickness is overall relatively low and the portion of mantle and crust taken into account in the equations is equally large. Lastly, it can be concluded that the size of the diamonds and circles mostly look similar, indicating only small differences between the fitting by using the mantle or crust. The crust models are slightly better (as can be seen in 4.1) as the larger part of the models consist out of crust. The only models for which the quality in fit is not similar when using the mantle or crust are the Pratt models, as the entire model is built up out of crust. It can be concluded that differences do arise when changing the fitting method, but without an unambiguous relation. Therefore, nothing is done with this result.

What is the effect of fitting the original models with the gravitational gradient, vector of potential? Figure 4.19 shows the influence of fitting the models with the gravitational tensor, vector or potential. On the y-axis

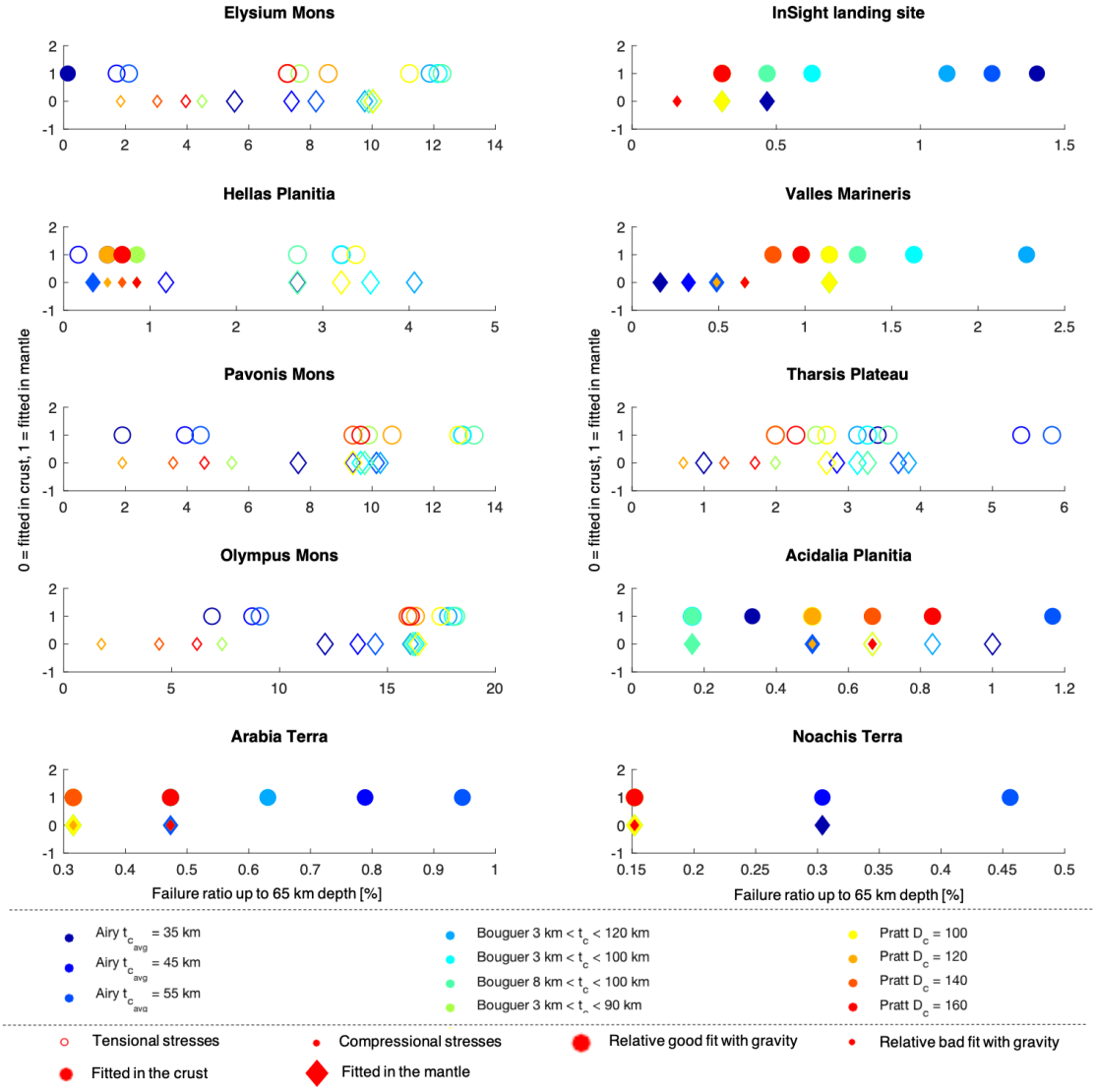

Figure 4.18: Bubble plot showing the effect of fitting with gravitational potential by placing density contrasts in the crust or mantle for a dry lithosphere with a BDT depth of 65 km. The models used for the question on the effect of the average crustal thickness are used.

the RMS of the gravitational potential residual is shown. The lower the RMS, the better the fit. On the x-axis the FR ratio with a BDT depth of 65 km is shown. In order to clearly see the influence of the fitting, the x-axis has different limits for each separate plot. The best fits are seen by fitting with the gravitational vector and gravitational potential. The worst fits can be seen by using the gravitational tensor. This agrees with the conclusion made from Figure 4.2, where the differences in fitting for one Bouguer model are shown. It can also be seen that by using the same model, but a different fitting technique, different results on the FR can be found (maximum 1,5%). It is concluded that it is different per model and per location whether one fitting method results in larger FRs than another fitting method.

What is the effect of changing the brittle-ductile transition depth? In Figure 4.20 the failure ratio maps for the five models used in previous plots are shown for three different BDT depths. Note that FR is negative in case of negative stresses (compression). In the first column, using the BDT depth of 30 km, the FRs are the most diverging and similar results for each model can be seen. In the second and last column, using a BDT depth of 65 and 80 km respectively, the results diverge per model, but lower FRs can be seen. Also, in both columns, the FR is significantly smaller than when a BDT depth of 30 km is used. This is an indication that marsquakes are more likely to happen at more shallow depths. When the baseline depth for the GPSt in-

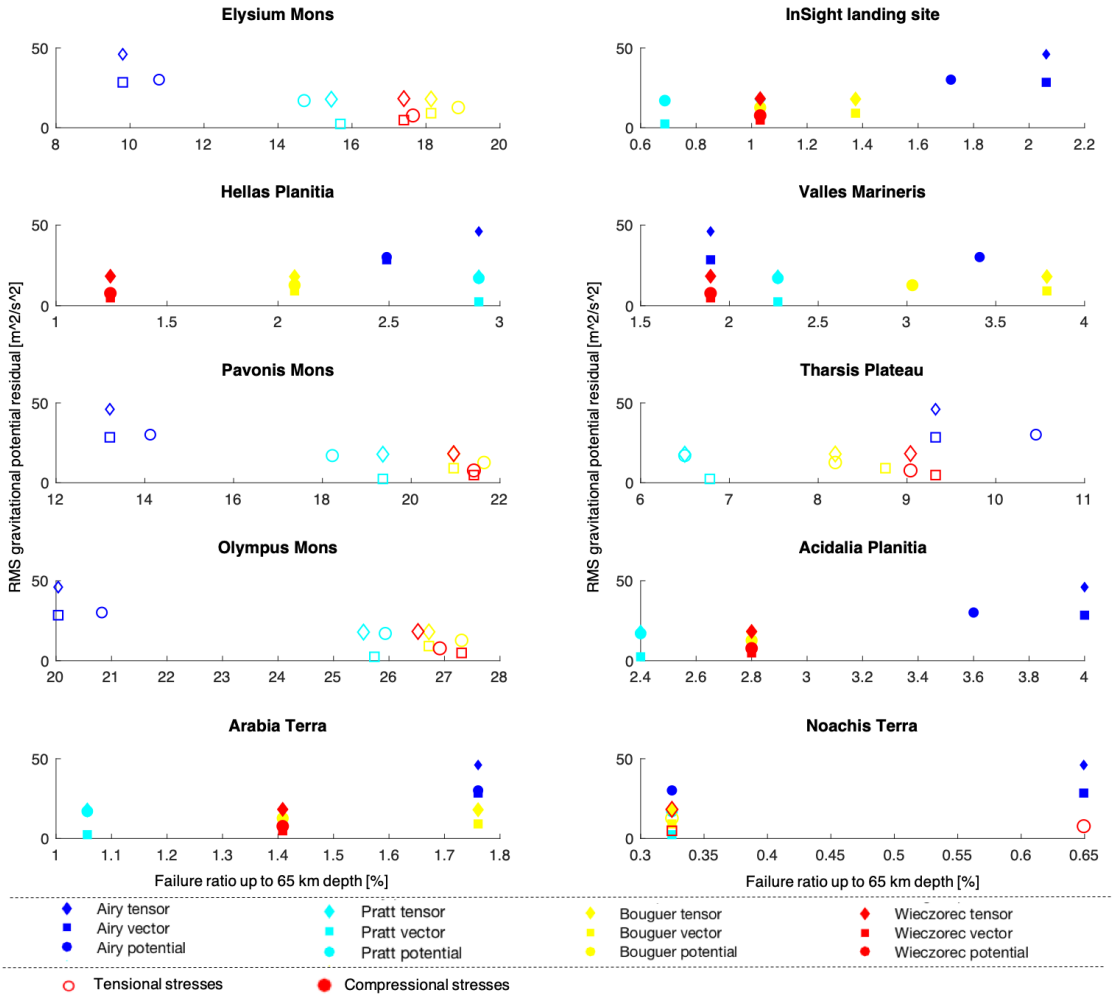

Figure 4.19: Bubble plot showing the effect of fitting with gravitational potential, vector or tensor by placing density contrasts in the crust for a dry lithosphere with a BDT depth of 65 km.

creases, the GPSt itself decreases, as shown in Figure 4.5. As previously explained, this is due to the decreasing difference in pressure between the reference column and the column being calculated for. This, combined with the fact that the only change in the YSE is that the linear line continues further down, results in the fact that the failure ratios become smaller with an increasing BDT depth.

What is the effect of a dry or wet lithosphere? This question was completely answered in Section 4.3. In Figure 4.9 and 4.10 the results can be seen. The main conclusion is that in case the lithosphere is wet, the FRs are significantly higher compared to a dry lithosphere.

From what locations are the seismic waves most likely to originate? Below, several interesting locations are discussed:

- Tharsis: the three Tharsis volcanoes cannot realistically be fitted in any of the models. The best fit is found by using the model from Wieczorek (2015) with an average crustal density of 2900 kg/m^3, however here they are still not fitted accurately (residual of $\pm$20 m/s^2). This leads to the conclusion that none of the models accurately represents what the interior of the Tharsis mountains could be like. In literature, there is still no consensus about what is happening at Tharsis. In this research a lot of seismicity is predicted in the Tharsis region, however as here the fits are not correct it is unclear how much value should be attached to this finding.
- Olympus Mons: Olympus Mons has a positive Bouguer gravity anomaly, which is counter-intuitive, as a

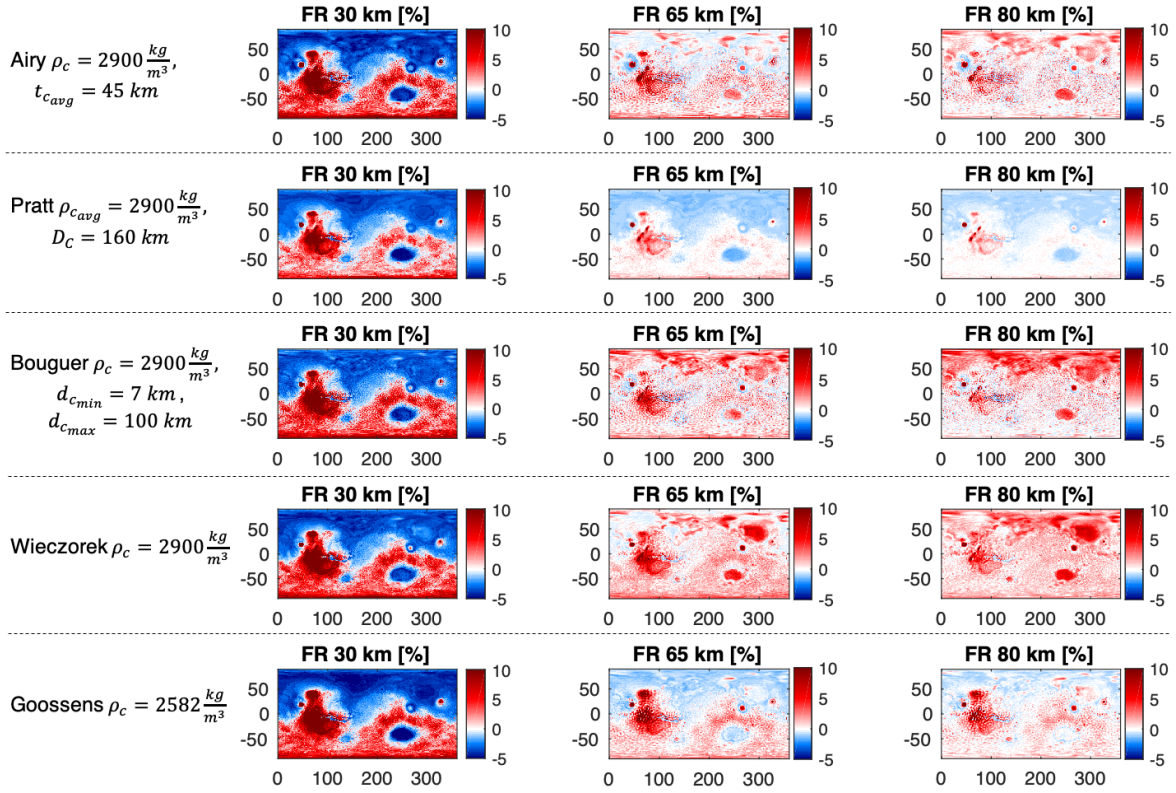

Figure 4.20: Comparison of failure ratio maps with a changing brittle-ductile transition depth for five different models, one of each type. The lower the BDT depth, the higher the FRs found. The FR maps highly correlate with the GPSt maps.

low material density is expected under large mountains/volcanoes due to isostatic compensation. This suggests that Olympus Mons is not compensated yet. The high density could also be due to the uprising lava underneath the volcano. In all models, Olympus is calculated to be in a state of tension, which is as expected. Together with the Tharsis volcanoes, the highest FRs are found at Olympus Mons. As the fits for Olympus Mons are also not as desired, the actual situation could differ from what is predicted.

- Thaumasia highlands: a significant amount of faults can be seen in the Thaumasia highlangs, all of which are presumed to be inactive. The Thaumasia highlangs are a part of the Tharsis rise where also high stresses are reached. Especially when a low BDT depth is used, the FRs reach more than 10%. This complies with the amount of tensional faults in this region. A question which remains is whether or not these faults are indeed inactive with such high failure ratios.

- Valles Marineris: the deepest and largest fault on the planet is Valles Marineris. This is a tensional fault, as can be seen in Figure 5.1. However, using the GPSt method, relatively large compressional stresses are found in Valles Marineris. This again puts the question to mind whether or not Valles Marineris is modelled accurately. The fits for this region also show to be less good than other regions.

- InSight landing site (Elysium Planitia): quakes measured by InSight will most likely not come from Elysium Planitia itself, but will have travelled towards the lander from elsewhere. The stresses at the landing site are slightly negative, ie. compressional, and their failure ratios are only a few percent for all the different models. The closest seismic origin is Elysium Mons when the BDT depth is shallow (close to 30 km). When the BDT is rather close to 65 or 80 km, the closest seismic origin towards InSight is Isidis Planitia. For the Wieczorek (2015) model with a crustal density of 2900 kg/m^3, Utopia Planitia also shows higher FR compared to the other models.

- Elysium Mons: in every model, Elysium Mons has a relatively high FR. The centre of the mountain has the highest tensional FR of the Elysium region, its surroundings have FRs close to 0 and around that

compressional FRs can be seen (among this region is the InSight landing site). Important to keep into account that the volcano itself shows relatively bad fits with the gravitational potential, so these results might not be true.

- Utopia Planitia: in most models Utopia Planitia is not an unusual area, however in several models it does stand out. Looking at topography, not much can be seen to happen at Utopia Planitia except from it being a low topographic area, however the region has an unexpected high free-air and Bouguer gravity, meaning that there is a lot of mass underneath. Using the Bouguer gravity, it suddenly shows signs of higher tensional stresses compared to its surroundings when using a large BDT depth. This could be due to the fact that Utopia Planitia can clearly be seen in the Bouguer gravity signals. Wieczorek (2015) and Goossens et al. (2017) both use gravity to calculate the crustal thickness and so does the Bouguer model. In these models (especially Wieczorek (2015) and the Bouguer models), its signature can clearly be seen in the form of higher tensional FRs compared to its surroundings. As its signature is mostly visible in the Bouguer gravity, this explains why it is not visible after fitting the Airy and Pratt models with the gravitational potential of the free-air gravity. According to Knapmeyer et al. (2006), north of Utopia Planitia is a high seismic zone. Arkani-Hamed and Riendler (2002) also identify Utopia Planitia as a high stress zone. The active fault in the north of Utopia Planitia neatly allign with the FRs calculated in that region. All of these factors make Utopia Planitia a very interesting location, even more because it is close to the InSight landing site.

- Hellas Planitia: this is an interesting location as sometimes it is seen in compression and sometimes in tension. When looking at the topography only, this region should experience compressional stresses. This is indeed the case when the BDT depth is 30 km, where the stresses mainly depend on topography. However, when looking deeper into the surface (BDT depth of 65 and or at the maximum model depth), for some models Hellas Basin can be seen in tension. This is only the case for the Bouguer and Wieczorek (2015) models. Again, this is related to the Bouguer gravity signal. Hellas Basin has a very high positive Bouguer anomaly. However, when fitting these models to the free-air gravity, negative density anomalies are introduced, which is counter-intuitive as a higher density would be expected at an impact area. This also means that Hellas Basin is not compensated yet. In the other models (Airy, Pratt and Goossens et al. (2017)) the FRs at Hellas Basin are very close to zero. According to Knapmeyer et al. (2006), south of Hellas Basin is a high seismic zone, this is not visible in the models created here.

5. DISCUSSION

A combination of the gravitational potential theory and Byerlee's law is used in order to find the most likely sources of marsquakes in different configurations of Mars. In order to do so, several interior density models are created using Airy and Pratt isostasy and using the Bouguer gravity. Also the models created by Wieczorek (2015) and Goossens et al. (2017) are used. The crustal density, average crustal thickness, fit of the model with gravity and state of the lithosphere (dry/wet and brittle-ductile transition depth) were varied in order to see the influence of these parameters on seismicity. This is all done in order to improve the efficiency of the analysis of the incoming seismic measurements by NASA's InSight mission. Below, the results of this research will be discussed and put in perspective with literature.

The simple Airy and Pratt models provide the least performing fits with reality as they assume an isostatic equilibrium and as they initially only use topography as input data. The original idea of these models was to use them as end members. Both of them succeeded in this goal, as important conclusions on the behaviour of GPSt and FRs could be made by changing their input parameters, as discussed in Section 4.4. The Bouguer models take both topography and gravity into account and result in better fits with reality compared to Airy and Pratt. Wieczorek (2015) and Goossens et al. (2017) also take both topography and gravity into account. The latter three, the Bouguer models, the Wieczorek (2015) models and the Goossens et al. (2017) model, prove to be the most realistic models used in this research. The lower crustal density used by Goossens et al. (2017) does not give significantly different results with respect to FR and GPSt compared to models with a higher density. This is because the crustal density cancels out by combining the GPSt and FR equations. Some extreme locations as the Tharsis volcanoes and Valles Marineris cannot be appropriately modelled using any of these methods. It is suggested that these locations can best be modelled while focusing only on these spots as it too hard to fit them in a global model. The Wieczorek (2015) model with a crustal density of 2900 kg/m^3 and the Bouguer model with a crustal density of 2500 kg/m^3 and crustal depth between 7 and 100 km perform best for these spots. Simple isostatic assumptions are not sufficient to explain the existence and support of these locations. This also leads to the conclusion that the Tharsis volcanoes and Valles Marineris are not isostatically compensated yet and that conclusions made about these location in this research are probably not realistic. Overall, it can be concluded that except from the Tharsis and Valles Marineris region, every model is an appropriate fit for the interior of Mars.

In Figure 5.1 the known faults on Mars are plotted underlain by the FR map calculated for the Wieczorek (2015) model with an average crustal density of 2900 kg/m^3. The fault catalogue by Knapmeyer et al. (2006) has been used. They state that almost all faults on Mars are compressional or tensional faults and almost no strike-slip faults are found. Therefore, only the compressional and tensional faults are incorporated in the catalogue. In order to improve insight into the relation between the faults and the calculated FR maps, the plots are split in two: in the left plots only the FR of tensional stresses and tensional faults are shown and in the rights plots the FR of compressional stresses and compressional faults are shown. The two top plots of the figure show the results for a BDT depth of 30 km, the two bottom plots have a BDT depth of 65 km. In all plots, a wet lithosphere is used as this results in the highest FRs and makes it easier for comparison. Looking at the top plots (BDT depth = 30 km), there are large parts where the FRs do not agree with the actual faults on Mars. First of all, the big difference is that the dichotomy can still be seen in the FR maps with a BDT depth of 30 km, whereas the faults on Mars are not related to the dichotomy. If it would have been related to the dichotomy, only compressional faults would be seen in the north and tensional faults in the south, which is clearly not the case. It is concluded that there is a low correlation between the faults on Mars and the FR map with DBT depth of 30 km. Looking at Figure 5.1, in the bottom plots, where the FR maps with a BDT depth of 65 km are shown, the correlation seems to be somewhat better but still not significantly similar. In some areas, a large amount of faults can be seen but smaller FRs are experienced. Examples are above Olympus Mons, below and right from the three Tharsis volcanoes, Tempe Terra, the region underneath Hellas Basin (Malea Planum and Promethei Terra) and the region right above Hellas Basin (Hesperia Planum). Also, some regions can be identified where relatively high FRs can be seen but almost no to no faults: Argyre Planitia, Utopia Planitia and Acidalia Planatia. Furthermore, in Isidis Planitia, the stresses are calculated to be tensional, however only compressional faults can be seen. When looking at topography, the straightforward conclusion is that stresses are compressive in this area. However, when fitting the models to the gravitational potential, large positive

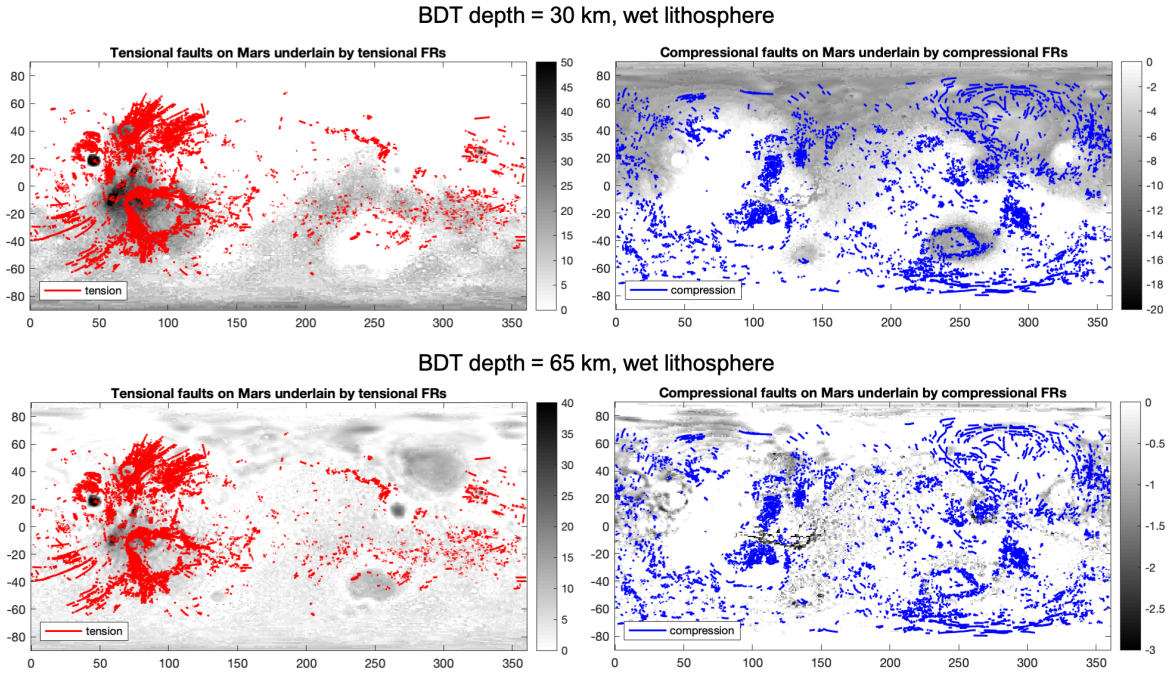

Figure 5.1: FRs overplotted by faults on Mars for the Wieczorek (2015) model with 2900 kg/m^3 as average density. The BDT depth is 30 km on the left side and 65 km on the right side. A dry lithosphere is assumed.

density anomalies need to be added in the crust at this location. This leads to a situation where there is no isostatic equilibrium and where the pressure is higher in this region compared to its surroundings, resulting in tensional stresses at that location. The same can be said for Hellas Basin when looking at the deeper BDT depth.

In Figure 5.2 FR maps overplotted with faults of the Bouguer model with an average crustal thickness of 2500 kg/m^3 and a crustal depth between 7 and 100 km are shown. The four top plots show the results with a BDT depth of 30 km, while the four bottom plots show the results with a BDT depth of 65 km. The images with a large amount of faults show all faults on Mars and the images with less faults show only the faults which are younger than 500 million years. Knapmeyer et al. (2006) made an estimation that faults which are younger than 500 million years could still be active at this moment in time. Overall, the correlation between the faults with FR maps with a BDT depth of 65 km is higher compared to the BDT depth of 30 km. This also indicates that marsquakes are more likely to come from deeper environments compared to more shallow environment. Similar conclusions compared to Figure 5.1, when all faults on Mars are shown for the Wieczorek (2015) model, can be made: similar regions show a high/low correlation of FRs and faults. Using only faults which are younger than 500 Myr, a high correlation can be seen around Utopia Planitia and around the Tharsis region. In order to be able to see this more clearly and to compare the Bouguer model with the Wieczorek (2015) model, a zoom in of these plots is shown in Figure 5.3, 5.4, 5.5 and 5.6.

Figure 5.3 and 5.4 show the tensional FR maps of (1) the Wieczorek (2015) model with an average crustal density of 2900 kg/m^3 and (2) the Bouguer model with an average crustal density of 2500 kg/m^3 overplotted with tensional faults for a BDT depth of 30 and 65 km respectively. In both figures, a zoom in of the Tharsis region is shown in the bottom plots, as in this region the most tensional faults are found. In Figure 5.3 a low correlation between the FRs and faults around Olympus Mons can be seen; compressional stresses are calculated for both the Wieczorek (2015) and Bouguer models due to the topographic lows around Olympus Mons. Around the Tharsis volcanoes, the faults and FRs seem to correlate for both models. In Figure 5.4, with a BDT depth of 65 km, some more tensional FRs are found around Olympus Mons, but still not as much as the faults show. Again, a high correlation between the faults and FRs is seen around the Tharsis mountains.

In Figure 5.5 and 5.6 the compressional FR maps of (1) the Wieczorek (2015) model with an average crustal

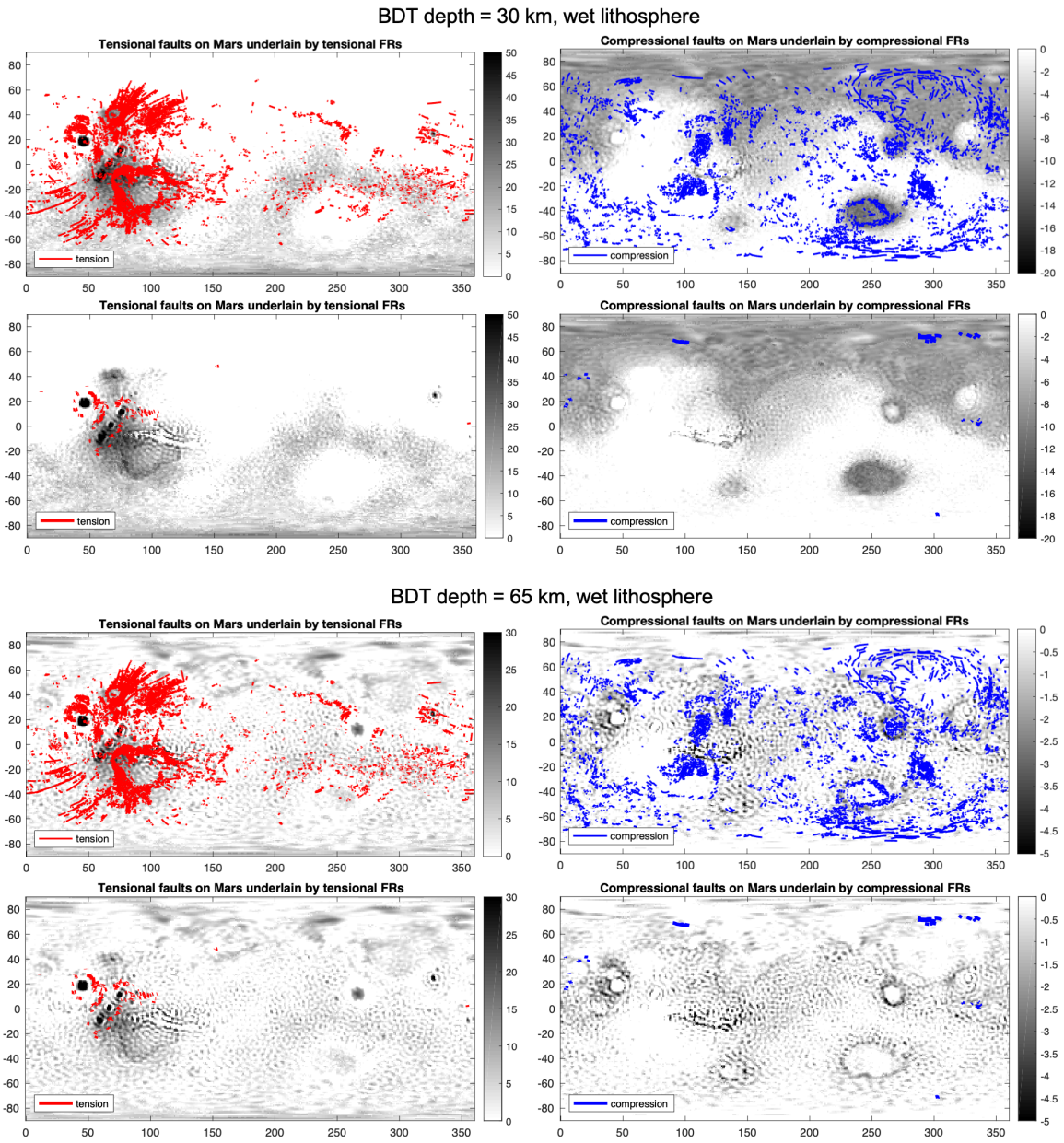

Figure 5.2: FRs overplotted by faults on Mars for the Bouguer model with 2500 kg/m^3 as average density and a crustal depth between 7 and 100 km. The BDT depth is 30 km in the top four figures and 65 km in the bottom four figures. The figures with lots of faults show all faults on Mars, the figures with less faults show only the faults younger than 500 Myr. A wet lithosphere is assumed.

density of 2900 kg/m^3 and (2) the Bouguer model with an average crustal density of 2500 kg/m^3 overplotted with compressional faults for a BDT depth of 30 and 65 km respectively are shown. In both figures, the top images show the complete map of Mars, the middle figures show a zoom in of the Utopia Planitia region and the bottom figures are zoom in of the region around Alba Patera. In both regions, the highest amount of compressional faults younger than 500 Myr are found. In Figure 5.5, in Alba Patera (middle figures), for the both the Wieczorek (2015) and Bouguer model, the faults align neatly with the FRs calculated. Also, below Elysium Mons, several active compressional faults are seen where also compressional FRs are calculated. In the bottom figures, which show the region around Alba Patera, the compressional faults also neatly align with the compressional FRs in the north and in the southwest. In Figure 5.6, showing the same results but with a BDT depth of 65 km, a lower scale on the colorbar is used as the calculated FRs are lower compared to a more shallow BDT depth. In both the Utopia Planitia and Alba Patera region, the FRs align neatly with the

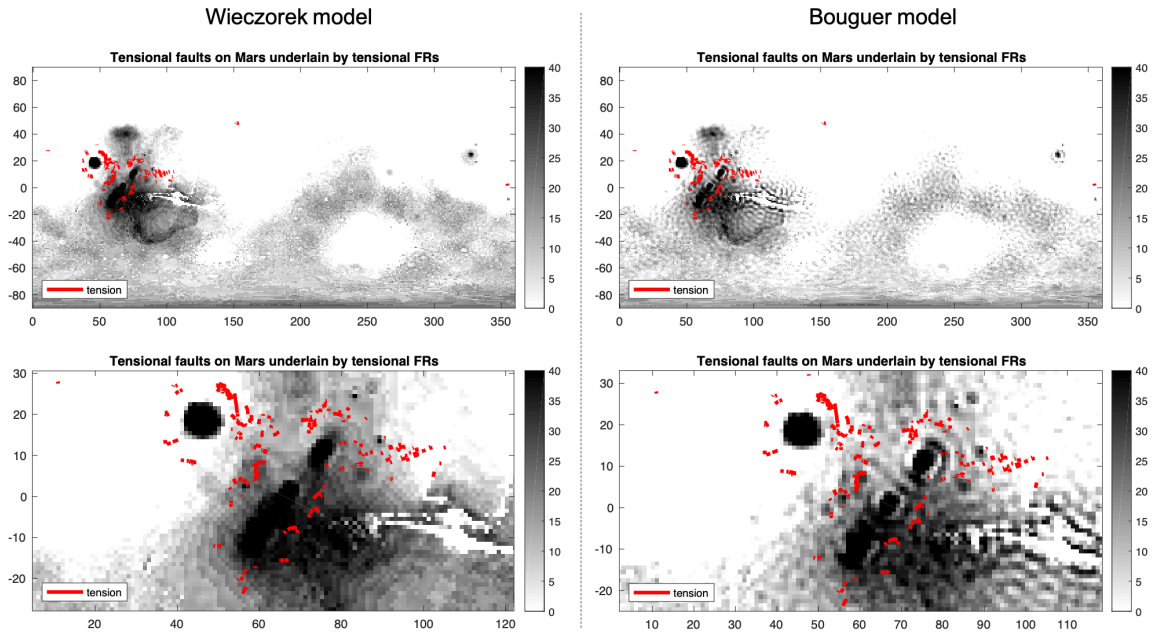

Figure 5.3: FRs with a BDT depth of 30 km overplotted by active tensional faults on Mars (age < 500 My) for the Wieczorek model with 2900 kg/m^3 as average crustal density and the Bouguer model with 2500 kg/m^3 as average crustal density and a crustal depth between 7 and 100 km. A wet lithosphere is assumed. The bottom figures consist of a zoom in of the Tharsis region.

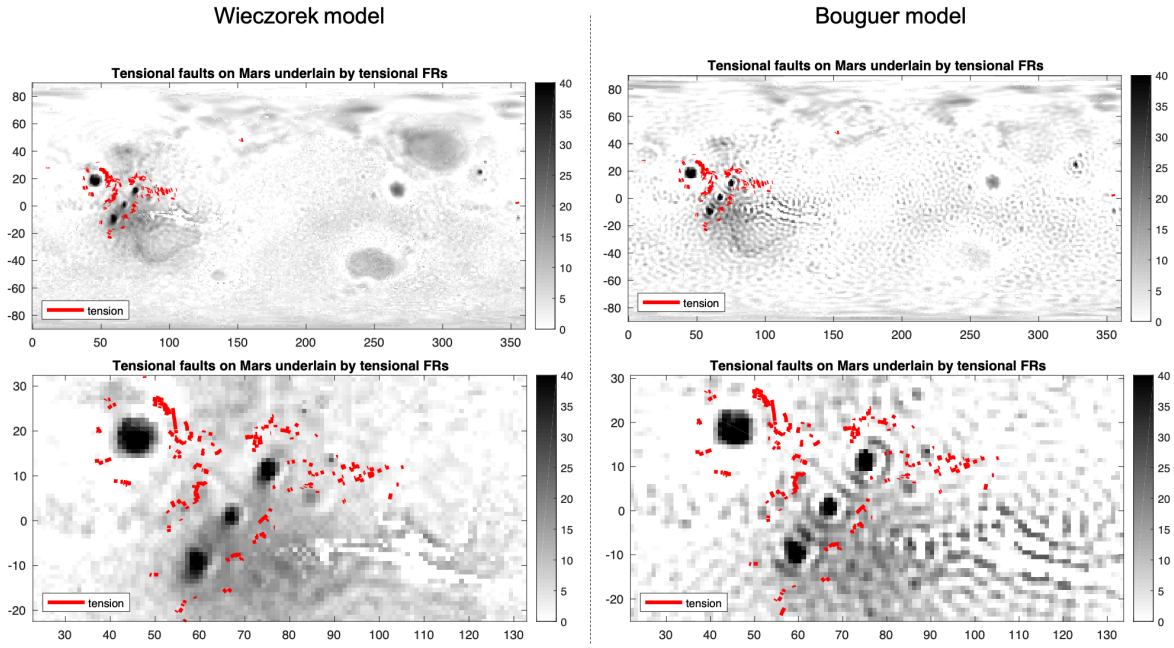

Figure 5.4: FRs with a BDT depth of 65 km overplotted by active tensional faults on Mars (age < 500 My) for the Wieczorek model with 2900 kg/m^3 as average crustal density and the Bouguer model with 2500 kg/m^3 as average crustal density and a crustal depth between 7 and 100 km. A wet lithosphere is assumed. The bottom figures consist of a zoom in of the Tharsis region.

FRs calculated. If this is true when using a BDT depth of 30 km and a BDT depth of 65 km, these locations are likely to show seismic activity.

In Plesa et al. (2018) thermal evolution models of Mars based on convective stresses and stresses due to the cooling and the contraction of Mars are used to make seismic budget estimations (discussed before in Section

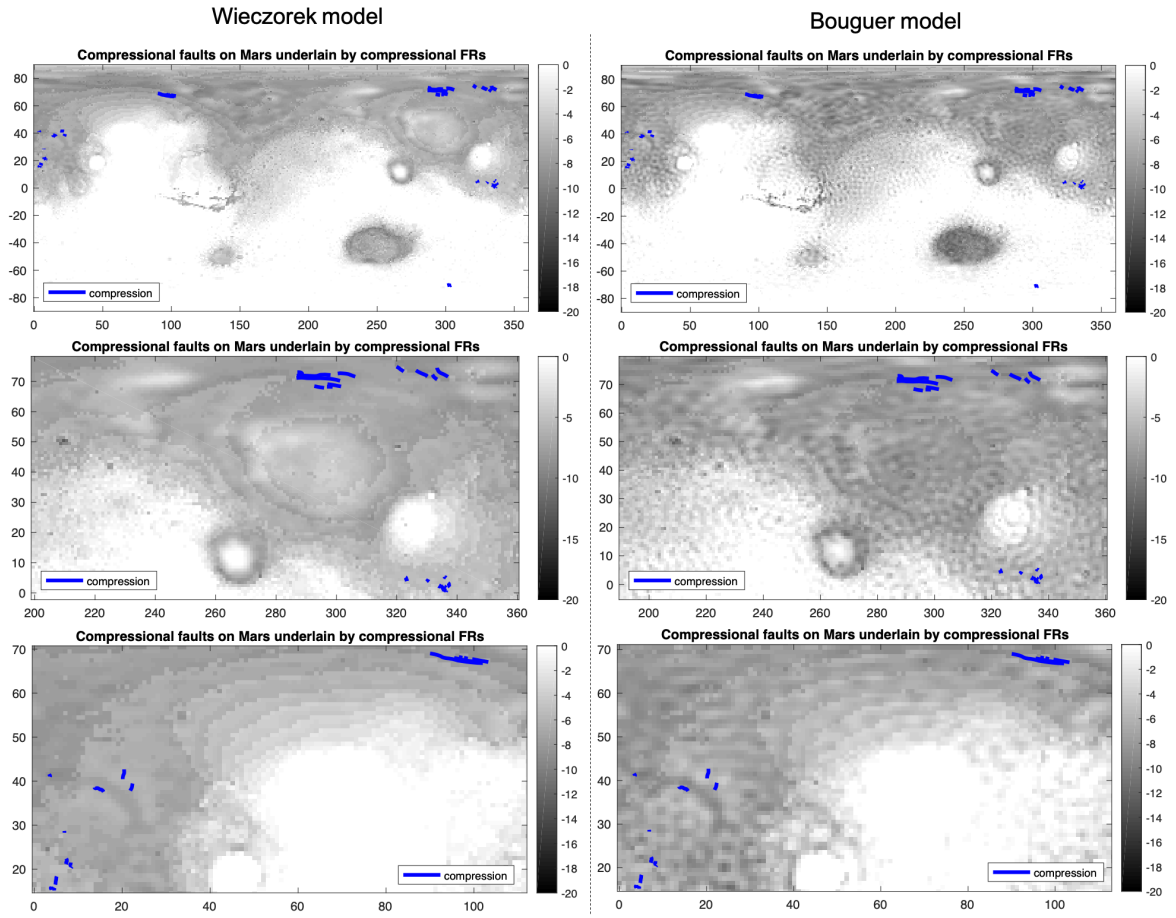

Figure 5.5: FRs with a BDT depth of 30 km overplotted by active compressive faults on Mars (age < 500 My) for the Wieczorek model with 2900 kg/m^3 as average crustal density and the Bouguer model with 2500 kg/m^3 as average crustal density and a crustal depth between 7 and 100 km. A wet lithosphere is assumed. The middle figures consist of a zoom in of the Utopia Planitia and the bottom figures are a zoom in of the region around Alba Patera.

1.3). Their main conclusion is that with a deep seismogenic depth (BDT depth) the highest seismic budget values are found in areas where the crustal thickness is small: ie. in the north and in impact basins. This is a conclusion which is also present in the Bouguer and Wieczorek (2015) models. Using a more shallow seismogenic depth they find high seismic zones around Alba Patera and between Isidis Planitia and Hellas Basin. High seismicity around Alba Patera can be found in the Goossens et al. (2017) model, however high seismicity between Isidis Planitia and Hellas Basin cannot be found in any of the models created in this research. This is due to the completely different approach in calculating seismicity. The fact that in the models created here, Tharsis is always a high seismicity zone while in Plesa et al. (2018) it is not, is because they do not use lithospheric flexure, which is the main source of stresses generated there. In the models created here, lithospheric flexure is also not taken into account but the unusually high topography of the region results in high GPTs for Tharsis.

Next, knowing the crustal density on Mars can lead to conclusions about the petrology of Mars. Unfortunately, no clear relation between density and failure ratios has been found. This means that when identifying epicenters for martian seismicity for different interior density models, no diverging results are found between the models. However, one of the main output parameters from SEIS is the travel time of the seismic body and surface waves from the epicenter towards SEIS. The travel time of the waves increases when the density is higher and decreases if the travel medium has a lower density. These measurements will put constrains on the density and the petrology of Mars. There are several suggestions towards large density differences on Mars (Arkani-Hamed and Riendler, 2002; Goossens et al., 2017). Some are implying a density dichotomy analogue to the crustal dichotomy (Plesa et al., 2018; Wieczorek, 2015). The south could have a lower density compared

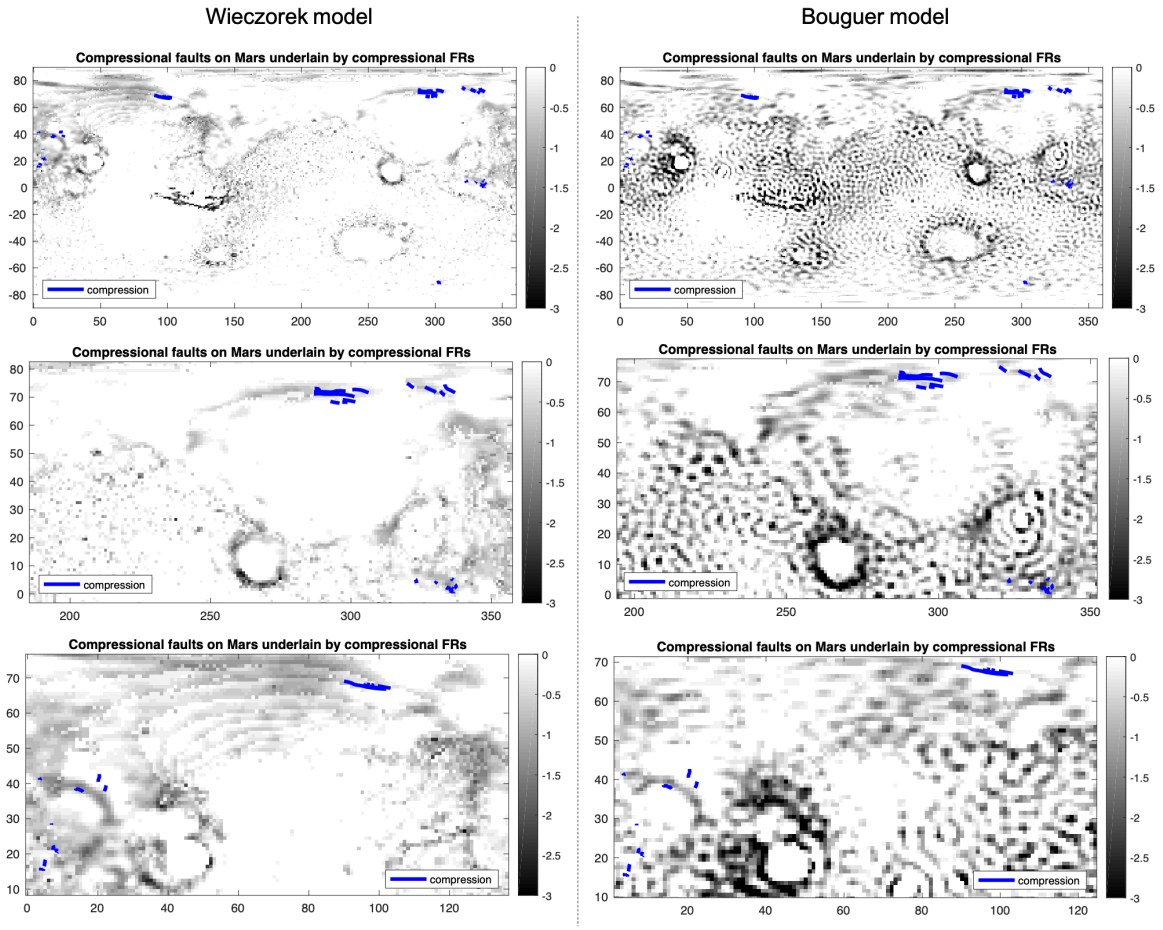

Figure 5.6: FRs with a BDT depth of 65 km overplotted by active compressive faults on Mars (age < 500 My) for the Wieczorek model with 2900 kg/m^3 as average crustal density and the Bouguer model with 2500 kg/m^3 as average crustal density and a crustal depth between 7 and 100 km. A wet lithosphere is assumed. The middle figures consist of a zoom in of the Utopia Planitia and the bottom figures are a zoom in of the region around Alba Patera.

to the north, which would be a Pratt-like model. In this research, the focus was not put into lateral density differences, but into different average crustal and mantle densities. Changing the average density did not lead to large differences in stresses and failure ratios. However, lateral density differences do lead to larger GPSts as the mass differences between respective columns becomes larger. This would be extremely interesting to research in the future.

While performing this research there were several instances during creation and fitting of the models where unrealistic densities arose. Looking at the petrology of Mars, this does put constrains on some of these models and excludes some models from being sound. First of all, a limit on the density variations during fitting of the models has been applied, as otherwise unrealistic stresses would arise. Secondly, the Pratt calculations also resulted in unrealistic densities when the compensation depth was low. Therefore, relatively high compensation depths were analyzed (≤ 100 km). According to Goossens et al. (2017) low crustal densities can be expected (around 2500 kg/m^3), whereas in other research the average crustal density is mostly expected to be around 2900 kg/m^3 (Neumann et al., 2004; Wieczorek, 2015; Wieczorek and Zuber, 2004; Zuber et al., 2000). Baratoux et al. (2014) also performed a crustal density analysis and found crustal densities that were significantly higher. They look at the chemical properties of Martian meteorites and at the Martian surface concentration of Fe, Al, Ca, Si and K using the data of the Gamma-Ray Spectrometer of Mars Odyssey. They concluded that the average crustal density is about 3100 kg/m^3 for the upper layer of Mars, which is higher compared to other literature. Therefore, it can be concluded that there is no consensus yet about the crustal

density of Mars. This is also why a lot of diverse densities were used in this research.

The total seismic moment expectations of Mars can be compared with the sums of all failure ratios of different models. For several models, high seismicity is derived and for several models low seismicity is calculated. Plesa et al. (2018) find a total seismic moment release between $5.7{\cdot}10^{16}$ Nm and $3.9{\cdot}10^{19}$ Nm per year for Mars. Their analysis takes into account convective stresses and stresses caused by mantle cooling and planetary contraction. Knapmeyer et al. (2006) finds a minimum total seismic moment of $3.42{\cdot}10^{16}$ Nm and a maximum of $4.78{\cdot}10^{18}$ Nm per year. As last, Golombek et al. (1992) find a total seismic moment of about 10^{18} Nm per year by looking at faults on Mars. The models which result in the highest seismicity in this research are the Bouguer models with a low crustal thickness range, the Wieczorek (2015) and Goossens et al. (2017) models. These could fit with the highest estimations made by Plesa et al. (2018) and Knapmeyer et al. (2006). The models resulting in low seismicity are models where compensation is assumed; Airy and Pratt. These could better fit with a total seismic moment of 10^{16} Nm per year or even less. Having a wet lithosphere and a shallow BDT depth would result in total seismic moment closest to the maximum estimated before, eg. 10^{19} Nm per year. As there is no direct relation between failure ratios and the seismic moment, only estimations can be made about the link between the total seismic moment and the sum of FRs.

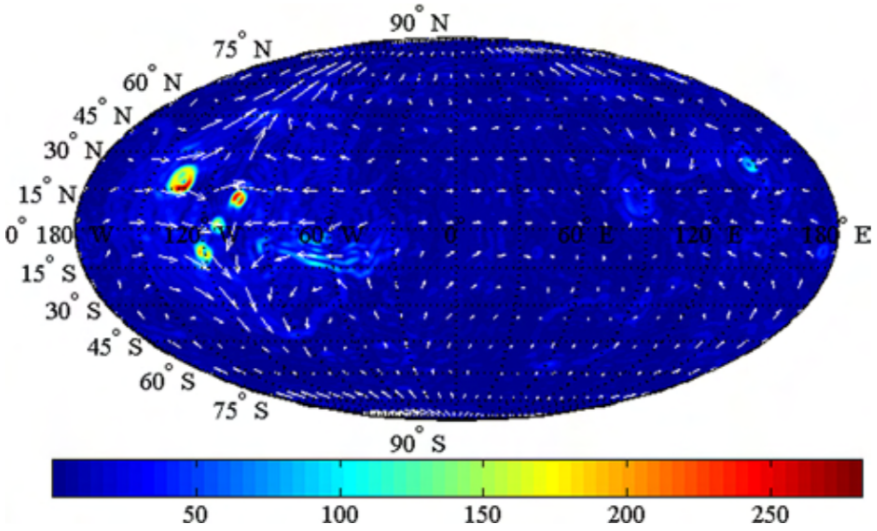

(a) Flexural stresses of Mars calculated by Tenzer et al. (2015). Stresses are shown in MPa.

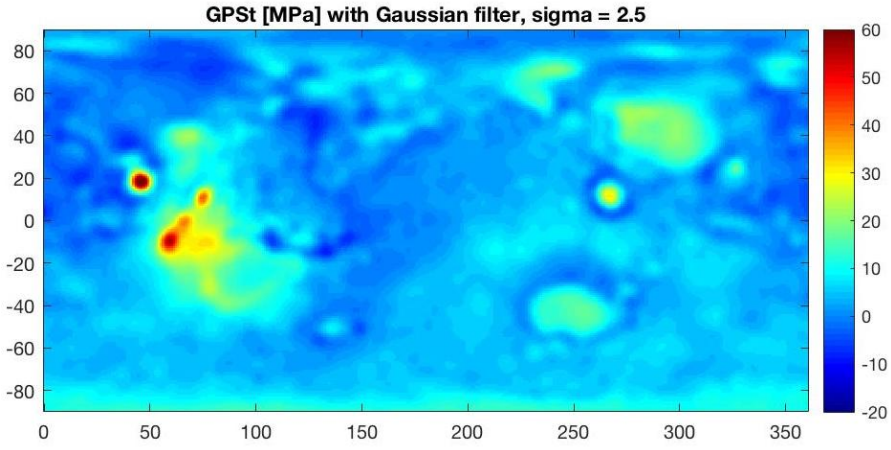

(b) Gaussian filter over the GPSt of the Wieczorek (2015) model with $\rho_c = 2900$ kg/m^3.

Figure 5.7: Comparison flexural stresses and GPSt after applying a Gaussian filter with a standard deviation of 2.5.

Important to keep into account are flexural stresses. At the start of this project it was decided to only focus

on gravitational potential stresses, which has been done successfully. However these gravitational potential stresses still need to be put into comparison with flexural stresses. As suggested by their name, flexural stresses arise due to the flexure of the lithosphere. Tenzer et al. (2015) calculated these stresses using the Vening-Meinesz inverse isostatic problem combined with the Navier-Stokes equations, their results are shown in Figure 5.7a. It can be seen that these stresses are significantly higher (from 0 to 280 MPa at Olympus Mons) than the gravitational potential stresses (on average from -50 to 80 MPa). They give the absolute value of all their stresses, but they do indicate the direction of the stress in Figure 5.7a. Flexural stresses are located in the lithosphere, similar to the GPSt. Tenzer et al. (2015) identify the crustal load of Mars as the main source of stresses, these are especially high at the Tharsis volcanoes and at Olympus Mons due to their size. As their main source of stress is the crustal loading, mostly long wavelength signatures can be found, while GPSt are very local. GPSt do not take into account its surroundings while flexural stresses do. They suggest that the huge load of Tharsis also resulted in regional tectonism which created Valles Marineris. It is also concluded from the high stresses found at the Tharsis volcanoes and Elysium Mons, that these volcanoes are not isostatically compensated yet. This agrees with findings in this research. In Figure 5.7 the GPSt of the Wieczorek (2015) model with an average crustal density of 2900 kg/m^3 after a Gaussian filter has been applied can also be seen. Applying the Gaussian filter results in a GPSt model which also takes its surroundings into account, which is attractive for comparison with the flexural stresses. Overall, Tenzer et al. (2015) find high stresses at Elysium Mons and the Tharsis region. GPSt are also found to be high at these locations. For both methods, Isidis Planitia and the surroundings of Hellas Basin also show higher stresses than average. Using GPSt, Utopia Planitia is also often a high stress zone, in the research of Tenzer et al. (2015) this cannot be seen clearly. This is thought to be because they have a very low crustal thickness at Utopia Planitia compared to its surroundings. In the models created here this is less the case. Unfortunately the color scaling of the figure by Tenzer et al. (2015) does not allow to make more elaborated conclusions about the similarities and differences between flexural stresses and GPSt.

In the future, this research can be used to easily make conclusions about the interior of Mars once seismic measurements from InSight are made. These measurements can impose limitations on the varying parameters of this research resulting in improved interior density models. This will in its place result in improved FR maps as less options of models will be left. Below, several items are listed which, if they are observed, will point towards certain parameters of the Martian interior:

- If there is a relative high total seismic moment per year, several things could be happening: (1) a shallow BDT depth is expected, (2) a wetter lithosphere is expected, (3) a small crustal thickness range over the entire planet is more likely or (4) a low level of isostatic compensation.
- High seismicity in Utopia Planitia: the model of Wieczorek with a 2900 kg/m^3 crustal density is closest to reality.
- High seismicity in Isidis Planitia: the model of Wieczorek with a 2900 kg/m^3 crustal density and Bouguer models are closest to reality.
- High seismicity in Hellas Basin: the Wieczorek (2015) model with a crustal density of 2900 kg/m^3 and Bouguer models are more likely.
- High seismicity from Tharsis: every model predicts this, in case this will not be measured, Tharsis must somehow be isostatically compensated and more research is needed towards what Mars looks like below Tharsis. If seismic activity is present on a large part of the Tharsis plateau, the Goossens et al. (2017) model is more likely (low density with higher density at Tharsis). If seismic activity only originates at the volcanoes itself, the other four types of models are more likely.
- High seismicity from Elysium Mons: the same conclusion as for Tharsis can be made. Every model predicts this, if this is not the case, a lot more research towards this location is needed.
- More seismicity from the north compared to the south: The Bouguer or Wieczorek models are closest to the actual situation.
- More seismicity from the south compared to the north: the Pratt assumptions might be somewhat realistic on Mars. This also indicates the presence of a density dichotomy.

Overall, several conclusions could be made on seismicity which would improve the efficiency of analysis of InSight seismic measurements. The most important are on several different high seismicity locations for different models and on the implications of a lower or higher total seismic budget. It was initially expected that the average crustal density would have a high influence on the seismic predictions, which turned out to be not true. The brittle-ductile transition depth and the amount of liquid present in Mars its lithosphere are discovered to be the most important parameters with respect to seismicity. It is again implied by this research how great of a value seismic measurements on Mars would be. The prospect of measurements of InSight its seismometer is exciting for everyone interested in space exploration or a future human settlement on Mars.

6. CONCLUSION

This research was performed in order to derive clear a-priori estimations about the most likely epicenters of Martian seismicity. A set of interior density models of Mars were created, based on Airy and Pratt isostatic principles, on the Bouguer gravity anomaly and derived from Wieczorek (2015) and Goossens et al. (2017). For all these models the gravitational potential stress fields were calculated and compared with the yield stress. The yield stress was calculated using Byerlee's law. The parameter chosen to compare all the interior density models created is the failure ratio (FR). This is the ratio between the depth of the lithosphere at which point the yield stress is reached and the brittle-ductile transition depth. It is a signature of what percentage of the lithosphere can fail. Several parameters were chosen to be variable in order to test the sensitivity of the failure ratio. The variable parameters are as follows: (1) the crustal density, (2) crustal thickness, (3) whether the model is fitted by density anomalies in the crust or mantle and (4) with the gravitational potential, vector or gradient, (5) the brittle-ductile transition depth (BDT depth) and (6) whether the lithosphere of Mars is in a wet, dry or hydrostatic state. Finally, by combining all the results from different types of models with varying input parameters, a well defined answer to the research question could be formulated:

Where are the most likely seismic epicenters of marsquakes derived from gravitational potential theory to be measured by the InSight mission?

The effect of the average crustal density on the FR ratios was initially expected to be large, but the relation between the two appeared to be minimal. This is because the density cancels out while combining the gravitational potential stresses equation and Byerlee's law (YSE). However it is concluded that large lateral differences in density lead to larger GPSts and FRs. The second variable parameter, the average crustal thickness is more important. The depth of the average crustal thickness is also a signature for the depth at which a certain amount of isostatic compensation is reached. When the average crustal thickness is close to the BDT depth, lower FRs are found compared to when this is not the case. The amount of seismicity measured by InSight can thus lead to conclusions about the relation between the average crustal thickness and the BDT depth. Fitting the interior density models with the gravitational tensor, vector or potential by adding density anomalies in the crust or mantle does have an effect on the final result, as some fitting choices lead to better models. The best fits are found by fitting with the gravitational vector or potential by using density anomalies in the crust. This can be explained by the models consisting mainly out of crust and less out of mantle. The same density anomaly imposed in the crust has thus a larger effect on the final model compared to when it is put in the mantle. The largest effect on the FRs are due to a wet or dry lithosphere and due to the brittle-ductile transition depth. A dry lithosphere is significantly stronger than a wet one, therefore in a wet lithosphere more seismicity occurs. A shallow BDT depth will also result in more seismicity compared to a deeper BDT depth. This is due to decreasing gravitational potential stresses with greater depths, because with greater depths the amount of compensation that has been reached increases. In the most shallow layers, not much compensation has been reached yet. The yield stresses also increase with depth, which results in faster failure at small depths. Combining these two factors results in increased FRs when the BDT depth is smaller. The main conclusion is that GPSts and FRs are lower when the level of compensation is higher, that is why the Airy and Pratt models result in low seismic estimations, while the Bouguer, Wieczorek (2015) and Goossens et al. (2017) models result in higher seismic estimations.

Several high failure ratio regions could be identified by using all these models. Interesting regions to keep into mind are Utopia Planitia, Isidis Planitia, Hellas Basin, the Tharsis region and Elyisium Mons. Seismic events happening at the first three locations are signatures of the Bouguer and Wieczorek (2015) models being most realistic. Seismic events happening in the Tharsis region and at Elysium Mons are expected for every model. In case this does not happen some unknown structures are present at these locations. North of Utopia Planitia, south of Elysium Mons, north and west from Alba Patera and around the Tharsis volcanoes are all locations where the youngest faults on Mars neatly align with the failure ratios calculated for most models. The young faults (< 500 million years) are assumed to be active at this moment in time. This means that marsquakes originating in these locations are most likely to happen. In case of a higher number of seismic events in the south compared to the north, Pratt-like isostatic compensation on Mars could be occurring, which points towards a higher density in the north. In case the overall total seismic moment on the planet is

higher than expected, some of the following features could be present: (1) a shallow BDT depth, (2) a wetter lithosphere, (3) an average crustal thickness far from the BDT depth, (4) large lateral density variations and (5) less isostatic compensation than expected.

With this research, the analysis from incoming InSight data can be ameliorated. Obtained conclusions will in its place lead to more constrained interior density models of Mars, which can lead to even better seismic predictions. Having an interior density model of Mars will eventually lead to more clarity about the formation of the terrestrial planets in the solar system. This research is an elementary part in knowing the human origin and making it possible for a human settlement on Mars to be created.

7. RECOMMENDATIONS

The take home message from this thesis is that there are a lot of unknowns regarding Martian seismicity, but by performing more research and by comparing research on this subject to measurements made by InSight, all these unknowns can be constrained more and more. There is a lot of research left to be done on this subject before it will be known what the interior of Mars actually looks like. Therefore, before closing this thesis, some useful recommendations for future research on this topic are given.

The first and most evident recommendation is to acquire more data on Mars. This sounds a bit straight forward as this is a recommendation made for almost every research subject, however that does not mean it is less true. Having a higher resolution of the gravitational measurements of Mars will open the possibility to create better interior density maps as the models can then be created and fitted using an ameliorated gravitational map which is closer to reality. Seismic data is also needed, having only a few seismic measurements will already result in improved estimations about the density in the crust and upper mantle of Mars. Incoming seismic measurements can be linked to the models created here in order to see which models are more likely to be close to reality. As last, incorporating even more interior density models created by scientist before would be beneficial. So far, only data from two authors has been used, however more than these two authors have worked on the interior density of Mars. Other authors were contacted but unfortunately, no meaningful reply was received. In the future, more effort could be put into retrieving the data from other scientists. Using more data, each created with a different approach, could result in a larger amount of interesting conclusions.

Secondly, more research should be performed towards lateral density variations on Mars. There are already suggestions that the north has a higher density compared to the south, however the focus was not on this density contrast in this research. This would be an interesting factor to study in the upcoming research. The crustal dichotomy of Mars and the Tharsis rise are still some of the two biggest questions of the planet. More research towards density profiles could lead to more concise answers of how these two features arose.

The method to compare the gravitational potential stresses with the yield stresses could be applied in more detail. For now, the GPSt over an entire column is taken and compared with the yield stress as a function of depth. The GPSt or a similar stress per depth instead of over an entire column could also be used. In this research this was not done as it is too computationally intense and too much data would have been created. The amount of data could not be processed with an ordinary laptop. It would have been possible to do this for a few models but not for as many as have been used now. Using another programming language (here Matlab was used) or using a more advanced computer/laptop, such kind of research could be possible. Also, important to keep into account while performing this kind of research is how to evidently display the results.

A very interesting concept would be if the failure ratios could be fitted to the magnitudes of marsquakes. While performing this research, no information on how to do this could be found. Therefore in this research only estimations are made of the total seismic moment by looking at the sum of all failure ratios of each model. If there were to be a method discovered to predict expected seismic magnitudes by comparing stresses with the YSE, that would be a huge leap forward in the seismic science field. For this research, the results would become a lot more concise and less dubious. Performing research towards this relation is a large recommendation. It is presumed to be only possible to find such a relation once seismic measurements of the planet are available. Luckily, InSight its measurements will start coming in soon if its landing and deployment go as planned.

Next, if more time is available, more focus could be put into the incorporation of flexural stresses. For now, flexural stresses are only taken into account in the discussion, and for this a model which was created before was used. A flexural model using the same assumptions as the models used here could be incorporated, this would result in a more coherent model than using the models created by other authors which often use slightly different input parameters. The overall use of flexural stresses results in more accurate predictions of seismicity compared to exclusively using gravitational potential stresses.

During this research a lot of time and effort has been put into testing the effect of changing the crustal and mantle density and changing the average crustal thickness on the final failure ratios. However, both the density and crustal thickness seemed to have a minor effect on the final failure ratios. The parameters which did have a large effect are (1) the brittle-ductile transition depth, as above this depth marsquakes are expected to occur and below this depth they are not expected to occur, and (2) how much liquid is present in the Martian lithosphere, as the more liquid present, the weaker the material. These two items significantly change the results, therefore it would be better to focus on these parameters in upcoming research.

As last, it has been proven that this method works and provides interesting results, therefore it suggested to use this method on other planets/moons as well. The calculation of gravitational potential stresses is a simple idea but has not been used often in research before. As shown here, it can lead to conclusions about seismicity by using Byerlee's law to calculate yield stress envelopes. Consequently, using GPSt on other planets will also result in renewing research and a different view on the planet. Combining it with the YSE will even be better. If this kind of research would be done on the other terrestrial planets of this solar system, differences and/or similarities between each planet could be found, which can indicate more information about the formation of each planet and the entire solar system.

A. VERIFICATION & VALIDATION

The programming process is divided into three main phases: (1) the creation of the radial density models and the calculation of the gravitational potential (implementation of Root et al. (2016) their software) for each model while fitting them, (2) the calculation of gravitational potential stresses and (3) the seismicity analysis by use of Byerlee's law. Additionally, the creation of all plots is also discussed. Each phase is verified accordingly. In this appendix, all steps until complete verification is reached are described. All software was written in Matlab. The V&V process proved to be very useful as several mistakes were found and eliminated. The final V&V steps performed (which all passed the test) are stated in this chapter.

A.1. INTERIOR DENSITY MODELS

There is one main division between the programs used: (1) the creation of all the initial models and (2) the fitting of these models using the software of Root et al. (2016).

A.1.1. CREATION OF THE MODELS

First of all, all models are created. For each type of models several points which are checked are given.

Airy

- Check manually if the Airy calculations have been done correctly for several points. **Correct**
- Plot the crustal thickness and see if it looks similar to literature (Goossens et al., 2017; Neumann et al., 2004; Wieczorek, 2007; Zuber et al., 2000) and if it matches with topography. **Correct**
- Plot the crustal thickness and check if the maximum and minimum thickness are within the expected ranges. **Correct**

Pratt

- Check manually if the Pratt calculations have been done correctly for several points. **Correct**
- Plot the crustal density and see if it matches with topography, ie. low density for higher topography and high density for low topography. **Correct**
- Plot the crustal thickness and check if it is equal to the compensation depth plus the topography. **Correct**

Bouguer

- Check the calculated Bouguer gravity anomaly with what was done previously by literature (Wieczorek (2015) and NASA[1]). **Correct**
- Check manually if the calculation of the crustal thickness derived from the Bouguer gravity has been done correctly for several points.
- Plot the crustal thickness and see if it looks similar to literature (Goossens et al., 2017; Neumann et al., 2004; Wieczorek, 2007; Zuber et al., 2000) **Correct**
- Plot the crustal thickness and check if the maximum and minimum crustal depth are within the input ranges. **Correct**

Wieczorek and Goossens models

- Check for both models if the model data has been read into program correctly. **Correct**
- Check for both models if the data has been transformed to the desired size correctly. **Correct**
- Plot both models and see if the crustal thickness and density maps are the same as Wieczorek (2015) and Goossens et al. (2017) state in their articles. **Correct**

[1] URL `https://svs.gsfc.nasa.gov/4436` [12-06-2018]

All models
These are several programming features which are applied to each model. They are tested for every model, however as the procedure is exactly the same for each model, the checks are only stated once.

- Check if the input data to the programs is correctly being read into Matlab (ie. topography data and gravitational data). **Correct**
- Check if the final result is correctly written into a `.txt` file. **Correct**
- Check if the final result has the correct format. **Correct**
- Check all input files with the function `visual_gmtfile.m` provided by Root et al. (2016). This functions plots the input density and boundary files of a layer. **Correct**
- Check if the areoid is correctly subtracted from the models. **Correct**

`Matrix2gmt.m`
This is a function which transforms a data matrix from a 180x360 format to a `.gmt` format: 64800x3.

- Compare several input and output elements with each other: check if they are the same and if they are in the correct location. **Correct**

`max50km.m` & `max50kmcheck.m`
Both are verified simultaneously as these functions closely work together. These functions split the layers of the radial density models into layers which are all thinner than 50 km.

- Plot input and output layers. **Correct**
- Check with test radial density models of 40, 70 and 120 km. **Correct**
- Check if all output layers are never thicker than 50 km. **Correct**

A.1.2. FITTING BY USE OF GRAVITATIONAL POTENTIAL

The software of Root et al. (2016) calculates the gravitational potential from a radial density profile. The calculated gravitational potential can then be compared with the actual gravitational potential. The gravitational potential residual indicates how well the density profile fits with the reality. The software of Root et al. (2016) has already been verified and validated extensively by the creators. Here, the correct use of the software is checked together with the calculation of the gravitational potential and the fitting process.

Correct use of software The software is originally used for Earth data. For this project it is verified for data of Mars. The following steps are performed:

- Check if the program works with data from the Earth (10 layers). **Correct**
- Check if the program runs with a simple data model from Mars (1 layer). **Correct**
- Check if the Mars input data is built up in a similar way compared to the data for the Earth. **Correct**
- Check the output plot of the gravitational potential is similar to the measured data. **Correct**

Residual calculation

- Check if the measured gravitational potential is correctly read by Matlab. **Correct**
- Check if the coordinate system of the actual and calculated data is the same. **Correct**
- Check the residual calculation manually for several data points. **Correct**
- Check the RMS calculation manually for a small part of the data. **Correct**

Fitting tool

- Plot the old density, new density, old gravitational potential and new gravitational potential in order to see if the correct data is updated. **Correct**
- Check if the best solution is saved by running the saved model. **Correct**
- If σ is put equal to zero, nothing should change in the models. **Correct**
- Check if the density in the changing layer does not exceed the limits set. **Correct**

A.2. GRAVITATIONAL POTENTIAL STRESSES

In this Matlab routine the density layers also serve as an input. The outputs are the gravitational potential energy and stresses.

- Check if the files are correctly being imported by Matlab. **Correct**
- Check manually if the correct minimum and maximum values are being found. **Correct**
- Check if the 3D matrix containing the layers is correctly created (`dens_l` and `crust_l`). **Correct**
- Check if the 3D matrix containing all data is correctly created (`dens_3d`). The minimum and maximum value of several layers is checked. **Correct**
- Check if similar same results are found with a different step size in depth. **Correct**
- Check if the equations are solved/programmed correctly by manually calculating a few points **Correct**
- Check the dependence on the reference column. Using a different reference column with also zero topography the same results should be found. **Correct**
- Check for several points manually whether the GPE and GPSt calculations are correct. **Correct**
- When using a Pratt model which is not fitted with gravity yet, the GPSt should be mostly zero with only minor rounding errors. **Correct**
- Check the order of magnitude of the GPE and GPSt and compare to what is found in literature. According to Raulin (2007) the ranges for GPE and GPSt found on Earth in Fennoscandia are as follows: GPE lies between -2 and $1{\cdot}10^{12}$N/m and GPSt lies between -15 and 6 MPa. Similar magnitudes are indeed found except from the extreme locations on Mars (eg. Tharsis). This is as expected. **Correct**

A.3. SEISMICITY

In the program used to check seismicity, the YSE is only calculated up to the depth where the yield stress at that location is reached. The ratio between that depth and the brittle-ductile transition depth (failure ratio or FR) is used for further analysis.

- Check if the the same YSE are found when using input variables from an example. The example of Burg (2017) is used. **Correct**
- Check if each time the YSE is calculated with the crustal density at that location. **Correct**
- Calculate the FR manually for several points. **Correct**

A.4. PLOTS USED FOR ANALYSIS

Everytime something is plotted the following items are checked:

- Check if the correct data is being read into Matlab. **Correct**
- Check if the correct data is plotted. **Correct**
- Check if while plotting the correct order of models is used for each input array to the plot. **Correct**
- Check if the correct units are used. **Correct**

B. SPHERICAL HARMONICS

In this appendix, the general equations for the spherical harmonics representation are given. First of all, the Legendre Polynomial is given as this is necessary for the correct understanding of spherical harmonics. Next, the spherical harmonics equations are given followed by some useful analysis tools for these equations. All information is derived from Klees (2000) and Wieczorek (2007) unless stated otherwise.

B.1. LEGENDRE POLYNOMIAL

The Legendre polynomial is needed for the derivation of spherical harmonics, therefore it is already shortly presented here. The Legrendre polynomial is the expression that forms the solution to Legendre's differential equation:

$$\left[(1-x^2)\frac{d^2}{dx^2} - 2x\frac{d}{dx} + n(n+1)\right] P_n(x) = 0 \tag{B.1}$$

Solving this results in;

$$P_n^m(x) = \frac{1}{2^n n!}(1-x^2)^{m/2}\frac{d^{n+m}}{dx^{n+m}}(x^2-1)^n, \quad \text{for } m = -n, -n+1, ..., n-1, n \tag{B.2}$$

Below, the first Legendre polynomials are stated:

- $P_0(x) = 1$
- $P_1(x) = x$
- $P_2(x) = \frac{1}{2}(3t^2 - 1)$
- $P_3(x) = \frac{1}{2}(5x^3 - 3x)$
- $P_4(x) = \frac{1}{8}(35x^4 - 30x^2 + 3)$

When $t = cos(\alpha)$ the equations result in:

- $P_0(cos(\alpha)) = 1$
- $P_1(cos(\alpha)) = cos(\alpha)$
- $P_2(cos(\alpha)) = \frac{3}{4}cos(2\alpha) + \frac{1}{4}$
- $P_3(cos(\alpha)) = \frac{5}{8}cos(3\alpha) + \frac{3}{8}cos(\alpha)$
- $P_4(cos(\alpha)) = \frac{35}{64}cos(4\alpha) + \frac{5}{16}cos(2\alpha) + \frac{9}{64}$

The best method to compute high order polynomials is by using the following recursive equation:

$$(n+1)P_{n+1}(x) = (2n+1)xP_n(x) - nP_{n-1}(x), \quad \text{for } n = 1, 2, 3, ... \tag{B.3}$$

In case the following equation is defined:

$$cos\gamma = cos\theta_1 cos\theta_2 + sin\theta_1 sin\theta_2 cos(\phi_1 - \phi_2) \tag{B.4}$$

Then the addition theorem of the Legendre polynomial gives the following equality:

$$P_n(cos\gamma) = \frac{4\pi}{2n+1}\sum_{m=-n}^{n} Y_n^m(\theta_1, \phi_1)\bar{Y}_n^m(\theta_2, \phi_2) \tag{B.5}$$

B.1.1. DERIVATION SPHERICAL HARMONICS

First of all the question as to what a harmonic function is has to be answered. There are three factors that apply to a harmonic function: (1) it satisfies the equation of Laplace (Equation B.6), (2) its first derivatives are continuous and have a single value and (3) the function has second derivatives (Blakely, 1996).

$$\nabla^2 f = \frac{\delta^2 f}{\delta x^2} + \frac{\delta^2 f}{\delta y^2} + \frac{\delta^2 f}{\delta z^2} = 0 \rightarrow \Delta f = 0 \tag{B.6}$$

Now, the spherical harmonic function is a set of orthogonal basis functions on the surface of a sphere. According to Wieczorek (2007), the spherical harmonic equations are as follows:

$$f(\Omega) = \sum_{n=0}^{\infty} \sum_{m=-n}^{n} f_{nm} Y_{nm}(\Omega) \tag{B.7}$$

In this equation Ω is the position on the sphere, $\Omega(\theta, \psi)$, f_{nm} is the corresponding expansion coefficient and Y_{nm} is the spherical harmonic function of degree n and order m:

$$Y_{nm}(\Omega) \begin{cases} \bar{P}_{nm}(\mu)(cos\theta)cos(m\psi) & m \geq 0 \\ \bar{P}_{n|m|}(\mu)(cos\theta)sin(|m|\psi) & m < 0 \end{cases} \tag{B.8}$$

Where $\bar{P}_{nm}(\mu)$ are the normalized associated Legendre functions:

$$\bar{P}_{nm}(\mu) = \sqrt{(2-\delta_{0m})(2n+1)\frac{(n-m)!}{(n+m)!}} P_{nm}(\mu) \tag{B.9}$$

And P_{nm} the normalized Legendre functions:

$$P_{nm}(\mu) = (1-\mu^2)^{m/2} \frac{d^m}{d\mu^m} P_l(\mu) \tag{B.10}$$

$$P_n(\mu) = \frac{1}{2^n n!} \frac{d^n}{d\mu^n} (\mu^2 - 1)^n \tag{B.11}$$

B.1.2. ANALYSIS TOOLS

In this section some useful tools to get some better understanding of the spherical harmonic equations are given. Only the mathematical descriptions are given here. In later research these methods are being used and conclusions on their effectiveness are made.

First of all, a useful tool to image the contributions of each separate harmonic degree is the degree variance (DV). Plotting results of this equation can tell more about which wavelengths have what contribution.

$$DV = 10log^{10} \left[\sum_{m=0}^{n} C_{nm}^2 + S_{nm}^2 \right] \tag{B.12}$$

Next, the power spectrum of a spherical harmonic function can be calculated:

$$S_{ff}(n) = \sum_{m=-n}^{n} f_{nm}^2 \tag{B.13}$$

While the cross-power of two functions f and g is given by:

$$S_{fg}(n) = \sum_{m=-n}^{n} f_{nm} g_{lm} \tag{B.14}$$

The power spectra are related to the last two analysis tools worth mentioning: the correlation and admittance. Both are used for comparison between two spherical harmonic functions, a good example of this is the comparison between topographic and gravitational data. The correlation, $\gamma(n)$ between two data sets is defined as:

$$\gamma(n) = \frac{S_{hg}(l)}{\sqrt{S_{hh}(l) S_{gg}(l)}} \tag{B.15}$$

Note that the term coherence is often used for the squared correlation, however not every author does this the same. The term coherence and correlation are also mixed up sometimes (Wieczorek, 2007). As last, the admittance, $Z(n)$ is defined as follows:

$$Z(n) = \frac{S_{hg}(l)}{S_{hh}(l)} \tag{B.16}$$

C. GEOGRAPHIC COORDINATES

In this appendix the geographic coordinates of specific locations used in this research are given.

Location name	Latitude [deg]	Longitude [deg]	Matlab code
Elysium Mons	25	148	[115,328]
InSight landing site	-5	137	[85,317]
Hellas Planitia	-40	72	[50,252]
Valles Marineris	-9	-72	[81,108]
Pavonis Mons	1	-112	[91,68]
Tharsis Plateau	7	-107	[97,73]
Olympus Mons	18	-132	[108,48]
Acidalia Planitia	56	-26	[146,154]
Arabia Terra	7	1	[97,181]
Noachis Terra	-56	-10	[34,170]

Table C.1: Geographic coordinates of locations used in the bubble plots of the research, see Figure 4.12, 4.15, 4.17, 4.18 and 4.19.

Location name	Latitude [deg]	Longitude [deg]	Matlab code
Elysium Mons	25	148	[115,328]
InSight landing site	-5	137	[85,317]
Hellas Planitia	-40	72	[50,252]
Valles Marineris	-9	-72	[81,108]
Tharsis Plateau	7	-107 [97,73]	
Olympus Mons	18	-132	[108,48]

Table C.2: Geographic coordinates of locations used to show the change of GPSt with depth in the research, see Figure 4.5.

Location name	Latitude [deg]	Longitude [deg]	Matlab code
Amazonis Planitia	-13	88	[77,32]
Chryse Planitia	-32	27	[63,148]
Cydonia Mensae	1	45	[45,181]
Hellas Planitia	74	-31	[121,254]
Isidis Planitia	111	4	[86,291]
Elysium Planitia	161	20	[70,341]

Table C.3: Geographic coordinates of locations used as reference columns in the research.

BIBLIOGRAPHY

Arkani-Hamed, J. and Riendler, L. (2002), 'Stress differences in the martian lithosphere: Constraints on the thermal state of mars', *Journal of Geophysical Research: Planets* **107**(E12), 2–1–2–6. 5119.
URL: *http://dx.doi.org/10.1029/2002JE001851*

Azuma, S. and Katayama, I. (2017), 'Evolution of the rheological structure of mars', *Earth, Planets and Space* **69**(1), 8.
URL: *https://doi.org/10.1186/s40623-016-0593-z*

Baratoux, D., Samuel, H., Michaut, C., Toplis, M. J., Monnereau, M., Wieczorek, M., Garcia, R. and Kurita, K. (2014), 'Petrological constraints on the density of the martian crust', *Journal of Geophysical Research: Planets* **119**(7), 1707–1727.
URL: *https://agupubs.onlinelibrary.wiley.com/doi/abs/10.1002/2014JE004642*

Blakely, R. J. (1996), *Potential Theory in Gravity and Magnetic Applications*, Cambridge University Press.
URL: *https://app.knovel.com/hotlink/khtml/id:kt006QTSXP/potential-theory-in-gravity/an-example-from-steady*

Burg, J.-P. (2017), *Lithospheric Strength Profiles*, ETH Zürich and Universität Zürich.

Burov, E. B. (2011), 'Rheology and strength of the lithosphere', *Marine and Petroleum Geology* **28**(8), 1402 – 1443.
URL: *http://www.sciencedirect.com/science/article/pii/S0264817211001425*

Byerlee, J. (1978), 'Friction of rocks', *pure and applied geophysics* **116**(4), 615–626.
URL: *https://doi.org/10.1007/BF00876528*

Close, D. (2010), 'Isostasy and gravity modelling: Integrating potential field data in interpretation workflows', *Recorder* **35**(06).

Denton, P. (2017), 'Marsquake: Seismology on another planet', British Geological Survey.

Fowler, C. (2005), *The Solid Earth: An Introduction to Global Geophysics*, Cambridge University Press.
URL: *https://books.google.nl/books?id=PifkAotvTroC*

Golombek, M. P., Banerdt, W. B., Tanaka, K. L. and Tralli, D. M. (1992), 'A prediction of mars seismicity from surface faulting', *Science* **258**(5084), 979–981.
URL: *http://science.sciencemag.org/content/258/5084/979*

Goossens, S., Sabaka, T. J., Genova, A., Mazarico, E., Nicholas, J. B. and Neumann, G. A. (2017), 'Evidence for a low bulk crustal density for mars from gravity and topography', *Geophysical Research Letters* **44**(15), 7686–7694.
URL: *https://agupubs.onlinelibrary.wiley.com/doi/abs/10.1002/2017GL074172*

H. Barosio, A., F. Valdés-Galicia, J. and Fucugauchi, J. (2001), 'Mars thermal history based on its tectonic and structural systems', *Geofísica Internacional* **41**.

Karimi, R., Azmoudeh Ardalan, A. and Vasheghani Farahani, S. (2017), 'The size, shape and orientation of the asteroid Vesta based on data from the Dawn mission', *Earth and Planetary Science Letters* **475**, 71–82.

Klees, R. (2000), 'Representation of the gravitational potential in spherical harmonics'.

Knapmeyer, M., Oberst, J., Hauber, E., Wählisch, M., Deuchler, C. and Wagner, R. (2006), 'Working models for spatial distribution and level of mars' seismicity', *Journal of Geophysical Research: Planets (1991–2012)* **111**(E11).
URL: *http:https://doi.org/10.1029/2006JE002708*

Lorenz, R. D., Nakamura, Y. and Murphy, J. R. (2017), 'Viking-2 seismometer measurements on mars: Pds data archive and meteorological applications', *Earth and Space Science* **4**(11), 681–688.
URL: *https://agupubs.onlinelibrary.wiley.com/doi/abs/10.1002/2017EA000306*

Marinova, M. M., Aharonson, O. and Asphaug, E. (2008), 'Mega-impact formation of the mars hemispheric dichotomy', *Nature* .

McLennan, S. M. (2001), 'Crustal heat production and the thermal evolution of mars', *Geophysical Research Letters* **28**(21), 4019–4022.
URL: *https://agupubs.onlinelibrary.wiley.com/doi/abs/10.1029/2001GL013743*

Melosh, H. (2011), *Planetary Surface Processes*, Cambridge Planetary Science, Cambridge University Press.
URL: *https://books.google.nl/books?id=3bQD1DJgliIC*

Mueller, K. and Golombek, M. (2004), 'Compressional structures on mars', *Annual Review of Earth and Planetary Sciences* **32**(1), 435–464.
URL: *https://doi.org/10.1146/annurev.earth.32.101802.120553*

Neumann, G. A., Zuber, M. T., Wieczorek, M. A., McGovern, P. J., Lemoine, F. G. and Smith, D. E. (2004), 'Crustal structure of mars from gravity and topography', *Journal of Geophysical Research: Planets* **109**(E8), n/a–n/a. E08002.
URL: *http://dx.doi.org/10.1029/2004JE002262*

Pascal, C. (2006), 'On the role of heat flow, lithosphere thickness and lithosphere density on gravitational potential stresses', *Tectonophysics* **425**(1), 83 – 99.
URL: *http://www.sciencedirect.com/science/article/pii/S0040195106003532*

Perron, J. T., Mitrovica, J. X., Manga, M., Matsuyama, I. and Richards, M. A. (2007), 'Evidence for an ancient martian ocean in the topography of deformed shorelines', *Nature* .

Plesa, A.-C., Knapmeyer, M., Golombek, M. P., Breuer, D., Grott, M., Kawamura, T., Lognonné, P., Tosi, N. and Weber, R. C. (2018), 'Present-day mars' seismicity predicted from 3-d thermal evolution models of interior dynamics', *Geophysical Research Letters* **45**(6), 2580–2589.
URL: *https://agupubs.onlinelibrary.wiley.com/doi/abs/10.1002/2017GL076124*

Raulin, C. (2007), Stress state and structure of the fennoscandian lithosphere, Master's thesis, University of Paris.

Root, B. (2018), 'Planetary gravity field modelling', Lecture slides.

Root, B., Ebbing, J., van der Wal, W., England, R. and Vermeersen, L. (2017), 'Comparing gravity-based to seismic-derived lithosphere densities: a case study of the british isles and surrounding areas', *Geophysical Journal International* **208**(3), 1796–1810.
URL: *http://dx.doi.org/10.1093/gji/ggw483*

Root, B., Novák, P., Dirkx, D., Kaban, M., van der Wal, W. and Vermeersen, L. (2016), 'On a spectral method for forward gravity field modelling', *Journal of Geodynamics* **97**, 22 – 30.
URL: *http://www.sciencedirect.com/science/article/pii/S0264370715300533*

Sneeuw, N. (1994), 'Global spherical harmonic analysis by least-squares and numerical quadrature methods in historical perspective', *Geophysical Journal International* **118**(3), 707–716.
URL: *https://onlinelibrary.wiley.com/doi/abs/10.1111/j.1365-246X.1994.tb03995.x*

Stein, S., Wysession, M. and Stein, S. (2003), *Introduction to Seismology, Earthquakes, and Earth Structure*, Blackwell Publishing.

Tenzer, R., Eshagh, M. and Jin, S. (2015), 'Martian sub-crustal stress from gravity and topographic models', *Earth and Planetary Science Letters* **425**, 84 – 92.
URL: *http://www.sciencedirect.com/science/article/pii/S0012821X15003477*

Watters, T. R. and McGovern, P. J. (2006), 'Introduction to special section: The hemispheric dichotomy of mars', *Geophysical Research Letters* **33**(8).
URL: *https://agupubs.onlinelibrary.wiley.com/doi/abs/10.1029/2006GL025755*

Watts, A. B. (2001), *Isostasy and Flexure of the Lithosphere*, Isostasy and Flexure of the Lithosphere, Cambridge University Press.
URL: *https://books.google.nl/books?id=CNkiZU7enWUC*

Watts, A. B. and Moore, J. D. P. (2017), 'Flexural isostasy: Constraints from gravity and topography power spectra', *Journal of Geophysical Research: Solid Earth* **122**(10), 8417–8430.
URL: *https://agupubs.onlinelibrary.wiley.com/doi/abs/10.1002/2017JB014571*

Wieczorek, M. (2007), 'Gravity and topography of the terrestrial planets', *Treatise on Geophysics* **10**, 165–206.

Wieczorek, M. (2015), 10.05 - gravity and topography of the terrestrial planets, *in* G. Schubert, ed., 'Treatise on Geophysics (Second Edition)', second edition edn, Elsevier, Oxford, pp. 153 – 193.
URL: *https://www.sciencedirect.com/science/article/pii/B978044453802400169X*

Wieczorek, M. A. and Zuber, M. T. (2004), 'Thickness of the martian crust: Improved constraints from geoid-to-topography ratios', *Journal of Geophysical Research: Planets* **109**(E1).
URL: *https://agupubs.onlinelibrary.wiley.com/doi/abs/10.1029/2003JE002153*

Zharkov, V. and Gudkova, T. (1993), 'On the dissipative factor of the martian interiors', *Astron Vestn.* **27**(4), 3–15.

Zharkov, V. and Gudkova, T. (1997), 'On the dissipative factor of the martian interiors', *Planetary and Space Science* **45**(4), 401 – 407.
URL: *http://www.sciencedirect.com/science/article/pii/S0032063396001444*

Zuber, M. T., Solomon, S. C., Phillips, R. J., Smith, D. E., Tyler, G. L., Aharonson, O., Balmino, G., Banerdt, W. B., Head, J. W., Johnson, C. L., Lemoine, F. G., McGovern, P. J., Neumann, G. A., Rowlands, D. D. and Zhong, S. (2000), 'Internal structure and early thermal evolution of mars from mars global surveyor topography and gravity', *Science* **287**(5459), 1788–1793.
URL: *http://science.sciencemag.org/content/287/5459/1788*